PhD Thesis

Novel nanofabrication methods and processes for quantum photonic integrated circuits

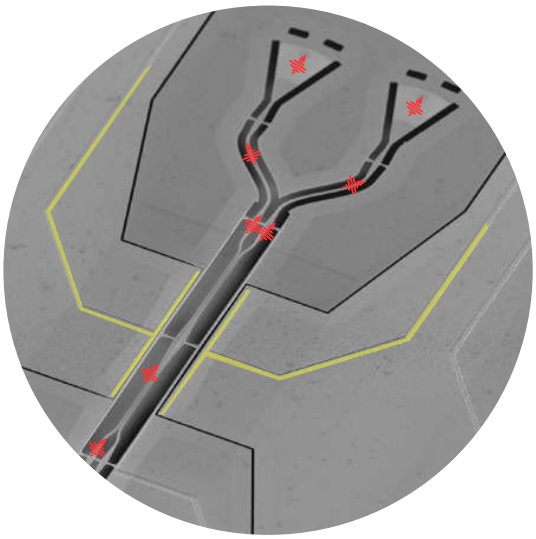

Ying Wang

June 3, 2021

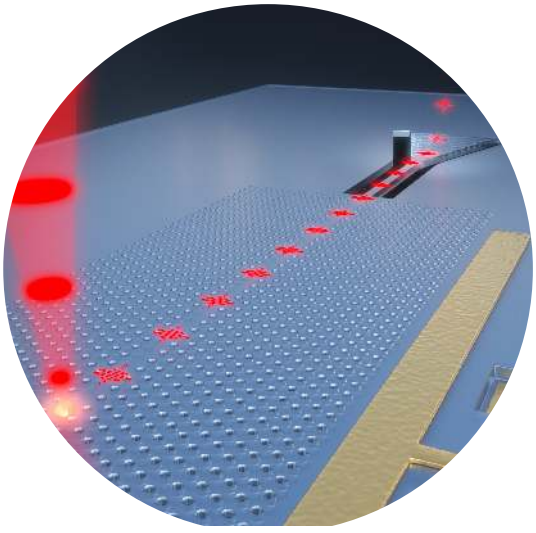

Colophon

This thesis was set with LaTeX 2$_\varepsilon$ using the memoir class.
Graphics created using Matlab 2018, Matplotlib under Python 3.6, as well as Inkscape.
Chapterstyles courtesy CP3.

Novel nanofabrication methods and processes for quantum photonic integrated circuits

Author	Ying Wang
Advisor	Leonardo Midolo
Advisor	Peter Lodahl

UNIVERSITY OF COPENHAGEN

Quantum Photonics

Center for Hybrid Quantum Networks (Hy-Q)
The Niels Bohr Institute

This thesis has been submitted to
The PhD School of The Faculty of Science
University of Copenhagen
June 3, 2021

Abstract

Single quantum dots are competitive candidates for the realization of highly-pure, highly-indistinguishable, and highly-efficient single-photon sources. To perform quantum information processing using single photons, hundreds of identical single photons are required. Therefore, scalable and integrated single-photon sources are needed. In this project, novel methods for the design and fabrication of scalable nanophotonic devices with integrated quantum emitters have been developed. These devices exhibit outstanding properties as single-photon sources with higher fabrication yield and faster electrical response.

Near-ideal single-photon sources in planar nanostructures with small localized electrical gates have been demonstrated. Photonic crystal waveguides have been used to tailor light-matter interaction and achieve near-deterministic operation over a broad wavelength range. An indistinguishability exceeding 97 %, a purity of >98 %, and a total efficiency of 8.4 % are simultaneously obtained in these devices, thanks to the improved nanofabrication process developed in this work. Several designs of near-unity purity and indistinguishability sources have been realized on-chip. These include special integrated circuits for resonantly exciting the quantum dots via nanophotonic waveguides. Such an excitation scheme enables long-time operation without losing alignment and offers the potential to scale up the number of sources integrated in the same chip.

The main figures of merit to assess the quality of single-photon emission and their characterization are discussed. The existing limitations are well understood: for example the purity is mainly limited by the limited suppression of the excitation laser background, while the photon distinguishability is due to the coupling of the quantum dot with its host environment, leading to charge, spin, and phonon noise. In gated devices, the charge noise and spin noise have been significantly suppressed, and only the phonon noise is a fundamental limitation. We experimentally show how indistinguishability changes as a function of temperature in a photonic crystal waveguide and identify various mechanisms involved in the degradation of the emitters' coherence. At $T < 10$K, the dephasing is induced by the linear phonon coupling, while above 10K, dephasing is dominated by acoustic phonon quadratic coupling enabling virtual transitions in the quantum dot.

Optical propagation loss is still the most challenging aspect when considering the total source efficiency. Waveguide loss becomes a serious issue when scaling to multiple sources or larger photonic integrated circuits. In this work, the origin of optical loss in gated nanophotonic waveguides as a function of temperature, wavelength, and external voltage is discussed. We found that the electroabsorption due to the Franz-Keldish effect, is the dominant loss mechanism. A strong surface electric field, induced by Fermi-level pinning, leads to loss over 20 dB/mm at room temperature in un-passivated samples. It is therefore necessary to reduce losses for scaling up further.

The thesis reports on the fabrication techniques developed towards building single-photon sources with state-of-the-art properties. While further scaling in GaAs seems

prohibitive due to optical loss, the sources and fabrication methods reported here could be readily used for heterogeneous integration in other material platforms. The results constitute an important step forward in building a fully-scalable photonic integrated platform with applications in quantum computing and simulation.

Sammenfatning

Kvantepunkter er lovende kandidater til at realisere meget enkeltfotonrene og kvantemekanisk uadskillelighed samt yderst effektive enkelt-foton kilder. For at udføre kvantemekanisk informationsprocessering ved brug af enkelte fotoner, kræves hundredvis af identiske enkelte fotoner. Derfor er skalerbare og integrerede enkelt-foton kilder en nødvendighed. I denne afhandling, er nye metoder til at designe og fabrikere skalerbare nanofotoniske enheder med integrerede kvante-emittere blevet udviklet. Disse enheder udviser fremragende egenskaber som enkelt-foton kilder, med højere fabrikationsudbytte og hurtigere elektrisk responds.

Tæt på ideelle enkelt-foton kilder i plane nanostrukturer med små lokaliserede elektriske kontakter er blevet udviklet. Fotonisk krystal-bølgeledere er blevet brugt til at skræddersy lys-stof-vekselvirkningen og opnå tæt på deterministisk drift over en bred række af bølgelængder. En kvantemekanisk uadskillelighed over 97%, enkeltfotonrenhed >98 % og en samlet effektivitet på 8.4 % er opnået samtidigt i disse enheder, takket være den forbedrede nanofabrikationsproces udviklet i denne afhandling. Adskillige design med tæt på perfekt enkeltfotonrenhed og kvantemekanisk uadskillelighed er succesfuldt blevet realiseret on-chip. Disse inkluderer specielt integrerede kredsløb til resonant excitation af kvantepunkterne gennem de nanofotoniske bølgeledere. Sådanne excitationsmetoder muliggør langvarig manipulation uden at miste fin-justeringen samt giver mulighed for potentiel opskalering af antallet af kilder integreret på samme chip.

De primære parametre for at evaluere kvaliteten af enkelt-foton emissionen samt dennes karakterisering er diskuteret. De eksisterende begrænsninger er forstået: for eksempel er enkeltfotonrenheden hovedsageligt begrænset af undertrykkelsen af excitationslaser baggrunden, mens foton adskilleligheden er tilstede på grund af koblingen mellem kvantepunktet og det omkringliggende miljø, hvilket leder til ladnings-, spin- og fonon støj. I enheder med elektriske kontakter, er ladnings- og spin støj tydeligt undertrykt, mens kun fonon støj er en grundlæggende begrænsning. Vi har eksperimentalt vist, at den kvantemekaniske uadskillelighed ændres som funktion af temperatur i en fotonisk krystal-bølgeleder og identificeret adskillige af de mekanismer, der er involveret i nedbrydningen af emitterens kohærens. Ved $T < 10$ K er dephasing fremkaldt af lineær fonon kobling, mens dephasing ved temperature over 10 K er domineret af kvadratisk akustiske fonon kobling, hvilket muliggør virtuelle overgange i kvantepunktet.

Optisk udbredelsestab er stadig det mest udfordrende aspekt, når det kommer til den samlede kildes effektivitet. Bølgeleder-tab bliver et alvorligt problem, når der skaleres til flere kilder eller til store fotonisk integrerede kredsløb. I denne afhandling diskuteres oprindelsen af optisk tab i nanofotoniske bølgeledere med elektriske kontakter som en funktion af temperatur, bølgelængde og ekstern spænding. Vi har fundet at elektroabsorptionen, grundet Franz-Keldish effekten, er den dominerende tabsmekanisme. Et stærkt overflade elektrisk felt, induceret af Fermi-level pinning, fører til et tab på over 20 dB/mm ved stue temperatur i ikke-passiverede prøver. Det er derfor nødvendigt at reducere mængden af tab for at skalere yderligere.

Denne afhandling beskriver fabrikationsteknikker udviklet til at bygge enkelt-foton kilder med state-of-the-art egenskaber. Mens videre skalering i GaAs kan virke begrænset grundet optisk tab, så kan drifts- og fabrikationsmetoderne beskrevet her anvendes ligetil i andre heterogene materialer. Resultatet udgør et vigtigt skridt fremad mod at bygge fuldt skalerbare fotonisk integrerede platforme med brede applikationsmuligheder i kvantecomputer og kvantesimulationsteknologien.

Preface

My three-year Ph.D. journey is approaching to its end as the thesis writing finishes. The project was carried out in the Quantum Photonics group at the Niels Bohr Institute, in the University of Copenhagen. Looking back on the past three years, this journey was challenging but fruitful. I was always passionate about my research and felt supported throughout the entire period, since Quantum Photonics is a fantastic group, that performs exciting research and brings together a great group of wonderful colleagues. Here I present my sincere gratitude to all the people who supported me throughout this period.

Firstly, I would like to thank my supervisor, Associate Professor Leonardo Midolo. The project was initiated and supervised by him. He is a great supervisor. Considering my different background, he motivated my interest in physics and guided me through the material that would prepare me for my research the best. Aside from teaching me many of the things that I know today, as different software tools, he was also always very patient and encouraged me to move forward. Then, I would like to thank Professor Peter Lodahl, for giving me the chance to study in the Quantum Photonics group. As the PI of the group, he has been selecting really wonderful people and built a great research environment. His feedback and suggestions along my PhD were always helpful to steer my project to a good direction. Further more, I would like to thank very much Ravitej Uppu, for all the knowledge he so generously shared. Ravi taught me all that I know about optical spectroscopy and was always so engaged to our work in the lab, on every single project that was running. He was for long time the hero of the lab, always coming to the rescue. I would also like to thank Zhe Liu, who taught me all that I know about fabrication. Zhe had always been available for helping and guiding me through my work at the HCØ. I learned a lot from his great experience and enjoyed the time we spent in the cleanroom.

Next I would like to thank my colleagues, starting with the fab team, Tomasso Pregnolato, Camille Papon, Asli Dilara Ugurlu and Atefeh Shadmani,Celeste Qvortrup, Arianne Stenberg Brooks and Lasse for all the fruitful discussions throughout these three years. A big thank you goes to the people who helped hunt for single photons, Xiaoyan Zhou, Henri Thyrrestrup, Freja Thilde Pedersen, Alexey Tiranov, Mikkel Mikkelsen, Nils V. Hauff, Hanna Le Jeannic, Thomas Hummel and Xiao-Liu Chu. Moreover I want to thank each one of my office mates, as well as all the members of the Quantum Photonics group individually, Ming Lai Chan, Eva M. Gonzalez Ruiz, Johann Kollath-Böning, Rodrigo A. Thomas, Martin H. Appel, Cecilie T. Olesen, Adam Søsted Knorr, Vasso Angelopoulou, Patrik Sund, Beatrice da Lio, Carlos Faurby and Mathias J. Rønne Staunstrup, not only for the physics discussions, but for the everyday company in the office and out. I would also like to thank few more of the HyQ members, Ivan Galinskiy, Yannick Seis, Eric C. Langman and Eric Planz, for the relaxing breaks and ice cream walks. I would like to wholeheartedly thank Freja for taking me out to get some fresh air and for always checking on me during the writing of the current thesis. Also Camille and Vasso for being carrying and motivating throughout the past months.

In addition, I would like to thank the friends that I met in Copenhagen, for giving me the chance to cook and eat Chinese food, which kept me far from feeling homesick, as well as all my friends scattered around the world, that were always present, listening, texting and supporting me. Especially I want to thank Hua Wei, for being my close friend and for inspiring me to be a strong and independent person. Finally, I would like to thank my parents and my younger brother, for their unconditional love and support.

List of publications

1. *Electroabsorption in gated GaAs nanophotonic waveguides.* Ying Wang Ravitej Uppu, Xioyan Zhou, Camille Papon, Sven Scholz, Andreas D. Wieck, Arne Ludwig, Peter Lodahl, Leonardo Midolo. Appl. Phys. Lett., 2021, 118, 131106.

2. *Near Transform-Limited Quantum Dot Linewidths in a Broadband Photonic Crystal Waveguide.* Freja T. Pedersen, Ying Wang, Cecilie T. Olesen, Sven Scholz, Andreas D. Wieck, Arne Ludwig, atthias C Löbl, Richard J. Warburton, Leonardo Midolo, Ravitej Uppu, Peter Lodahl. ACS Photonics, 2020, 7, 2343-2349.

3. *Scalable integrated single-photon source.* Ravitej Uppu, Freja T. Pedersen, Ying Wang, Cecilie T. Olesen, Camille Papon, Xiaoyan Zhou, Leonardo Midolo, Sven Scholz, Andreas D. Wieck, Arne Ludwig, Peter Lodahl. Science Advances, 2020,6.

4. *On-chip deterministic operation of quantum dots in dual-mode waveguides for a plug-and-play single-photon source.* Ravitej Uppu, Hans T. Eriksen, Henri Thyrrestrup, Asli D. Uurlu, Ying Wang, Sven Scholz, Andreas D. Wieck, Arne Ludwig, Matthias C. L¨obl, Richard J. Warburton, Peter Lodahl, and Leonardo Midolo. Nature Communication, 2020, 11, 3782.

5. *A coherent spin-photon interface with waveguide induced cycling transitions.* Martin Hayhurst Appel, Alexey Tiranov, Alisa Javadi, Matthias Christian Löbl, Ying Wang, Sven Scholz, Andreas Dirk Wieck, Arne Ludwig, Richard John Warburton, Peter Lodahl. Physical Review Letters, 2021,126, 013602.

In preparation

1. *Phonon induced decoherence of QDs coupled to GaAs photonic crystal waveguide.* Ying Wang, Freja T. Pedersen, Camille Papon, Mikkel Mikkelsen, Sven Scholz, Andreas D. Wieck, Arne Ludwig, atthias C Löbl, Richard J. Warburton, Leonardo Midolo, Ravitej Uppu, Peter Lodahl.

Contents

Chapter 1

Introduction to photonic quantum technologies

Introducing the field of photonic quantum technologies and the relevant theoretical background on self-assembled quantum dots coupled to nanophotonic devices for the efficient generation of high-quality single photons.

The revolution of information technology has been accelerated by the advances in the miniaturization of electronic circuits on silicon chips, which enable the computing power to double roughly every two years (according to Moore's law) since 1960s. During the first two decades of the twenty-first century, as electronic devices are approaching atomic dimensions, quantum effects started to emerge and pose limitations to Moore's law. A new paradigm is required if the revolution is to continue at anything like the rate that was set in at end of last century. Accordingly, considerable efforts have been devoted to address the challenges of designing and fabricating devices at the atomic scale and making them work reliably according to the laws of quantum physics, a field known broadly as quantum nanotechnology.

Recently, nanotechnology has made possible the realization of the first quantum information processors, i.e. devices capable of manipulating quantum states. These devices are expected to tackle computational tasks that go beyond the power of classical computation. Therefore, novel scientific opportunities are brought up, attracting an increasingly growing community of scientists and engineers to build quantum computers.

In particular, *photonic* quantum technology is expected to play a big role in the field of quantum information processing due to the natural advantage of single photons as information carrier, possessing high speed and low decoherence. Moreover, it

opens opportunities for distributing quantum states over long distances in the form of single photons. A key element of photonic quantum technology is the possibility to produce single photons on-demand with high quality. With the advent of modern epitaxial growth techniques, such single-photon emitters can be reliably built using semiconductor quantum dots (QDs) and directly embedded in a circuit, enabling the development of *integrated* photonic quantum technologies.

In this introductory chapter, we will provide a brief overview of the field of quantum information processing and to the state-of-the-art in quantum photonic integration. Then, we will introduce the theoretical background of QDs and we discuss the physics of light-matter interaction in photonic nanostructures, which is required throughout the rest of this thesis. Finally, the thesis topics and objectives are given in 1.3.

1.1 Quantum information processing

Combining two good things can sometimes create something even better, as in the case of quantum information: the marriage of computing theory and quantum physics. Quantum information is an interdisciplinary field that combines quantum mechanics, computer science, information theory, and cryptography. In the late nineteenth century, the mansion of classical physics was close to complete. However two dark clouds appeared, namely electrons fall into the atomic nucleus and the existence of an ultraviolet catastrophe, which brought to a series of crises for the classical view of physics. Early measurements of the atomic spectrum revealed that the energy levels inside an atom are discrete. Later, with the advent of Schrödinger's wave equation (1926), the modern theory of quantum mechanics was created, which portrays a world that is fundamentally probabilistic and describes the microscopic systems using probability distributions..

Quantum mechanics provides a mathematical framework for the construction of physical theories. Compared to classical systems, quantum mechanics displays radically different rules. The most famous is perhaps Heisenberg's uncertainty principle, which sets a fundamental limit to the simultaneous measurement accuracy of some physical observables. For example, it is impossible to measure the position x and the momentum p of a particle simultaneously with absolute certainty. Instead, the product of the uncertainties of the two observables exhibit a lower bound

$$\sigma_x \sigma_p \geqslant \hbar/2. \tag{1.1}$$

Another difference between classical and quantum systems is the concept of superposition, which allows the state of particle to be in a superposition of several states. For example, if a quantum object can be observed in two possible states, denoted $|0\rangle$ and $|1\rangle$, its most generic state before observation can be written as

$$|\psi\rangle = \alpha\,|0\rangle + \beta\,|1\rangle\,, \tag{1.2}$$

where α and β are two complex numbers. Upon measurement, the state is known to "collapse" into one of the possible states, with probability $|\alpha|^2$ and $|\beta|^2$, respectively,

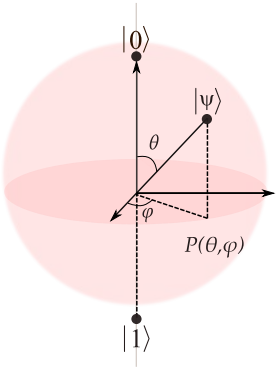

Figure 1.1: Representation of a quantum state $|\psi\rangle$ using the Bloch sphere. Two angles θ and ϕ define the complex coefficients α and β of equation 1.2 in polar coordinates.

with $|\alpha|^2 + |\beta|^2 = 1$. The state of equation 1.2 represents a quantum bit (or qubit, see Fig. 1.1), where the information encoded in the state is clearly much more than in a classical binary digit (bit). The concept of superposition is incredible from the perspective of the classical world, but its existence has been widely confirmed in microscopic system. Most two-level systems (TLS) such as ions, atoms, electron spin, exhibit superposition states and are therefore excellent candidates to implement stationary (or "matter") qubits. Photons as well can be used to realize "flying" qubits carrying information in their degrees of freedom (spatial, temporal, or polarization). Yet, the most unique phenomenon in quantum mechanics, is the entanglement between two or more quantum objects. Quantum entanglement occurs whenever the state describing multiple objects, can no longer be separated. An example of an entangled state between two quantum systems A and B is given by

$$|\psi_{\mathrm{A,B}}\rangle = \frac{1}{\sqrt{2}} \left(|0\rangle_{\mathrm{A}} |1\rangle_{\mathrm{B}} + |1\rangle_{\mathrm{A}} |0\rangle_{\mathrm{B}} \right), \tag{1.3}$$

which implies that the probability of the object A or B to be in state $|0\rangle$ or $|1\rangle$ is 50 %. However, if the object A is measured in the state $|0\rangle$, the object B has to be in the state $|1\rangle$, and vice versa, irrespective of how far A and B are located. For this reason, quantum entanglement is a unique resource, which is not limited by space and time. Creating and manipulating entangled states and subsequently performing measurements is at the core of quantum technologies and the idea that quantum computing is possible.

Quantum computing is the processing of quantum information using the principles of superposition and entanglement developed in quantum mechanics. Any physical apparatus exploiting the principles of quantum mechanics is, in a broad sense, a quantum computer. Yet a more strict definition requires the quantum computer to surpass the computing power of classical computers (i.e. show some speed up or advantage) and solve problems that existing computers cannot solve. Some criteria (known as Di Vincenzo's criteria) have been developed to define a quantum computer

in year 2000 [1]. It consists of seven conditions that an experimental setup must satisfy to implement quantum algorithms and quantum computation. Among these, the first and likely most important criterion requires a *scalable* physical system to work with arbitrary number of qubits. To date, scalability is still the most critical issue for most quantum systems.

Many quantum mechanical systems are being explored to achieve quantum computing, like nuclear magnetic resonance (NMR), ion traps, quantum dots (QD)s, multi-photon system, cavity quantum electrodynamic (QED) systems, solid-state electron and nuclear spins, superconducting systems, topological quantum materials, etc. [2–10]. Every system displays its unique advantages and the future quantum computer will likely involve several systems in a hybrid platform [11], likely distributed over distant nodes [12].

In this thesis, I will focus on photonic quantum technologies, based on single photons and quantum emitters, whose prominent feature is to enable long-distance quantum communication, but has recently drawn attention as a platform for computing and simulation [13, 14], with an ever-increasing interest from the industry [15] and start-ups(1).

1.1.1 Photonic quantum technologies and integration

Photonic quantum technologies involve the generation, processing, and detection of quantum light. Fig. 1.2 shows the components which are necessary to develop the full potential of quantum photonics.

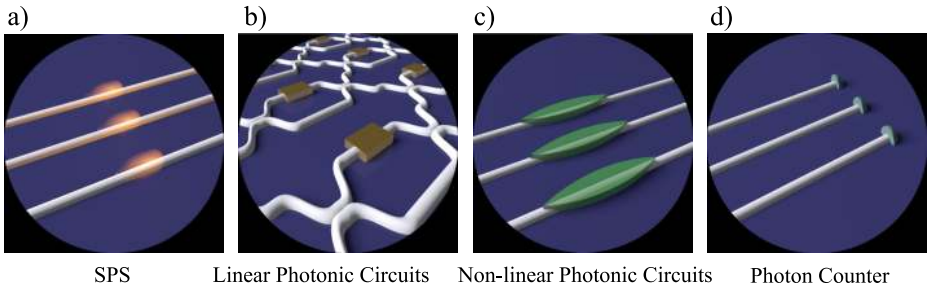

Figure 1.2: Schematics of the required functionalities for quantum photonics: a) Single-photon source (SPS), b) Reconfigurable circuits for linear and c) Non-linear optical processing, d) Single-photon detectors and counters. Courtesy of Dr. Jacques Carolan.

Single-photon sources

Single photon sources (SPS) are the most fundamental building block. SPS with high purity, indistinguishability, and brightness are required to produce large number of

(1) https://psiquantum.com/

photonic qubits in a scalable manner. These concepts will be illustrated in greater detail in Chapter 4.

The two most widely used SPSs are, to date, based either on non-linear frequency conversion or on the spontaneous emission of quantum emitters. The single photons generated by non-linear frequency conversion methods, such as spontaneous four-wave mixing (SFWM) [16] and spontaneous parametric down conversion (SPDC) [17], exhibit high purity and indistinguishability [18] but are fundamentally *probabilistic* (i.e. they cannot be produced on-demand). Even though time [17] and spatial [19] multiplexing techniques can be implemented to improve this issue, there is still a trade off between source efficiency and indistinguishability, which makes scaling very challenging.

SPS based on solid-state emitters such as QDs provide instead a deterministic method to generate photons. Arguably, the best performing QD based SPSs are obtained by self-assembled InAs(Ga)As QDs. A series of near-optimal QD-based SPS [20–26] have been achieved thanks to the highly-mature material growth and nano-fabrication technologies, as well as the optical characterization techniques and the creative design of novel nano-devices. However, it is challenging to create scalable multiple identical SPSs using self-assembled QDs due to the inhomogeneous distribution of QDs sizes, leading to different photon emission wavelengths.

One approach for producing multiple photons is to spatially de-multiplex the single photons emitted by a single QD [27] with a reduced overall rate. Alternatively, modifying the QDs environment using techniques such as Stark tuning [28], strain tuning [29] and temperature tuning [30], could compensate for the inhomogeneous distribution of QD emission and provide multiple identical SPSs from separated QDs.

Photonic integrated circuits and single-photon detectors

To perform quantum information processing, linear [31] and non-linear [32] photonic circuits are required (cf. Fig. 1.2 b) and Fig. 1.2 c). These circuits provide a way to interfere several indistinguishable photons for implementing quantum gates.

To read out the results of the quantum interference, detectors sensitive to single photons (see Fig. 1.2 d)) are required. Single-photon detectors such as avalanche photodiodes (APD) and superconducting nanowire single photon detectors (SNSPD) [33] have been developed with high detection efficiency, spectral range, signal to noise ratio and capability to resolve photons number. Particularly, the recently demonstrated detector fabricated on-chip using superconducting nanowires with impedance-matching taper [34], suggests that full on-chip integration is feasible.

1.1.2 Architectures for photonic quantum information processing

Figure 1.3 a) shows a state-of-the-art free-space quantum photonic circuit, where optical components such as mirrors, polarizers, beamsplitters, mounted on an optical table are used to route and manipulate single photons. Impressive results have been demonstrated [35] with such system, approaching quantum advantage using single photons. Yet, to further scale up to hundreds or thousands of single photons, required for

a)

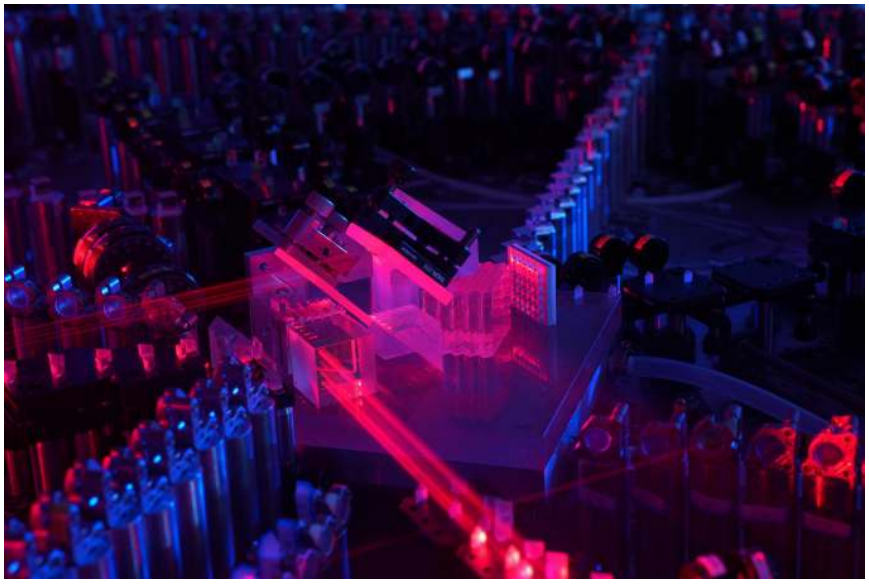

b)

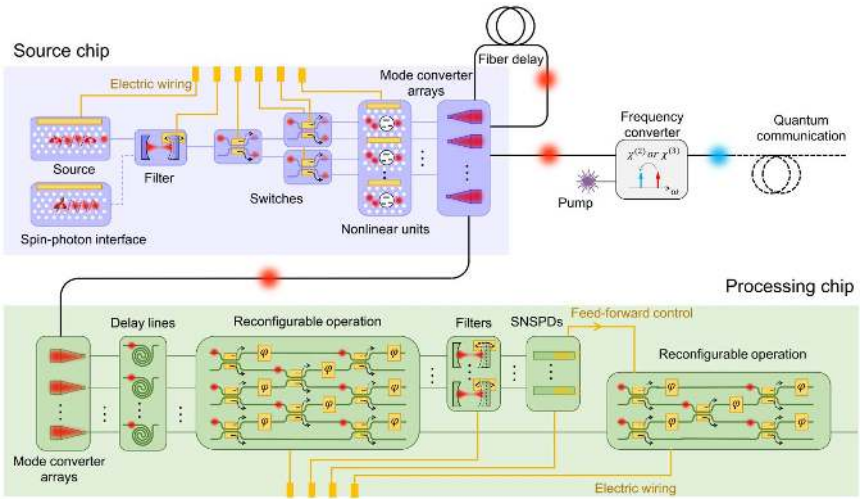

Figure 1.3: Architectures for photonic quantum information processing. a) Free-space photonic quantum circuits [35], b) Schematic view of quantum photonic integrated circuit with scalable building blocks [36].

large-scale quantum information, it is necessary to miniaturize the various components and integrate them within a single chip. On-chip integration is a promising approach to realize the functionalities illustrated in Fig. 1.3 b), where several photonic building blocks (sources, filters, switches, etc.) are integrated in a single chip with a footprint size at a scale of a few millimeters. The individual building blocks have been already

realized with excellent performance and offer good stability since they have been realized on a robust solid-state platform. Moreover, the advances in the development of fabrication techniques offer great potential for achieving the blueprint sketched in Fig. 1.3 b) in a single material platform.

In this thesis, I investigated fabrication methods and novel designs to integrate and interconnect several of these building block in the Gallium Arsenide (GaAs) material platform. The choice of GaAs mostly stems from the availability of the deterministic emitters (i.e. the QDs). Moreover, I focused primarily on the scalability of the SPS, but the methods developed in this work are potentially applicable to other devices. These fabrication methods are described in detail in Chapter 2. While the choice of GaAs as a single platform could solve many issues due to scalability, it is also unlikely that a full quantum computer or simulator can be built entirely in GaAs, mostly due to limitations in the waveguide losses (see the analysis carried out in Chapter 6). As mentioned earlier, a heterogeneous platform, using several photonic materials, could offer a better platform to realize the circuit shown in Fig. 1.3 b). Nevertheless, the fabrication methods and the SPS characterization developed in this thesis constitute a starting point toward the development of hybrid photonic quantum technologies.

Here, we briefly mention recent achievements towards on-chip heterogeneous integration. 1) Wafer bonding, where self-assembled In(Ga)As QDs sources are bonded to silicon nitride photonic circuits [37], has been realized using this approach, which shows optimal device performance from each individual material, 2) Transfer print, integration of QDs embedded in a GaAs cavity on a complementary -metal-oxide-semiconductor(CMOS)-processed silicon chip [38] has been achieved by this process, which provides a potential candidate for an on-chip single photon non-linear component, 3) Pick and place, scalable integration of SNSPDs with silicon and aluminum nitride waveguides has been demonstrated by this method [39], which enables on-chip detection of quantum light efficiently.

1.1.3 Challenges for on-chip integration

Several outstanding challenges are encountered towards the integration of multiple quantum devices within the same chip. These stem mostly from incompatibility between materials and fabrication processes. Some of these challenges are:

- The thermal mismatch of different building blocks in a single chip. Generally the quantum single emitters and SNSPD require cryogenic operation, whereas circuits such as those used for photon routing are based on thermo-optic and free-carrier plasma dispersion effects, which are more suitable for room-temperature operation.

- The optical losses due to the integration of different components. In addition to mode and phase velocity mismatch between different materials causing light scattering, the optical interconnects between room temperature circuits and cryogenic detectors inevitably leads to propagation loss.

- The technical limitations arising from nanofabrication. The intrinsic imperfection of fabrication itself increase the non-uniformity of the devices in a wafer scale. Moreover incompatible fabrication processing and added number of fabrication steps due to different building blocks deteriorate the devices performance.

Yet, the realization of on-chip integration of quantum photonic circuits is substantially valuable to perform quantum information tasks. In this thesis we concentrate on self-assembled QDs based photonics quantum system, which is an excellent system for developing solid qubits and flying qubits. The self-assembled QDs can achieve considerably high quality benefiting from the mature molecular beam epitaxy technology. The advances in techniques and equipment for the nano-fabrication enable to fabricate nano-devices with high precision. The coupling of the self-assembled QDs with well-designed nano-structures not only demonstrates a series of surprising quantum effects, but allows the generation of single photons with the right specifications for quantum computation.

1.2 Theoretical background

In this work, photonic devices are fabricated on a GaAs membrane with embedded self-assembeld In(Ga)As QDs, for the generation of single photons. QDs consist of tiny islands of tens of thousands of atoms forming a semiconductor heterostructure. Due to their small size, the quantum confinement of electrons and holes in three dimensions provides discrete energy levels. For this reason, QDs are usually considered as artificial atoms, having optical properties similar to single atoms. Unlike single atoms, however, such a solid-state platform can be readily embedded in photonic nanodevices. In the following, we briefly outline the properties of In(Ga)As QDs, and the fundamentals of light-matter interaction.

1.2.1 Growth and properties of self-assembled quantum dots

Quantum dots are grown using molecular beam epitaxy (MBE), which is an advanced and important material growth technique [42]. All the samples used in this thesis have been grown by Dr. Arne Ludwig and colleagues at University of Bochum, Germany. MBE can achieve high quality material since it allows controlling the growth of complex heterostructures with single atomic layer precision. The MBE process firstly evaporates high purity solid As and Ga into a chamber prepared with ultra high vacuum creating molecular beams directed towards a target, where a wafer substrate is mounted. The atomic vapor reaches a wafer substrate and diffuses around the surface forming a deposited single-atom layer until atoms reach energetically favorable locations [43].

Figure 1.4 a) sketches the layer structure of the typical heterostructure employed in this thesis. It consists of a 180-nm-thick membrane forming a waveguide comprising several layers of semiconductor materials deposited on top of each other. Different solid precursors can be used during the growth, allowing the preparation of different semiconductor compounds. Moreover, different elements can be introduced to the

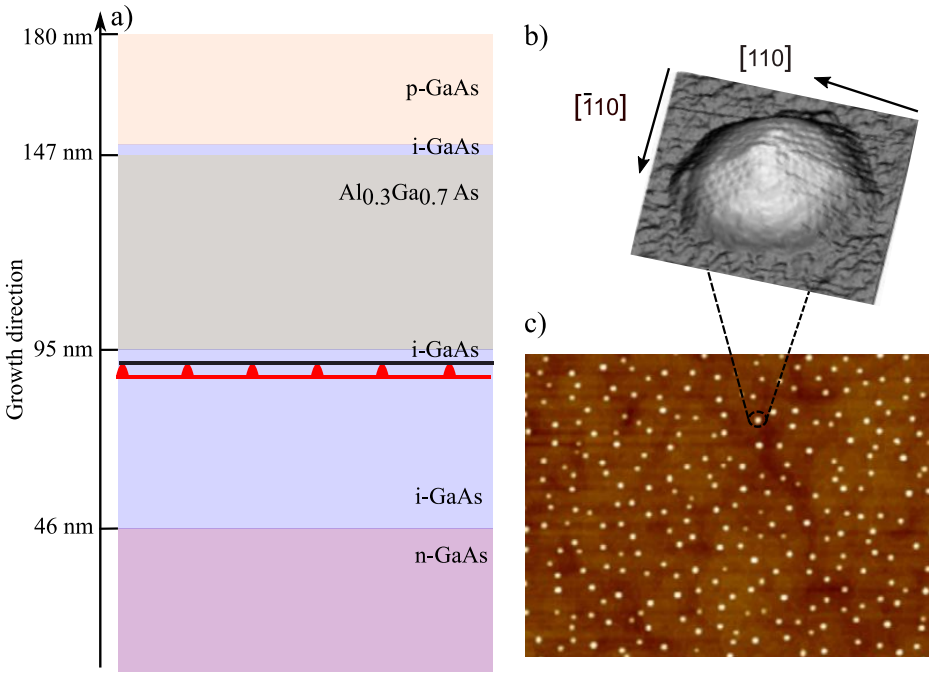

Figure 1.4: Semiconductor heterostructure and self-assembled QDs. a) Schematics of heterostructure membrane grown by molecular beam epitaxy method, with embedded QDs (red dots). b) Top-view of a Scanning Tunneling Microscope (STM) image of an uncapped InAs QD [40]. c) Atomic Force Microscope (AFM) image of self-assembled InAs QDs [41].

chamber at the same time enabling to introduce the dopants such as Si (for n-type doping of GaAs) and C (for p-type).

The self-assembled InAs QDs are grown in the middle of the GaAs membrane using the Stranski-Krastanov (SK) [44] method. Generally, two mono-layers of InAs are deposited on GaAs. The strain after 1.5 mono-layers, caused by the lattice mismatch between InAs and GaAs, leads to the formation of islands. A two-dimensional InAs layer, the so-called wetting layer (WL), is also formed below the QDs. A scanning tunneling microscope (STM) image (Fig. 1.4 b)) shows the QD morphology form the top view. The density and size of the QDs can be characterized by atomic force microscope (AFM) scans as the one shown in Fig. 1.4 c). The height and diameter of the QD islands are around 4–7 nm and 20–40 nm, respectively, which can not be deterministically controlled because they are very sensitive to the growth parameters. Also the spatial position and the geometry of QDs can not been controlled precisely since the residual strain is a process that locally nucleates InAs islands at random positions of the surface.

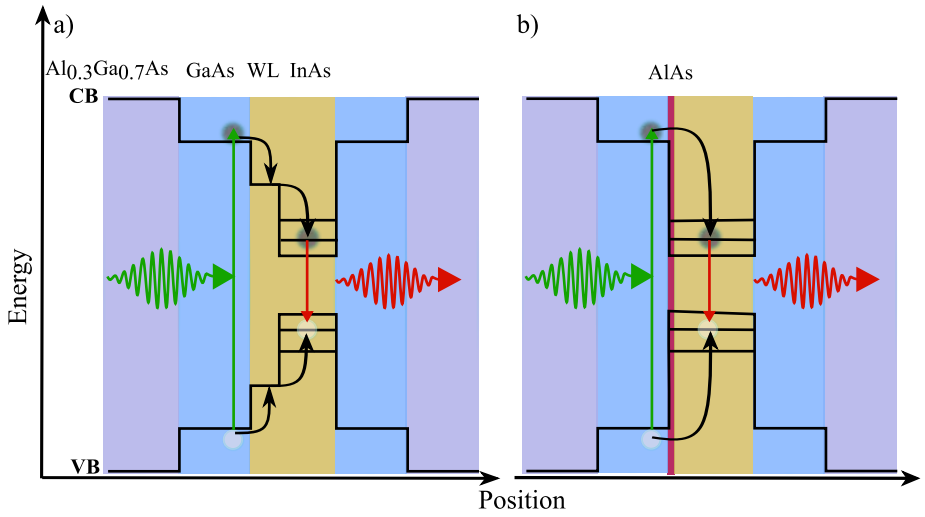

Figure 1.5: The electronic band diagram of an InAs QD embedded in a GaAs membrane, showing the energy of the conduction band (CB) and the valance band (VB) as a function of position along the growth direction. An optical pulse (green arrow) excites an electron (black) from the VB to CB and leaves a hole (white) in the VB, forming an exciton which can emit a photon (red arrow). a) QDs with wetting layer(WL), the solid arrows illustrates how carriers firstly couple to the WL and then relax in a QD. b) QDs without WL, the carriers can directly reach QDs.

Optical transitions in a quantum dot

The bandgap of InAs (the QD material) and GaAs (the surrounding material) are 0.35 eV and 1.42 eV, respectively and when aligned, they form a type-I heterojunction, which acts as a quantum well for both electrons and holes (see Fig. 1.5a). The three-dimensional confinement of the QD creates discrete energy states, which is similar to single atom possessing electronic orbitals, with different symmetries. The quantization occurs along the growth direction z because the confinement is stronger in this direction. Upon optical excitation, an electron in the valance band (VB) (black circle) is promoted to the conduction band (CB) leaving a vacancy (a hole) in the VB. Additionally, the electron and hole in a QD are attracted by the Coulomb interaction and form a bound state, called exciton. An above-band laser excitation transfers the carriers to the WL layer and finally to the QD.

Several optical transitions are possible in a QD, depending whether they satisfy certain selection rules. The lowest energy shell transitions between an electron in the conduction band and a hole in the valence band are parity-allowed, since their Bloch functions have opposite parity. Additionally, several spin combinations are possible for electron and holes, leading to a further classification into bright and dark states. The total angular momentum $J = S + L$ is employed to characterize the electronic states, for which the growth direction z is taken for the spin quantization. The spin of the electrons and holes is $S_{e/h} = 1/2$, while the orbital momentum L depends on the specific

valence band being considered. In most semiconductors, there are various valence bands, classified according to their band curvature, and therefore effective masses. The relevant valence band in QD is the so-called heavy-hole band, which is the most deeply confined.

Electrons have a wavefunction with an s-like character leading $L_e = 0$, while holes show an $p-$like character giving $L_h = 1$. The projected total momentum for electrons and heavy-holes is $J_e^z = \pm 1/2$ and $J_{hh}^z = \pm 3/2$. There are four possible bound states allowed from the recombination of an electron-hole pair $J_{e,h}^z = J_e^z + J_h^z$. According the optical selection rules [45], the allowed transition states are those where the change in total angular momentum is $\Delta J = \pm 1$, i.e. when electron and holes have opposite spin. Fig. 1.6 a) shows the level structure for two different decay process of a neutral exciton (i.e. a single electron and a single hole). The two energy levels are split in energy due to the exchange interaction. This fine structure splitting results from the lack of geometrical symmetry of the QDs. Similarly, two dark levels exists leading to $\Delta J = \pm 2$, which is optically forbidden.

Moreover, multiple electrons and holes in QDs can be recombined to form multiexcitonic states displaying different optical properties than single neutral exciton. Trions (two electrons and a hole or two holes and an electron) and biexcitons (two electrons and two holes) are the simplest examples of the multiexcitonic states.

Optimization of the quantum dots

One widely-known drawback of the QDs grown by SK-mode is the unwanted WL lying between QDs [46], which creates a continuum in energy very close to the QD confinement states. There is an energy gap between the QDs electron and hole states and the WL-continuum sates shown in Fig. 1.5 a). This gap can protect the QDs electrons and holes from coupling to the WL, but the gap is not complete and can only protect to a certain degree. Consequently, a low energy tail of the WL-continuum can extend to the QDs bound states [47]. This results in negative effects on the optical performance such as a broad absorption background [47] and phonon-exciton scattering [48]. Hence, the QD performance can be radically improved if the WL states are absent.

In this thesis, the QDs have been grown using a modified SK protocol for the purpose of removing the WL states. The InAs islands are capped with a single monolayer of AlAs (0.3 nm) first, followed by a capping layer of GaAs as shown in Fig. 1.4 a) , where the solid black line on the top of the red islands denotes the AlAs layer. The corresponding band diagram is sketched in Fig. 1.5 b).

Electrical control of quantum dots

The membrane structure shown in Fig. 1.4 a), consists of the bottom gate n-doped GaAs with thickness of 40 nm, the intrinsic layer of i-GaAs and $Al_{0.3}Ga_{0.7}As$ with the total thickness of 104 nm, the top gate p-doped GaAs (30 nm thick) and the InAs QDs without WL in the middle. The intrinsic layer in the middle reduces the total built-in electric field in the junction and reduces the current across the diode. When applying

an external bias to the diode structure, the electric field on the QDs can be controlled. The relation between the applied voltage bias and the responding current in an ideal case can be characterized using Shockley equation [49],

$$I = I_0 \left[\exp(\frac{eV}{k_B T}) - 1 \right], \tag{1.4}$$

where I_0 is the saturation current which depends on the doping density, k_B is Boltzmann constant, and T is temperature.

Using doped layers to control the electric field provides several advantages compared to undoped samples. The electrical control enables to tune the QDs emission energy through the Stark tuning [28] by a few meV. This gives one more degree of freedom to manipulate QDs. For example, it offers the possibility to tune the QDs emission into resonance with another QD or with a cavity mode and therefore to compensate the sample inhomogeneity or fabrication imperfections. But most importantly, the electrical gates can minimize the charge noise on the QDs (arising from trap states in defects), which is highly detrimental for the generation of indistinguishable photons [50], by "sweeping" away all charges in the proximity of the QD.

1.2.2 Quantum dots as two-level quantum emitters

An exciton in a QD can be described well using a two-band model only including heavy-hole valance and conduction band. As previously mentioned, the quantum confinement and strain lift the energy degeneracy of light-hole and heave-hole in the QDs and the transitions from the conduction band to the heavy-hole valence band possess the lowest energy. Thus, it is a good approximation neglecting the light-hole band [45]. In this model frame, the QDs size also shows energy level spacing larger than the Coulomb energy. So the motion of carriers in the conduction band and valance band can be considered independently and Coulomb effects included perturbatively [45]. Employing two-level system (TLS) model for QDs as single quantum emitter is very useful for investigating light-matter interaction and decay dynamics.

An optical pulse exciting the QD, triggers the transition from the ground state $|g\rangle$ to the excited state $|e\rangle$, and subsequently the TLS relaxes by spontaneous emission of a single photon. The Hamiltonian used to describe the interaction of a TLS and a light field consists of three components $H_S = H_{TLS} + H_F + H_I$, where H_{TLS} and H_F are the free Hamiltonians of the TLS and light field, respectively, while H_I is the light-matter interaction Hamiltonian. The dimension of the self-assembled In(Ga)As QDs is much smaller than their emission wavelength, which allows us to use the dipole approximation and write the interaction Hamiltonian as:

$$H_I = -\overrightarrow{d} \cdot \overrightarrow{E}, \tag{1.5}$$

where $\overrightarrow{d}$ is the dipole moment operator and $\overrightarrow{E}$ is the electric field operator at the QD position. Essentially, H_I couples different states of the emitter, allowing transitions

by emitting or absorbing a photon. The spontaneous decay rate Γ of a TLS can be calculated by Fermi's golden rule as

$$\Gamma = \frac{2\pi}{\hbar^2} \sum_{\mathrm{f}} |\langle f| H_{\mathrm{I}} |i\rangle|^2 \delta(\omega_{\mathrm{f}} - \omega_{\mathrm{i}}), \tag{1.6}$$

Here $|i\rangle$ and $|f\rangle$ denote the initial and final state of the TLS and $\delta(\omega_{\mathrm{f}} - \omega_{\mathrm{i}})$ indicates that the emitted photon frequency matches the separation of the two states.

From Fermi golden rule, it is possible [45] to derive an expression for Γ that depends on the transition dipole $|d|^2$ (a property of the emitter) and a quantity known as the local density optical state (LDOS), which is a property of the surrounding optical environment:

$$\Gamma(r_0, \omega_0, d) = \frac{\pi\omega_0}{\hbar\epsilon_0} |d|^2 \rho_{\mathrm{LDOS}}(r, \omega_0, \overrightarrow{e_{\mathrm{d}}}), \tag{1.7}$$

where r_0 is the emitter position, ω_0 is the emission frequency and $\overrightarrow{e_{\mathrm{d}}}$ is a unit vector defining the transition dipole orientation. The LDOS generally specifies interaction strength of the local-light matter and gives the number of optical states at frequency ω per bandwidth and volume. The LDOS can be greatly enhanced or suppressed using nanophotonic structures such as photonic crystals, which will be discussed in more detail in 1.2.4.

1.2.3 Decay dynamics of quantum dots

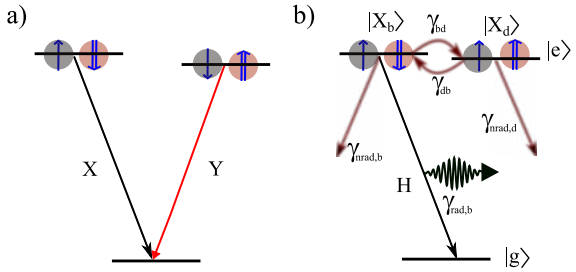

Figure 1.6: QDs as single quantum emitter. a) Level diagram of neutral exciton which displays non-degenerate excitation levels. b) Decay dynamics of a neutral exciton. The X-polarized bright exciton $|X_{\mathrm{b}}\rangle$ can emit a photon by radiatively decaying to the ground state, while the dark exciton $|X_{\mathrm{d}}\rangle$ decays to ground state non-radiatively without emitting a photon. The coupling of $|X_{\mathrm{b}}\rangle$ and $|X_{\mathrm{d}}\rangle$ occurs through spin-flip process. The fine structure splitting between $|X_{\mathrm{b}}\rangle$ and $|X_{\mathrm{d}}\rangle$ results from electron hole exchange interaction. The various transition and decay rates are indicated as well (see main text for details).

In section 1.2.1 four possible transitions have been introduced. Optical selection rules allow two transition states to decay by emitting a photon, which are the so-called bright exciton sates. The other two are called dark excitons and can only decay non-radiatively. Owing to the orbital symmetry of heavy holes Bloch functions, the two

bright states are linearly polarized in the plane orthogonal to the growth direction. For this reasons they are denoted as $|X_{b,d}\rangle$ and $|Y_{b,d}\rangle$ depending on the dipole orientation. The coupling between bright and dark states occur via a spin-flip [51, 52] process schematically shown in Fig. 1.6 b), which only shows the case of the X-dipole that spin-flips between $|X_b\rangle$ and $|X_d\rangle$. Since the transition between $|X_{b,d}\rangle$ and $|Y_{b,d}\rangle$ are negligible, the two dipoles are decoupled. When the bright exciton couples to the dark exciton via a spin-flip it decays without photon emission. This process leads to blinking of the emission and it can reduce the overall quantum efficiency of the emission. The dynamics of bright exciton decay reads as [53, 54]:

$$P_b(t) = A_f e^{-\Gamma_f t} + A_s e^{-\Gamma_s t}, \tag{1.8}$$

$$\Gamma_f = \Gamma_{rad,b}/2 + \Gamma_{nrad,b} + \Gamma_{db} + \sqrt{\Gamma_{rad,b}^2/4 + \Gamma_{db}^2}, \tag{1.9}$$

$$\Gamma_s = \Gamma_{rad,b}/2 + \Gamma_{nrad,b} + \Gamma_{db} - \sqrt{\Gamma_{rad,b}^2/4 + \Gamma_{db}^2}, \tag{1.10}$$

which indicates the transition decays biexponentially, with a combination of fast and slow decay where A_f and A_s are the corresponding decay rate amplitudes. Here, $\Gamma_{rad,b}$, $\Gamma_{nrad,b}$ and Γ_{db} are the radiative decay rates of the bright exciton state, the non-radiatively decay rate of the bright exciton state, and the bright to dark state spin flip rate. From measurements, it is possible to extract the radiative, non-radiative and spin-flip rates by fitting the equation 1.8. This allows to estimate the system quantum efficiency using $\eta = \frac{\Gamma_{rad}}{\Gamma_{rad}+\Gamma_{nrad}}$, i.e. the ratio between the radiative decay rate and the total decay rate including the non-radiative processes.

Light-matter interaction

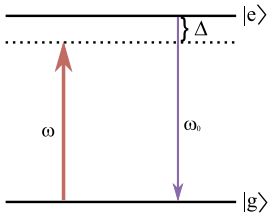

Figure 1.7: Interaction of a two-level system with a light field. The frequency of the light is ω and the spontaneous emission frequency of the system is ω_0. The detuning between the laser and the system is $\Delta = \omega_0 - \omega$

.

We now consider the case shown in Fig. 1.7 where a two-level system with resonant frequency ω_0 interacts with a (near-) resonant light field at frequency ω. The interaction

Hamiltonian H_{I} in the rotating wave approximation (RWA) is given by

$$H_{\mathrm{I}} = -\langle g|\overrightarrow{d}|e\rangle\,(E_0^{(-)}\sigma_- e^{\mathrm{i}\omega \mathrm{t}} + E_0^{(+)}\sigma_+ e^{-\mathrm{i}\omega \mathrm{t}}), \tag{1.11}$$

$$= \frac{\hbar\Omega}{2}(\sigma_- e^{\mathrm{i}\omega \mathrm{t}} + \sigma_+ e^{-\mathrm{i}\omega \mathrm{t}}), \tag{1.12}$$

where we used the TLS transition operators $\sigma_- = |g\rangle\langle e|$ and $\sigma_+ = |e\rangle\langle g|$ between ground and excited state and introduced the Rabi frequency $\Omega = \langle g|\overrightarrow{d}|e\rangle\, E_0^{(+)}/h$.

The generic TLS state vector is in the form

$$|\psi(t)\rangle = c_{\mathrm{g}}(t)\,|g\rangle + c_{\mathrm{e}}(t)\,|e\rangle\,, \tag{1.13}$$

where $c_{\mathrm{g}}(t)$ and $c_{\mathrm{e}}(t)$ are the time-dependent coefficients for the ground and excited state, respectively, and they must obey $|c_{\mathrm{g}}(t)|^2 + |c_{\mathrm{e}}(t)|^2 = 1$. In the interaction picture, Schrödinger equation reads

$$i\hbar\frac{d}{dt}\,|\psi(t)\rangle = H_{\mathrm{I}}\,|\psi(t)\rangle\,. \tag{1.14}$$

By substituting the interaction Hamiltonian, the time evolution of the coefficients $c_{\mathrm{g}}(t)$ and $c_{\mathrm{e}}(t)$ can be expressed as

$$\dot{c_{\mathrm{g}}} = -\frac{i\Omega}{2}c_{\mathrm{e}}(t), \tag{1.15}$$

$$\dot{c_{\mathrm{e}}} = -i\omega_0 c_{\mathrm{e}} - \frac{i\Omega}{2}c_{\mathrm{g}}(t), \tag{1.16}$$

The solution for Equation 1.15 and 1.16 is given by

$$c_{\mathrm{g}}(t) = e^{\mathrm{i}\Delta \mathrm{t}/2}\left[c_g(0)\cos(\frac{1}{2}\tilde{\Omega}t) - \frac{i}{\tilde{\Omega}}\left[\Delta c_{\mathrm{g}}(0) + \Omega c_e(0)\right]\sin(\frac{1}{2}\tilde{\Omega}t)\right], \tag{1.17}$$

$$c_{\mathrm{e}}(t) = e^{\mathrm{i}\Delta \mathrm{t}/2}\left[c_{\mathrm{e}}(0)\cos(\frac{1}{2}\tilde{\Omega}t) + \frac{i}{\tilde{\Omega}}\left[\Delta c_{\mathrm{e}}(0) + \Omega c_{\mathrm{g}}(0)\right]\sin(\frac{1}{2}\tilde{\Omega}t)\right], \tag{1.18}$$

where we introduced the atom-laser detuning $\Delta = \omega_0 - \omega$ and $\tilde{\Omega} = \sqrt{\Omega^2 + \Delta^2}$, which is the effective Rabi frequency in the presence of detuning. If assume the system is in the excited state initially, $c_{\mathrm{g}}(0) = 0$ and $c_{\mathrm{e}}(0) = 1$, the probability that the system is in state $|e\rangle$ is

$$P_{\mathrm{e}}(t) = |c_{\mathrm{e}}(t)|^2 = \frac{1}{2}\frac{\Omega^2}{\tilde{\Omega}^2}(1 - \cos\tilde{\Omega}t). \tag{1.19}$$

If the laser is pulsed, $\tilde{\Omega}t$ becomes $\int\sqrt{\Omega(t)^2 + \Delta^2}dt$. A single-photon source can be therefore built by exciting the QD with resonant pulses, thus making $\Delta = 0$ and adjusting the pulse power so that $\int\Omega(t)^2dt = \pi$. In this scenario all the population is transferred from one state to the other. Such pulse is therefore called π pulse.

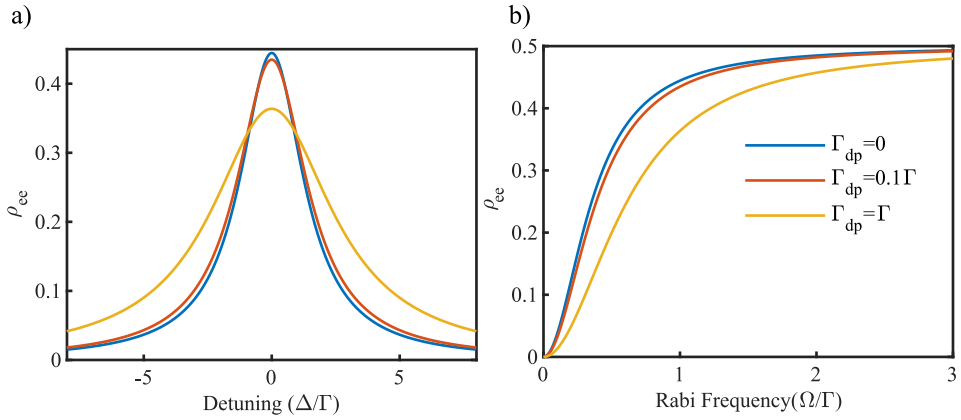

Figure 1.8: Steady-state reduced matrix of the excited state. a) ρ_{ee} is calculated as a function of normalized detuning $\frac{\Delta}{\Gamma}$ at $\Omega = \Gamma$ for different Γ_{dp}. b) ρ_{ee} is calculated as a function of normalized Rabi Frequency $\frac{\Omega}{\Gamma}$ under resonant fluorescence $\Delta = 0$ for different Γ_{dp}.

Besides the interaction with a driving field, the TLS also couples to a continuum of optical modes (or reservoir) leading to spontaneous emission according to Fermi golden rule. To take into account the coupling to the reservoir, it is necessary to use a density matrix formalism and solve the master equation [55]. Density matrix of the TLS is $\rho = \sum_i p_i \left|\psi_i(t)\right\rangle \left\langle\psi_i(t)\right|$, p_i denotes the probability of a pure sate occurring. This density matrix contains both information of the TLS and the light field, however we are primarily concerned with the TLS. Thereby, we trace out the reservoir and the reduced density matrix ρ_A for the TLS is

$$\rho_A = \begin{pmatrix} \rho_{gg} & \rho_{ge} \\ \rho_{eg} & \rho_{ee} \end{pmatrix}, \tag{1.20}$$

where $\rho_{gg} = c_g^\dagger c_g$, $\rho_{ge} = c_g^\dagger c_e$, $\rho_{gg} = 1 - \rho_{ee}$ and $\rho_{eg} = \rho_{ge}^\dagger$. We obtain the optical Bloch equations for the system:

$$\dot{\rho_{gg}} = i\Omega(\rho_{eg} - \rho_{ge}-) + \Gamma\rho_{ee}, \tag{1.21}$$
$$\dot{\rho_{ge}} = -(\Gamma_2 + i\Delta)\rho_{ge} + \Omega(\rho_{ee} - \rho_{gg}), \tag{1.22}$$
$$\dot{\rho_{eg}} = -(\Gamma_2 + i\Delta)\rho_{eg} - \Omega(\rho_{ee} - \rho_{gg}), \tag{1.23}$$
$$\dot{\rho_{ee}} = i\Omega(\rho_{eg} - \rho_{ge}-) - \Gamma\rho_{ee}. \tag{1.24}$$

Where Γ is the spontaneous decay rate, $\Gamma_2 = \Gamma/2 + \Gamma_{dp}$ is the total decay rate and Γ_{dp} is the pure depahsing rate indicating the coherence of the system is lost due to fast

interaction with environment. The steady-state solution of the TLS is

$$\rho_{ee}(t \to \infty) = \frac{2\Gamma_2\Omega^2}{\Gamma(\Gamma_2^2 + \Delta^2 + 4(\Gamma_2/\Gamma)\Omega^2)}, \tag{1.25}$$

$$\rho_{ge}(t \to \infty) = -\frac{\Omega^2(i\Gamma_2 + \Delta^2)}{\Gamma_2^2 + \Delta^2 + 4(\Gamma_2/\Gamma)\Omega^2}. \tag{1.26}$$

Figure. 1.8 a) shows the steady-state line-shape of the excited state population using equation 1.25 with different values of dephasing. The full half-maximum linewidth Γ_{FWHM} is given by $\Gamma_{FWHM} = 2\Gamma_2\sqrt{S+1}$, where we introduced the saturation parameter S given by:

$$S = \frac{\Gamma_2\Omega^2}{\Gamma(\Gamma_2^2 + \Delta^2)}, \tag{1.27}$$

which is proportional to the excitation power.

In the low-power limit the linewidth is $2\Gamma_2$. In the absence of pure dephasing, the linewidth is exactly Γ, which is the soc-called lifetime limited linewidth, indicating a perfect emitter.

If we employ resonant fluorescence on the TLS using a continuous wave (CW) laser, the excited state population as a function of S is given by

$$\rho_{ee} = \frac{1}{2}\frac{S}{S+1}, \tag{1.28}$$

showing a saturation behavior to exactly 1/2 of the population. The ρ_{ee} saturation with increasing the incident power is shown in Fig. 1.8 b).

Having developed the full dynamics of the TLS, it is possible to describe the light emitted by the QDs and study their statistical properties. The most important feature of single-photon is revealed by their second-order correlation function $g^{(2)}(\tau)$ which is measured with a Hanbury Brown and Twiss (HBT) setup (see Chapter 3 and Chapter 4 for further details). The HBT setup consists of a 50/50 beam splitter which separates the photons in two paths. Two detectors are placed at the output and their correlation provides the measurement of $g^{(2)}(\tau)$ where τ is the time difference between two clicks. A perfect single-photon source is anti-bunched, which means that the two detectors never click simultaneously, hence $g^{(2)}(0) = 0$. The second order correlation function is given by

$$g^{(2)}(\tau) = \frac{\left\langle \hat{E}^-(0)\hat{E}^-(\tau)\hat{E}^+(\tau)\hat{E}^+(0)\right\rangle}{|\left\langle \hat{E}^-(0)\hat{E}^+(0)\right\rangle|^2}. \tag{1.29}$$

Where $\hat{E}$ is the electric field operator, full expression of the photon auto-correlation function is given by [56]

$$g^{(2)}(\tau) = 1 - e^{-(3\Gamma_2/4)\tau}(\cos\sqrt{\Omega^2 - (\frac{\Gamma_2}{4})^2}\tau + \frac{3}{4}\frac{\Gamma_2}{\sqrt{\Omega^2 - (\frac{\Gamma_2}{4})^2}}\sin\sqrt{\Omega^2 - (\frac{\Gamma_2}{4})^2}\tau). \tag{1.30}$$

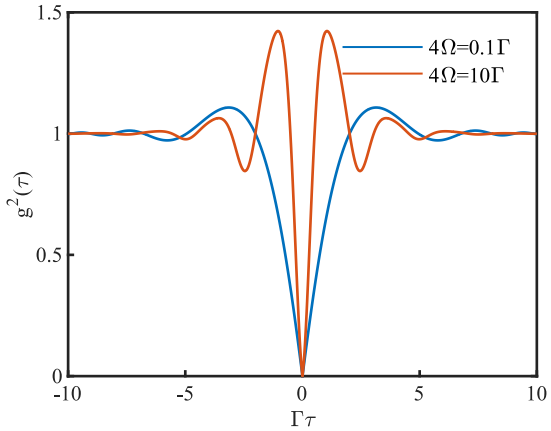

Figure 1.9: $g^{(2)}(\tau)$ as a function of delay time $\Gamma\tau$ for weak excitation (blue line) and strong excitation (red line) respectively.

As shown in Fig. 1.9, $g^{(2)}(0)=0$, and $g^{(2)}(|\tau|) > 0$ as $|\tau|$ increases. Therefore we get $g^{(2)}(|\tau|) > g^{(2)}(0)$, which is a phenomenon known as photon *anti-bunching*. For weak excitation, $\Omega \ll \Gamma/4$, $g^{(2)}(|\tau|)$ increases monotonically from 0 to 1 with $|\tau|$, while for the strong excitation, $g^{(2)}(|\tau|)$ oscillates with $|\tau|$. The oscillating magnitude dampens as $|\tau|$ increases and $g^{(2)}(|\tau|)$ reach unity when $|\tau| \rightarrow \infty$. In this project, we only focus on weak excitation regime. Chapter 4 provides further insight on the experimental details for measuring $g^{(2)}$ on photons emitted by QDs.

1.2.4 Photonic crystal waveguides

Coupling single QDs to nanostructures allows to create an efficient light-matter interface by defining and tailoring the local density of optical states (LDOS) as indicated in equation 1.7. Photonic crystal waveguides (PCW) offer a versatile tool for manipulating the LDOS. A PCW enable to preferentially and efficiently couple the spontaneous emission to a single guided mode while suppressing the coupling to radiation modes. In addition, PCW has a wide bandwidth offering optical access to various QDs with different size. Photonic crystals (PhCs) are nanostructures created by periodically altering dielectric materials with different refractive index. Here the PhCs are obtained by etching an array of air holes in the GaAs membrane (refractive index $n \approx 3.5$) as shown in Fig. 1.10 a). Light propagating in the membrane (or slab waveguide) undergoes multiple reflection due to Bragg scattering, resulting in forbidden optical frequency bands. This leads to the formation of the photonic band gap in the PhC, in analogy to the electronic band gaps in semiconductor [58].

Figure 1.10 b) shows the LDOS of a PhC (in green) as a function of frequency compared to free-space (which scales as ω^2). An ideal, infinitely long three-dimensional

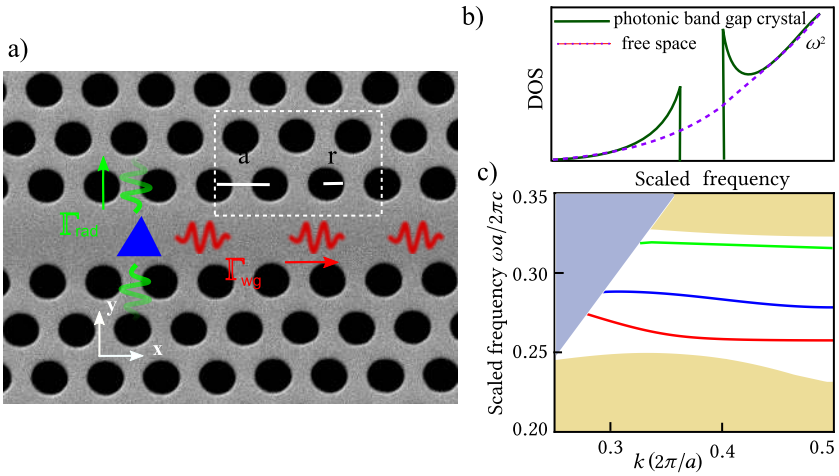

Figure 1.10: Photonic crystal waveguide (PCW). a) Top view Scanning Electron Microscope (SEM) image of a planar PCW on a GaAs membrane, a is the lattice constant and r is the radius of the air holes. The single photons emitted by QDs (blue triangle) coupled to the guided (red photons) and radiation continuum mode (green photons) are shown schematically. b) Illustration of the density of optical states of photonic crystals shown in a) circled in white. c) Band diagram of PCW, the gray blue region is the continuum of radiation modes out of the membrane confinement, the membrane modes are shaded in yellow. The solid lines are the three guided modes within the band gap, the fundamental mode is marked in red [57]

.

PhC, can virtually suppress the LDOS due to the absence of allowed optical modes. Moreover, in the proximity of the bandgap a large LDOS is observed owing to the large dispersion at the band edge.

Removing a row of holes from the perfect PhC lattice forms the waveguide shown in Fig. 1.10 a). This defects introduces new allowed bands within the photonic band gaps, corresponding to optically guided modes. The band structure of such a PCW is given in Fig. 1.10 c), where the three solid lines indicate the allowed optical modes in the photonic band gap. The lowest-energy mode is referred to as the fundamental mode (with even symmetry) and it is marked in red in the figure. The corresponding frequencies are dependent of the hole-to-hole spacing a and hole radii r and can be calculated by numerical simulations. The group velocity $v_g = \frac{dw}{dk}$ of the guided modes is the slope of the lines, which goes to zero when approaching the edge of the Brillouin zone. Therefore the group index $n_g = \frac{c}{v_g}$ diverges correspondingly, introducing a large slow-down factor.

The strength of light-matter interaction of a QDs coupled to a fundamental mode in a PCW can be quantified by the LDOS $\rho_{\mathrm{LDOS}}(r_0, \omega_0, \overrightarrow{e_0})$. The LDOS is strongly dependent on the position of the QD and the orientation of the transition dipole. The orientation of the orthogonally polarized X- and Y-dipoles in QDs are along the [110] and [1-10] crystallographic axes of the GaAs substrate [59]. Interestingly, these are

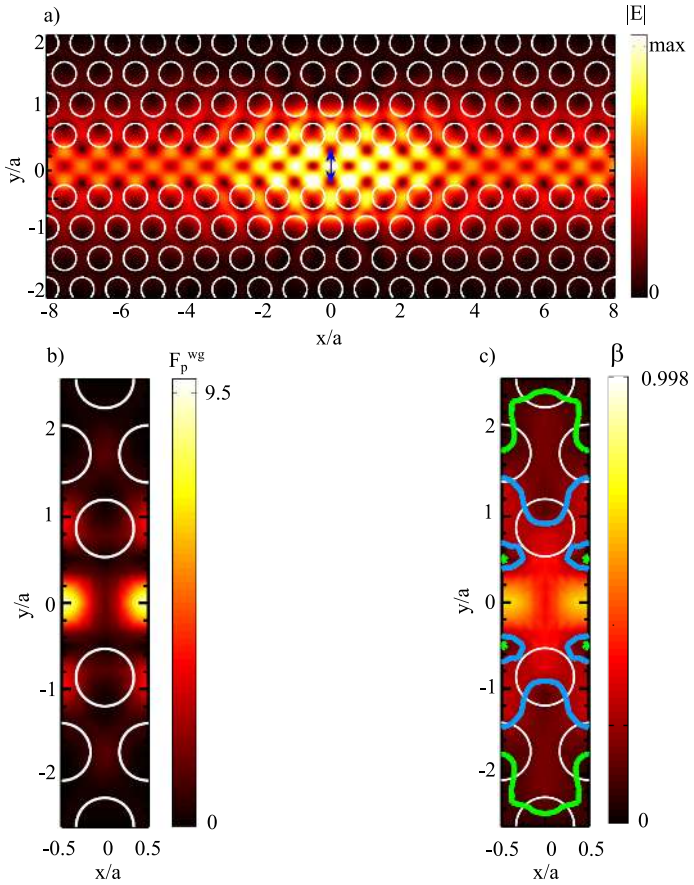

Figure 1.11: Numerical modeling of PCW, adapted from [57] a) Spatial dependence of the electric field magnitude produced by a Y-dipole located in the center of the PCW. b) Spatial map of the Purcell factor F_0^{wg} as a function of the QD position. c) Spatial map of the β factor. The blue and green contours indicate $\beta = 0.96$ and $\beta = 0.8$, respectively.

also the cleaving axes of GaAs, so they are easily identified during processing. By aligning the PCW along one of the GaAs crystallographic directions it is possible to maximize the coupling to one of the dipoles to the mode electric field. In terms of the emitter position, the best coupling is achieved for the emitter placed in the centre of the PCW as shown in Fig. 1.10 a) (blue triangle). In this case, the Y-dipole couples to the fundamental mode while the X-dipole couples to the first order mode.

Numerical modeling is used to quantify the interaction of a QD coupled to a PCW [57]. The excitation of the PCW mode by the Y-dipole is shown in Fig. 1.11 a) in the case of high group index ($n_g = 58$). The light-matter enhancement is quantified by the Purcell factor, which is the ratio of the radiative decay rate in the PCW Γ_{wg} to

radiative decay rate in the homogeneous medium (or bulk) Γ_{bulk}. It can be expressed for a transition dipole optimally aligned to the electric field and placed at the antinode of the mode profile in a PCW as [45, 60]

$$F_{\text{p}}(\omega) = \frac{\Gamma_{\text{wg}}}{\Gamma_{\text{bulk}}} = \left(\frac{3}{4\pi n}\frac{\lambda^2/n^2}{V_{\text{eff}}/a}\right) n_{\text{g}}(\omega). \tag{1.31}$$

This equation indicates how the light-matter enhancement is realized in a PCW. A tight confinement of the optical modes defined by effective mode volume (V_{eff}) and a slow v_{g} obtained in the strong dispersive PCW are required to achieve high Purcell enhancement. High F_{p} values are only achievable in a reduced area of the nanostructures as shown in Fig. 1.11 b).

PCW enable near-deterministic light-matter interaction as QDs couple very efficiently to the fundamental mode and negligibly to any other non-guided mode. This efficiency is quantified by the β factor, which is the fraction of the radiation coupled to the PCW mode defined as

$$\beta = \frac{\Gamma_{\text{wg}}}{\Gamma_{\text{tot}}} = \frac{\Gamma_{\text{wg}}}{\Gamma_{\text{wg}} + \Gamma_{ng} + \Gamma_{\text{nrad}}}, \tag{1.32}$$

where Γ_{wg} and Γ_{ng} denote the decay rate in the waveguide and to non-guided modes, and Γ_{nrad} is the non-radiative decay rate. Spatial maps of the β factor are given in Fig. 1.11 c) as a function of the emitter position. The blue and green contour correspond to $\beta = 0.96$ and $\beta = 0.8$. The color bar quantifies the amplitude of the β factor which is highly non-linear in a quite large spatial range. The dipole placed in the center of the PCW within $\pm a$ can realize $\beta \geqslant 96\%$ for experimentally achievable of $n_{\text{g}} = 58$. This indicates the significant robustness of the β factor in regard to spectral and spatial detuning in the PCW, and $\beta > 0.98$ have been experimentally demonstrated [61].

1.3 Thesis objectives and structure

In this thesis, we present the work carried out as my PhD project, towards scaling up quantum photonic technologies based on QDs in GaAs photonic integrated circuit. While tremendous progress has been made in various material platforms, the development of a fully integrated and scalable quantum photonic integrated circuit, comprising single-photon sources, reconfigurable circuits, and detectors (illustrated in Fig. 1.2), is still at its infancy. This thesis focuses mainly on novel fabrication approaches for scaling SPS with individual electrical gates and addresses some of the outstanding challenges in realizing "building blocks" that can be easily integrated and replicated in a chip. Chapter 1 served as introduction for the entire thesis framework and highlighted the basic theoretical foundations of QD-based SPS.

Chapter 2 presents the fabrication techniques utilized to produce the samples in this project. We firstly introduce the processing methods such as metal contact deposition and nano-structure patterning. A novel kind of SPS based on "local gated devices" are developed. We also summarize the common problems and corresponding solutions which occur during the sample processing.

The SPS have been characterized extensively in this thesis. Chapter 3 describes the cryogenic optical setups and the relevant measurement methods used for the characterization of the devices. Chapter 4 reports the results of the characterization of the SPS. The chapter illustrates the general principles used to assess the properties of a SPS and reviews the state-of-the-art of high quality SPS realized with QDs on different systems.

In Chapter 5, the various decoherence mechanisms consisting of charge noise, spin noise and phonon in In (Ga)As QDs coupled to nano-devices system are presented. The effect of phonons on the indistinguishability of photons emitted by QDs coupled PCW is characterized experimentally.

Chapter 6 addresses the problem of waveguide loss in the GaAs platform. We provide a full analysis of the loss mechanisms involved in single-mode waveguides. In particular, the loss caused by the Franz-Keldysh electroabsorption in *n-i-p* junctions is measured experimentally and approaches towards the reduction of such losses are discussed.

Scaling up to multiple devices that can be independently controlled (for example integrating SPS and switches) has also been explored. While this is still an ongoing activity, chapter 7 presents some preliminary results, provides an outlook of the future work, and a conclusion to this work.

CHAPTER 2

Nano-fabrication of quantum photonic devices

Description of the fabrication techniques of quantum nanophotonic devices in GaAs membranes, with a focus on the newly developed localized gates for QDs.

As presented in chapter 1, QDs coupled to nanostructures constitute a promising platform for the generation of high quality single-photon sources (SPS). To achieve this, a combination of high-quality MBE grown material and fabricated nanophotonic structures with high yield is needed. Nano-fabrication techniques for quantum devices have benefited from the advances of miniaturization of microelectronics and enable today the realization of few nanometers-scale devices, making quantum experiment on a chip possible. The devices implemented in this project are fabricated on a GaAs heterostructure membrane with embedded self-assembled QDs. The layout of the layer structure is shown in Fig. 1.4. As an example of the devices developed in this thesis, Fig. 2.1 shows a scanning electron microscope (SEM) image of a photonic crystal cavity (PCC) coupled to suspended nanophotonic waveguides. The PCC is surrounded by shallow-etched trenches that electrically insulate it from the rest of the chip, and by a metal contact deposited next to it. These so-called "local" contacts have been specifically developed in this thesis and constitute the key to scale up the circuit elements.

In this chapter, an overview of the fabrication processes for quantum photonic devices based on quantum dots in gallium arsenide (GaAs) is given and the main challenges towards developing scalable circuit building blocks are addressed. Part of the results in this chapter have been published in [62].

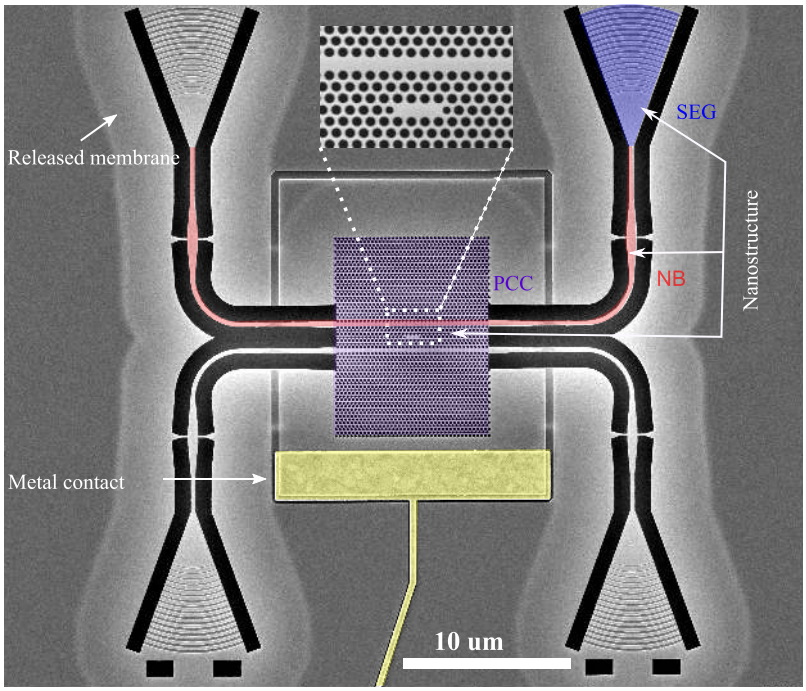

Figure 2.1: Scanning electron microscope (SEM) image of a nanophotonic device with electrical contacts. It consists of several components: metal contacts, photonic crystal cavities (PCC, shaded in purple), nanobeam waveguides (NB, colored in red), and focusing shallow etched grating (SEG, shaded in blue). The entire device is realized on an under-etched suspended GaAs membrane.

2.1 Nanofabrication methods

The complete fabrication procedure implemented in this project consists of three main steps:

I. Definition of *p*-type and *n*-type metal contacts.

II. Etching of isolation trenches and gratings.

III. Nanostructure definition and membrane undercut.

The detailed fabrication recipe is provided in appendix A.2. Each of these steps comprises a series of standard nanofabrication techniques for pattern definition (lithography), etching, or deposition, which are illustrated below.

2.1.1 Lithography

Lithography is a process which transfers designed patterns to a polymeric film called resist. The resist is usually sensitive to either electrons or photons (or sometimes both),

which, by interacting with the resist's polymeric chains being exposed, change its solubility in a chemical solution called developer. The chemical reactions during the exposure can be of two kinds depending on the nature of the resist. If the chemical bonds between the molecules break, it will make the exposed areas more soluble to the developer, then this polymer is called positive resist. On the contrary, the exposure generates new bonds between molecules (cross-linking) and the exposed areas will not dissolve in the developer. This kind of the resist is called negative resist. According to the nature of the exposure source, there are two types of lithography. One is photo-lithography which uses light source, and the other is the electron beam lithography (EBL), employing electrons. In this work, I used EBL exclusively, using a high-resolution positive electron beam resist ZEP520A [63].

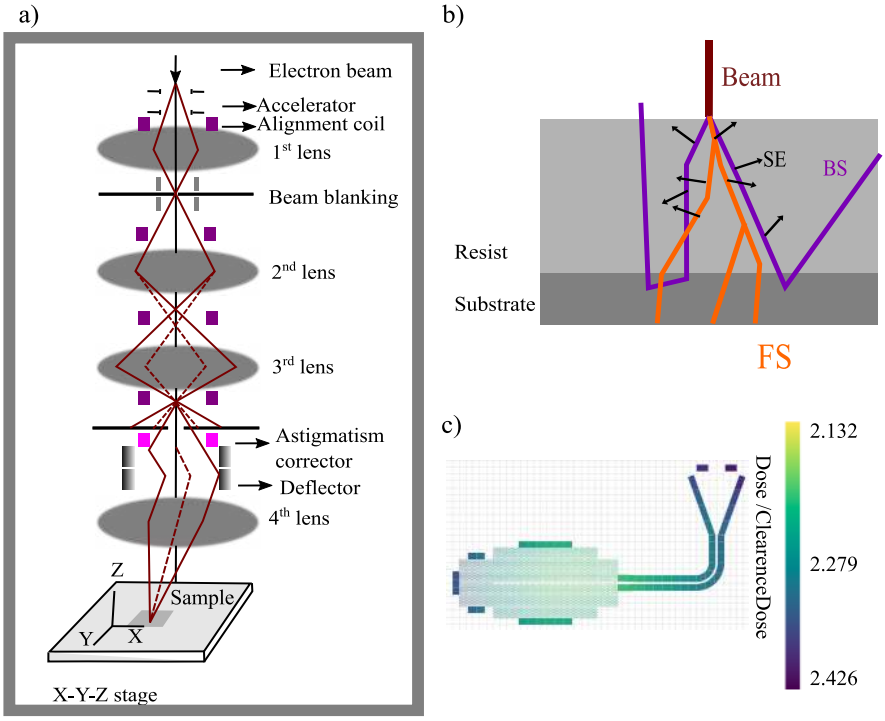

Figure 2.2: Electron beam lithography (EBL). a) Sketches the central part of EBL system. b) Proximity effect caused by electron scattering in the substrate. Forward scattering (FS, orange line), back scattering (BS purple line) and the low-energy secondary electrons (SE,black line with arrow), are shown. c) Shows an example of applying proximity effect correction(PEC) on a nanodevice of photonic crystal waveguide for exposure dose calculation. The color bar gives the ratio of the calculated dose to the clear dose.

The EBL enables to pattern features with resolution down to the few-nm scale. Fig. 2.2 a) sketches the main body cross-section of an EBL system. It is composed of a column for accelerating the e-beam, beam blankers for tuning on/off the e-beam with

high speed, a set of electromagnetic lenses for shaping the beam, an alignment coil for calibrating the beam and correcting for astigmatism, and a beam deflector for steering the beam on different regions of the substrate [64]. The beam accelerator defines the electron energy (in keV) and thus determines the electron's De Broglie wavelength according to $\lambda = \hbar/p$, which is usually well below 1 Å. The beam focus system consists of four electromagnetic lenses, which provide the same focusing mechanism as a scanning electron microscope. The main difference is that the second and third lenses are positioned after the focusing lens aiming at fixing the focal point on the fourth lens. The advantage of the this design allows to write patterns over a range of several hundreds of nanometers with high stability. Once the electron beam spot is focused on the sample, exposure is performed using electrostatic deflectors to drive the beam spots precisely on the intended sample position.

The final resolution and the smallest feature size is determined by the diameter of the e-beam after focusing and by the interaction with the resist/substrate. A beam diameter of few-nm is readily realizable in state-of-the-art EBL systems especially with high-voltage acceleration. In this work, I used an Elionix ELS-F125 [(1)], which allows reaching beam spots as small as 1.7 nm with 1 nA currents. The beam diameter is therefore small enough to define the photonic nanostructures with high precision.

The main limitation in writing resolution stems from the interaction with the resist. This is shown schematically in Fig. 2.2 b). When the incident electron beam hits the resist, it undergoes multiple scattering events which deflect its initial trajectory and "blur" the beam. In the resist, the beam is deflected with small angles (forward scattering) due to the low-Z numbers of the chemical species in the resist (C, H, Cl). However, in the substrate, Ga and As atoms cause additional back scattering and reflect some of the electrons towards regions of the resist far from its incident position. The secondary electrons produced in the process are the main contributions to the resist exposure. The additional exposure caused by back-scattering is known to produce a proximity effect, which broadens the effective exposure area in the resits leading to an increase of the minimum feature size of the patterns.

In order to minimize the proximity effect, we apply proximity effect correction (PEC) algorithm when calculating the dose to be assigned to each feature. The dose (units of μC/cm^2) is the amount of electrons per unit area quantifying the energy transferred to the resist. PEC is performed according to the beam point spread function (PSF), which is commonly modeled using a double Gaussian model

$$P(r) \approx \frac{1}{\pi(1+\eta)}\left(\frac{1}{\alpha^2}e^{-\left(\frac{r}{\alpha}\right)^2} + \frac{\eta}{\beta^2}e^{-\left(\frac{r}{\beta}\right)^2}\right) \tag{2.1}$$

In Eq.2.1, the first (second) term indicates the contribution of the forward (back) scattering to the total energy. α and β are the corresponding interaction radii of the two scattering processes. The coefficient η is the ratio between the two parts. Commercial software are developed to simulate the PSF for a variety of combination of resist and substrates. In this project, Beamfox Proximity[(2)] is used to calibrate the exposure dose

(1) https://www.sts-elionix.com/product/els-f125/
(2) https://www.beamfox.dk/

and the detailed description can be found in [65]. Fig. 2.2 c) displayed the dose distribution after PEC using Beamfox for a nano-device with a feature size of ~ 100 nm on GaAs substrate coated with ZEP 520. For such a small structure, the exposure dose is as large as > two times the clear dose and varies depending the surrounding features. In this specific case, the α, β and η are 0.014 μm, 15.776 μm, 0.7779, respectively.

Despite the high voltage (125 kV), which reduces the beam spot size (i.e., improve the focus) and reduces the forward scattering [64], a PEC is required to expose large patterns containing both small and large features. This ensures high quality and reproducibility through multiple fabrication steps. Furthermore, the reproducibility is improved by using a low-temperature (~ −5 °C) development of the e-beam resist. Low-temperature development improves the resolution of the e-beam resist and its sensitivity making the developed patterns less rough and reducing the achievable feature size [66].

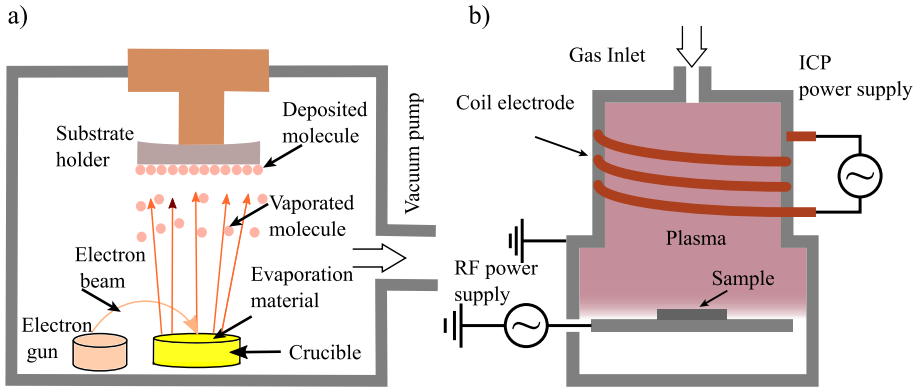

Figure 2.3: a) Metal deposition chamber using electron beam evaporation. An electron beam hits the metal source pocket mounted in the crucible (yellow cylinder) and vaporizes it under vacuum. The evaporated metal (pink circles) deposits on the substrate where the sample is mounted. b) Schematic of the inductively coupled plasma reactive ion etching ICP-RIE system. This figure adapted from [65]

.

2.1.2 Metal deposition

Electron beam evaporation is a kind of physical vapor deposition technique, shown in Fig. 2.3 a), where a stream of electrons emitted from an electron gun are used to melt and evaporate a metal in a vacuum chamber. Subsequently, the vaporized metals deposit on a substrate and form a thin layer. In this system, the electron gun is used to produce a beam of electrons, while the crucible contains all the materials needed for evaporation in different pockets, which can be selected via an external control. The e-beam current and postion is also controlled externally to gradually and uniformly evaporate each specific target metal according to its melting point. By selecting different pockets sequentially, arbitrary metal layer stacks are defined. The

machine used in this project is a Polyteknik Flextura system [(3)] which enables fully automated and programmable operation.

To define a metal pattern, a technique known as lift-off is used. First, a pattern is defined by EBL using ZEP520 and developed. Then the sample is loaded in the evaporator and a metal sequence is evaporated. The sample is left in a N-Methyl-2-pyrrolidone (NMP) solution heated to 80 °C for approximately 10 minutes, during which the resist is dissolved and lifts off the metal in the unwanted regions. Further immersion in a gentle ultrasonic bath enables cleaning the surface from residues. In this way, thin lines and arbitrary-shape metal contacts can be patterned on the sample.

The metal layers used to achieve ohmic behavior on *p*-type and *n*-type GaAs have been developed in previous work [65]and consist of a Ni/Ge/Au stack for *n*-type GaAs and Cr/Au for *p*-type GaAs. The *n*-type contact is fabricated first, as it requires rapid thermal annealing (RTA) at 420 °C to form an alloyed ohmic contact. Moreover, the *n*-layer acts as a single ground plane for the entire chip. The *p*-type contact instead does not require alloying, as the surface of membrane contains a high-doping layer with a concentration exceeding 10^{19} cm^{-3}, but it can be patterned to form isolated *p-i-n* diodes. Here, Cr is preferred as adhesion material, which is also compatible with hydrofluoric acid etching.

2.1.3 Dry etching

Dry etching is an etching process involving physical and chemical mechanisms, which enables controlling the anisotropy of the etched profile. The etching occurs in a reaction chamber with a gas plasma. In the physical process, the positive ions are accelerated with high kinetic energy to bombard the sample surface. Part of the energy is transferred to the sample surface atoms results in a sputtering process, which leads to vertical and sharp etched features. Chemical interaction of the incident ions with the substrate surface usually forms volatile products, which can be evacuated by the vacuum system. Chemical etching selectively removes the material in an isotropic manner.

In this work, an inductively coupled plasma (ICP) reactive ion etching (RIE) system (Oxford Instruments PlasmaLab 100) is used to etch GaAs/AlGaAs membranes in two different configurations depending on the required etching detph. The reaction chamber is schematically shown in Fig. 2.3 b). The ICP-RIE system provides two independently controlled radio-frequency RF sources, one required to strike the plasma and perform the RIE process, and one controlling the coil for ICP. During operation, a voltage difference is created between the bottom electrode where the sample is placed, and the walls of the reaction chamber, enabling the accelation of chemical specimens towards the sample. Without the ICP, the RIE process provides a well controllable etching process, but the etching rate and anisotropy are compromised, especially in small features below 500 nm. Enhancement of the etching rate and anistropy are possible by adding the second power source of ICP power supply. The ICP process can largely

(3) http://www.polyteknik.com/products/industrial-pvd-systems/flextura-evaporator/

increase the plasma density in the chamber to enhance the etching rate, while the plasma energy can be on a low level for good selectivity.

GaAs can be etched in a mixed plasma of Cl_2 and BCl_3 gases diluted in argon at low pressure ~ 4.7 mTorr [67]. Both RIE and ICP-RIE are performed in this project. RIE is used for shallow etching of features with depth ~ 100 nm required for, e.g. etching trenches and grating couplers. The nanostructures such as photonic crystals and waveguides are instead etched by ICP-RIE, which ensures sharp and vertical etching. In both cases, the desired pattern is first defined with EBL using ZEP520. Unfortunately, the e-beam resist is not the most suitable mask material for dry ething, as it has relatively poor selectivity. For ICP etching, a ZEP thickness of 550 nm is needed so that the smallest features (holes with a radius of 55 nm) can be successfully etched through the membrane. However, the plasma burns the surface of the photoresist leaving non-volatile residues (commonly known as "crusts") which are hard to remove after fabrication. Using an intermediate hard mask (e.g. SiN or SiO_2 thin film) would alleviate such issue. However, the equipment for thin film deposition and etching of hard masks was unfortunately not available throughout this project.

2.1.4 Wet Etching

Unlike dry etching, wet etching is typically isotropic leading to significant loss of the critical dimensions. Thus it is not used to etch photonic nano-devices. However, the nature of wet etching of high selectivity and high etching rate makes it attractive for non-critical size etching like the membrane undercut. In this project, wet etching is mainly used to underetch and release the membranes from the substrate and subsequent cleaning of non-volatile products produced by dry etching. The undercut is performed in a 5 % solution of hydrofluoric acid (HF), which attacks the AlGaAs layer below the membrane but is completely selective to GaAs.

2.2 Scalable nanophotonic devices with electrical gates

The gates implemented in the *p-i-n* heterostructure membranes offer the opportunity to Stark-tune the emission frequency of QDs, and control the charge surroundings of the QDs and thereby minimize the decoherence caused by charge noise. Especially towards achieving the latter goal, which enables building indistinguishable single-photon sources, it is crucial to fabricate high-quality devices with ideal diode behavior. However, it is quite complicated to make such a high-quality gate because of the defects of the material and imperfection of the fabrication. The quality of the metal gates can be quantified by measuring the current-voltage (I-V) characteristics of the diode. The presence of leakage currents or early turn-on behavior usually indicate a malfunctioning device which will not result in coherent single-photon emission. While the physical mechanisms that correlate the leakage currents in the membrane and QD stability are not yet fully understood, experimental evidence suggests that leakage currents add extra noise to the voltage gate. One possible explanation, is that leakage occurs in bursts, as a local breakdown (e.g. avalanche process) that makes the voltage

across the device fluctuate. Consequently, a Stark tuning noise is imposed on the QDs, leading to spectral diffusion. Another common issue is the device area. The larger is the *p*-*i*-*n* diode area, the higher is the opportunity to include defects. Moreover, a large area leads to a large diode capacitance, which slows-down the response time of the gate.

This thesis addresses the above issues by devising a novel design with smaller diode capacitance and an optimized fabrication method for creating local gates. The fabrication problems can be classified into two categories. Firstly, both material defects and fabrication imperfection have the potential to short circuit the *p*-doped layer with the *n*-doped layer. Second, erosion effects, such as photochemical etching, can produce trenches around the *n*-type contacts which can change the carrier density and deteriorate the gates performance. Another important factor for high quality gate is the selection of metal, which should have good conductivity, good adhesion and Ohmic behavior. A series of optimized recipes that address the above issues are provided in Appendix A.2.1.

In the following, the concept of "local" gates is introduced and the I-V curves are compared to the previous generation of devices.

2.2.1 Characterization of local metal gates

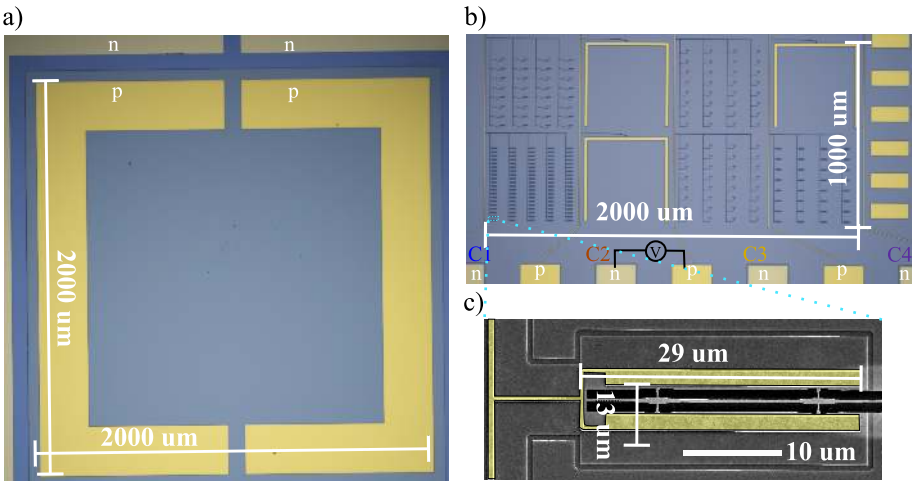

Figure 2.4: Local metal gate designs. a) Optical microscopy image of previous devices consisting of a pair of contacts and a large square device area. b) The optical microscopy of the devices realized in this work, where individual devices with localized *p*-contact are connected in parallel. The devices are arranged in columns and connected to a *p*-type bonding pad (small yellow squares in the bottom) and isolated by shallow-etched trenches. All the *n*-type contacts are grounded. c) SEM image of a single device with *p*-type contact isolated from the rest of chip by trenches.

Figure 2.4 a) displays the layout of the square gates used in the past and commonly found in the literature [68], on which the voltage bias applied across the *p-i-n* diode extends over an area of $A_{SM} = 2 \times 2$ mm^2. Owing to its large capacitance, such devices resulted in a response time in the millisecond time-scale, i.e. slower than the typical charge-noise fluctuations. A new generation of QD gated samples (shown in Fig. 2.4 b) and c)) have been designed to improve the response time. Essentially, the proposed design features metallic wires reaching the individual samples, thereby reducing the resistivity of the diode (i.e. the sheet resistance). Additionally, the wires and the gated devices are entirely isolated by shallow-etched trenches that isolate the *p*-doped layers and enable addressing each device independently.

In practical experiments, multiple devices are connected in parallel and arranged in a column layout (indicated with the letter C in Fig. 2.4b). Each column is connected to a large square metal pad used for wire bonding to the experimental apparatus. While this layout increases the device capacitance, it still significantly suppresses the sheet resistance. The localized *p*-contact has an area of $A_{MM} = 29 \times 13 \mu$m^2. Compared to the old design, the new generation exhibits the remarkable advantage that the material defects and fabrication imperfections are minimized, thereby improving the total yield. Statistic data from our fabrication indicates the yield of the squared contacts was $\sim$ 50 % while the new sample can reach $\sim$ 80%.

Figure 2.5 a) show the cryogenic temperature I-V curve of the best-fabricated square mesa (blue line), compared to the micro-mesa, and the leakage current is several orders of magnitude larger. The I-V curves have been tested on various gates. As shown in Fig. 2.4 b), the voltage bias in each single columns are independently controlled due to the fact p-contacts are isolated using the trenches shown in Fig. 2.4 c). This offers the potential to obtain scalable single photon sources using independently manipulated stark tuning of different QDs into the same emission frequency. The corresponding I-V curves at cryogenic temperature of the four columns are shown in Fig. 2.5 b). C1 and C3 exhibits an ideal diode I-V behavior. The current slightly fluctuates around 10 pA when the voltage bias is applied from -1 V to 1.4 V. However the leakage current in C4 increases drastically when the voltage bias go beyond 0.8 V. C2 is an example of unsuccessful gate. The voltage bias required to turn on the QDs embedded in the membrane A.1 is around 1.2 V. C1, C3 and C2 gates enable to perform the neutral exciton stark tuning perfectly, while C1 and C2 gates can even perform high level of negatively-charged exciton states.

The response time of the diode is characterized by measuring the *RC* time constant, $\tau_{RC} \propto R\frac{\epsilon A}{d}$, where d is the distance between the *p*-doped and *n*-doped layer, which is $\sim$ 100 nm, R is the total sheet and contact resistance, and A is the area of the active charge-tunable region. Compared to the square gates design, where every single device has an effective gate area as large as A_{SM}, the speed performance of the device with localized gates is improved thanks to the isolation trenches which greatly reduces the effective charge-tunable region.

To measure the *RC* constant, resonance fluorescence, discussed in detail in Chapter 3, is performed on a QD. The photons emitted by the QDs are used as a probe to quantify the electrical switching time response to an applied voltage bias. The results

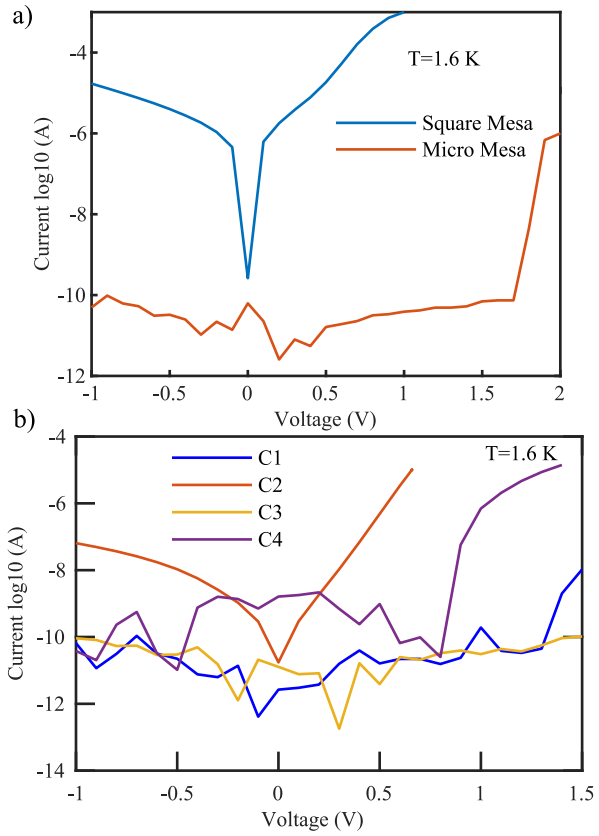

Figure 2.5: Measured current - voltage (I-V) characteristic of the *p-i-n* diode. a) A comparison of I-V curves of the square mesa (blue line) with the micro mesa (red line) at cryogenic temperature T=1.6 K. b) I-V curves from four independent mesas corresponding to the four independent gates in Fig. 2.4 b) labeled them as C1, C2, C3, C4.

are shown in Fig. 2.6. The QD is resonantly excited by a continuous-wave laser, and the gate voltage is sinusoidally modulated around the resonant voltage of the QD. A bias-tee is used to combine the DC and AC voltage source. The DC source V_{DC} is the resonant voltage of the QD and it is offset by a sinusoidal AC source V_{AC} with a peak-to peak amplitude of 100 mV sketched in the inset of Fig. 2.6, which is far larger than the QD linewidth. The modulation tunes the QD in and out resonance and thereby modulates the intensity of the emission shown in Fig. 2.6. We measure the time-averaged fluorescence intensity as a function of the AC source frequency. The time-averaged QD emission intensity $I_{QD}(f_{AC})$ reads as

$$I_{QD}(f_{AC}) = I_0 \int_{-A(f_{AC})}^{A(f_{AC})} S(V - V_{DC})dV \tag{2.2}$$

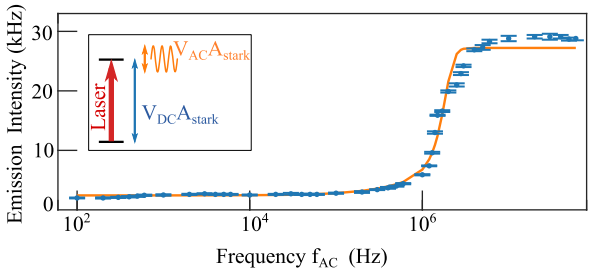

Figure 2.6: Response time characterization of local gates. The blue data points are the average emission intensity of the resonance fluorescence of a QD under AC modulation with frequency f_{AC}. A clear threshold at around 2 MHz, indicates the cut-off of the *RC* circuit formed by the diode and the contact resistance. The fitting curve of the data is shown in orange and gives the *RC* time constant τ_{RC} = 0.4 μs [62].

where $A(f_{(AC)}=(V_{AC}/2)\exp[-2\pi f_{AC}\tau_{RC}]$, $S(V\text{-}V_{DC})$ is the voltage response of the QD, I_0 is the intensity under resonant excitation without voltage modulation.

This measurement is based on the attenuation of the emission intensity when tuning the voltage applied on the QD. When the frequency is much larger than the response time, the average intensity increases because the QD can not follow the AC source and thereby emission intensity is saturated to the average voltage value. If the frequency is close to the device *RC* response time, the intensity will exponentially increase until it saturates.

The *RC* time constant τ_{RC}=0.4 μs is obtained in this experiment, and the resistance *R* is estimated from the I-V curve given in 2.5 a) (red line) by fitting the forward bias section with equation. 1.4, is 7 kΩ. The effective charge-tunable area of an entire column of devices in parallel in the current configuration is a bit less than 0.5×2 mm^2. However, if there is only a single device with a local contacted gate as shown in Fig. 2.4 c), the switching speed could be boosted to few ns scale.

2.3 Fabrication results

In the following, the results of the nanofabrication optimization and the remaining challenges are reviewed.

2.3.1 Device yield and accuracy

Several designs of nano-devices, such as the nanobeam waveguide shown in Fig. 2.9 c), photonic crystal wavegudes (cf. Fig. 2.7 a), and dual mode waveguides for in-plane resonant excitation (see Chapter 4) [69], have been tested and fabricated with near-unity structural yield (i.e. without collapsing or damaged features). Moreover, the localized QD gates show nearly ideal I-V behaviors with >90% yield, which suggests that scaling to multiple devices in the chip is possible. To connect multiple devices with nanophotonic waveguides, a method that allows trenching the *p*-layer on a waveguide with low-loss has been devised. This is required as high-density currents can otherwise

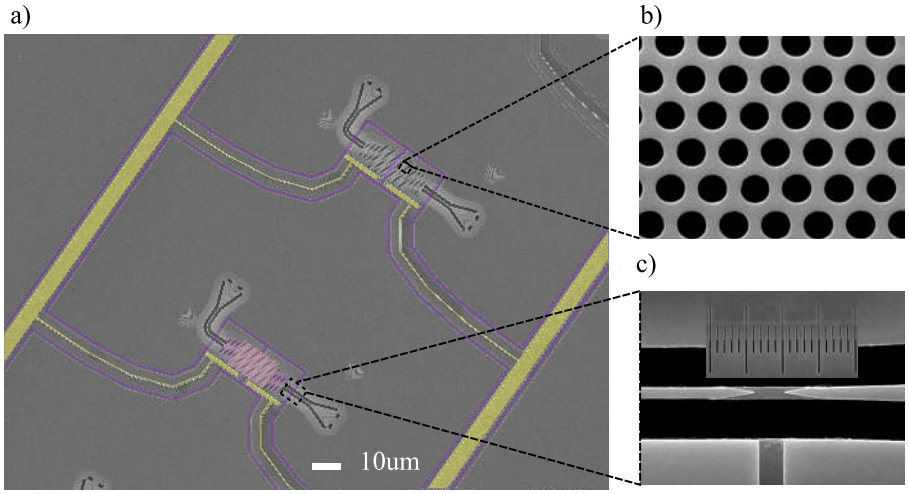

Figure 2.7: SEM images of the device produced using the optimized fabrication recipe. a) Device for on-chip tuning of two QDs in a photonic crystal waveguide (PCW), with isolation trenches (solid purple line). b) Detail of the photonic crystal region used for estimating the reproducibility of the hole radii. c) 'Butterfly' trenches used to isolate two regions across a waveguide without optical loss. (Inset) Nonius pattern to illustrate alignment accuracy below 20 nm achieved with EBL.

propagate on the waveguide surface when two devices are biased at different voltage. As shown in Fig. 2.7 c), a shallow-etched 'butterfly' trench is used to isolate the photonic crystal diode from the rest of the circuit. The trench is shaped in such a way that the light is adiabatically transferred to a thinner section of a membrane and then back. This allows electrical isolation without optical loss. As this is fabricated in two EBL steps, great alignment accuracy (below 20 nm) is required and routinely achieved (see inset of Fig. 2.7c, where a nonius structure is used to measure the alignment error).

The high resolution of EBL and applied PEC on exposure dose, enables to produce the nano-features with very high precision. The fabrication accuracy of two typical devices measured on more than 10 devices are listed in table 2.3.1. It indicates that the difference between design and measurement for the photonic crystals shown in Fig. 2.7 b) is < 6 nm, for nanobeam in Fig. 2.9 c) <8 nm, which indicates that nano-devices with a feature size of ~ 150 nm with high fabrication accuracy has been realized in our soft-mask based nano-fab platform.

	PCW – r (nm)	NB – r (nm)
Design	135	140
Fabrication	137 – 141	145 – 148
Difference	2 – 6	5 – 8

Table 2.3.1 The hole radius (r) value of the designed, and fabricated devices of PCWs and NBs, as well as the size differences between design and fabrication.

2.3.2 Device uniformity and reproducibility

The device uniformity is mainly affected by variations in the resist thickness and etching process from run to run. It can be quantified by optical characterization. For the nano-features like photonic crystals and waveguides etched using ICP-RIE, the size variation is mainly caused by the non-uniformity of the resist thickness. Transmission measurements (see also Chapter 4.3) of PCWs with identical parameters in the same chip and in different chips are shown in Fig. 2.8 a) and c) respectively. Fig. 2.8 a) shows the cut-off wavelength of five PCWs with lattice constant a=240 nm and radius r=64 nm to be between 939.5 nm and 942.5 nm, so the maximum cut-off wavelength shift from one device to another is ~ 3 nm. Fig. 2.8 c) shows that the the cut-off wavelengths of 947.4 nm and 950.9 nm for the PCWs with identical a=248 nm and r=70 nm but produced in 2020 and 2018, again with a 3.5 nm shift, which is comparable to the shift observed in the same chip, indicating a high reproducibility over time.

The focusing shallow-etched gratings (SEG) (Fig. 2.1) are etched by RIE and the end point is controlled manually. In the same chip, the uniformity of the SEG is determined by uniformity of the resit thickness. As displayed in Fig. 2.8 b), the transmission profiles of five single mode NBs connected with pairs of SEGs fully overlap. This enables reliable loss measurements within the same chip, using cut-back methods as illustrated in Chapter 6. However, the SEG central peak shift can be as large as ~ 20 nm from one chip to another as shown in Fig. 2.8 d). This is because of the etching depth variations on different chips. The QD emission wavelength is typically around 930 nm at cryogenic temperature, so the central wavelength of SEG is also designed to be 930 nm, corresponding to etching the grating grooves to a depth of 50 nm [70]. The SEG depth of the chip processed in 2020 is ~ 53.3 nm, while it is ~ 74.6 nm for a chip produced in 2018. This discrepancy leads to a central peak wavelength difference of 21.3 nm. As SEGs ultimately determine the collection efficiency of single photons from the chip, their reproducibility is of utmost importance and further work is required towards a more deterministic fabrication process.

2.3.3 Non-volatile residues and sample cleaning

As mentioned earlier, a long-standing issue in using a soft resist mask for ICP etching, is the production of non-volatile compounds produced during ICP etching. These residues are shown in Fig. 2.9 a). Their main effect is to increase surface and side-wall roughness and therefore to cause more propagation loss and unwanted scattering. Moreover, the residues make it impossible to perform any surface passivation, which could decrease the surface states [71] and reduce absorption. Therefore, it is necessary to dissolve such residues for further improving the devices performance. Several attempts have been made to remove the residues. Using oxygen plasma instead of hot NMP to remove the resist after ICP etching, still leads to a large amount of tiny residues on the surface as shown in Fig. 2.9 b). On undoped wafers, the residues are typically removed using a digital etch process, consisting of an immersion in concentrated hydrogen peroxide, followed by de-oxidation. This process is however too aggressive for the doped chip as

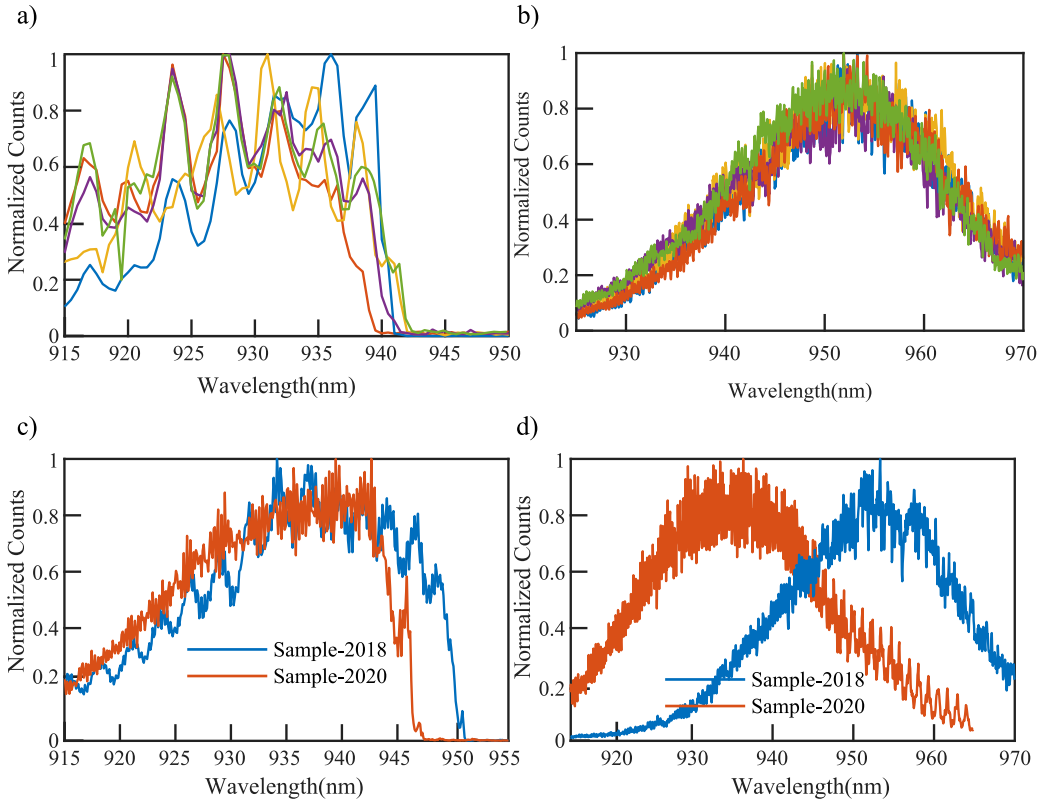

Figure 2.8: Optical device characterization to illustrate fabrication precision and uniformity. a) Transmission profile of five PCWs with identical lattice constant (a=240 nm) and radius (r=64 nm). b) Transmission profile of five pairs of shallow etched gratings connected by nanophotonic waveguides. c) Transmission profile of two PCWs with identical lattice constant (a=248 nm) and radius (r=70 nm) produced over different years. d) Same as c, but for SEGs fabricated in different years.

it leads to enlarged features as shown in Fig. 2.9 c), and to contact erosion. Moreover, it is known to seriously erode the surface and side wall, likely producing more surface states and deteriorating the devices performance. Fig. 2.9 d) reveals an increased surface roughness when the SEM image is taken at an angle. Presently, there is no known method to remove the residues efficiently in a doped sample and it is likely that a hard mask method will be required in the future to further improve the sample quality.

* * *

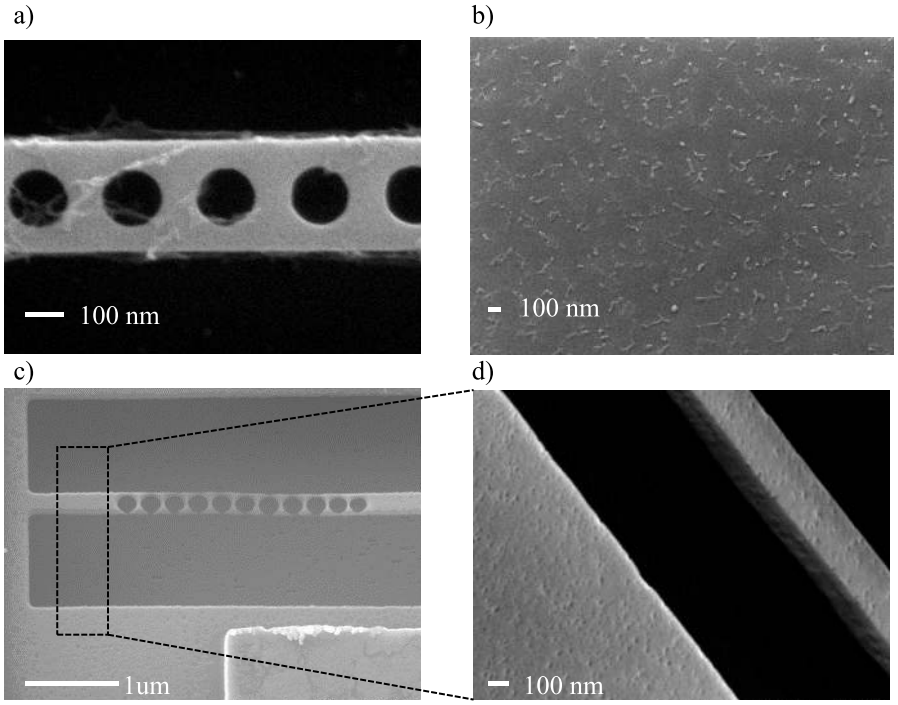

Figure 2.9: High resolution SEM images reveal the defects occurring during the sample processing. a) Example of photonic crystals with non-volatile residues due to ICP etching. b) GaAs surface after oxygen plasma cleaning of the residues, showing permanent residues even after treatment. c) Feature degradation and d) surface erosion after chemical etching of the residues in a H_2O_2 solution. While the residues are no longer observed, the features appear enlarged and the roughness has visibly increased.

In conclusion, this chapter illustrated the nano-fabrication techniques for producing quantum photonic circuits in GaAs membranes with embedded QDs. The new generation of localized QDs gates have been developed, which exhibit remarkable advantages over the previous ones in terms of device yield, speed, and scalability. The main results from the fabrication have been presented together with some outstanding challenges which are yet to be addressed. Yet, with such devices, high-quality single-photon sources have been developed and will be illustrated in the following chapters.

CHAPTER 3

Experimental methods

Describing the optical apparatus utilized to measure quantum nanophotonic devices and the methods for quantum dot excitation.

3.1 Optical setups

The single-photon source (SPS) characterization setups require a cold (< 10K) and stable sample chamber and free-space optics for coupling light in and out of the chip. Additionally, low-noise electrical connections, which play an important role in the generation of indistinguishable photons, are needed. An ideal setup decouples the environment noise and minimizes the path loss. This section presents the two main setups used in this thesis, and the optics required for excitation of QDs and collection of single-photons.

3.1.1 Liquid helium flow cryostat

The helium flow cryostat uses circulating liquid helium to cool the sample, placed in a vacuum sealed chamber, to ~ 4K. It can be cooled down and stabilized in just a few hours, which allows us to perform quick characterization on newly fabricated samples, with the goal of assessing the sample quality. Prior to in-depth characterization of a SPS, it is necessary to estimate the density of QDs, their spatial distribution, emission spectrum, and a reference brightness.

Figure 3.1 schematically shows the configuration of the setup. There are several possible excitation laser inputs (illustrated in the upper left corner of the figure): a pulsed Ti: Sapph laser, Mira 900, or a pulse laser diode (PLD) are used to excite QDs.

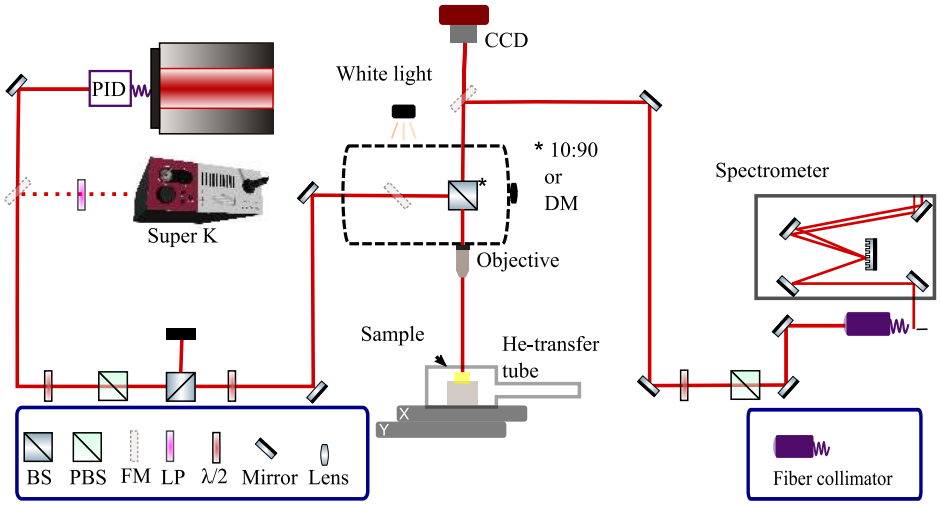

Figure 3.1: Schematic layout of the flow cryostat setup for device characterization.

The input power is controlled and stabilized by a homemade proportional-integral-derivative (PID) controller. Alternatively, a super-continuum laser light (Super K, from NKT Photonics) is used for transmission measurement and broadband characterization.

The two different light sources can be swapped using a flip-mounted mirror (FM). The optical path marked by solid red lines indicates the optical input on the left side and the output path on the right side. The excitation laser is coupled to fibers and guided free-space through a half-wave plate $\lambda/2$, a polarized beam splitter (PBS), a 50:50 beam splitter (BS) whose reflection port is aligned to a power meter (PM) to monitor the input power in order. Then goes through an additional half-wave plate used to control the polarization of the input laser. Light is subsequently coupled f to a microscope unit (Olympus BXFM), shown with a black dashed line in Fig. 3.1, which allows us to switch between white light and laser. Resorting an objective (NA 0.6), light is guided and focused on the sample surface via a 10:90 beam splitter (BS) or a dichroic mirror (DM) with a cutoff wavelength at 870nm. The microscope with a position controllable mirror, which determines the emission light from the sample, is either sent to a charge-coupled device (CCD) camera for imaging or to the collection path. The collection path includes a half-wave plate used to control the light polarization for optimizing the collection efficiency, PBS, and a lens to collimate light into a collection fiber. The output fiber is then coupled to a spectrometer (Oxford Instruments).

The sample is glued to a printed circuit board (PCB) and mounted in the flow cryostat chamber (Microstat HireS II, Oxford Instruments). Thermal contact to the sample is established via a copper cold-finger. A voltage source (Keithley 2450) is used to apply an electric field on the sample. The transfer tube illustrated on the right side of the sample in Fig. 3.1, is used to deliver liquid helium to a heat exchanger close to the

sample mount. The helium returning from the heat exchanger then cools the radiation shield and flows out of the cryostat. A thermometer and heater are mounted on the heat exchanger. These can be used together with a temperature controller to balance the cryostat's cooling power and control the temperature of the sample.

Measurements are usually done at 10K, which is cold enough for most of the basic QD characterization. In addition, the amount of helium needed to maintain a 4K temperature is far more than what is required to keep it at 10K. The characterization of single-photon sources has stringent requirements regarding setup stability, especially for the polarization filtering of the laser background resonant excitation. The continuous flow of helium causes vibration and can lead to stage drift. Moreover, owing to the price of the liquid helium and the considerable amount of helium needed to maintain the cryostat cold, we need to warm up and cool down the sample every day, which can potentially damage the sample. The emission frequency and relative excitation position of QDs change from one cool down to another, adding too much effort for characterization. Therefore, for advanced SPS characterization, a dedicated closed-cycle cryostat system is used.

3.1.2 Attocube closed-cycle cryostat

After a pre-characterization of the newly fabricated samples, the promising candidates are transferred to an attoDry 2100 closed-cycle cryostat for accurate characterization. Apart from having a more stable and colder (1.6K) chamber, the cryostat features lower environment noise. An optimized and robust characterization setup has been built and it is shown in Fig. 3.2 for SPS characterization.

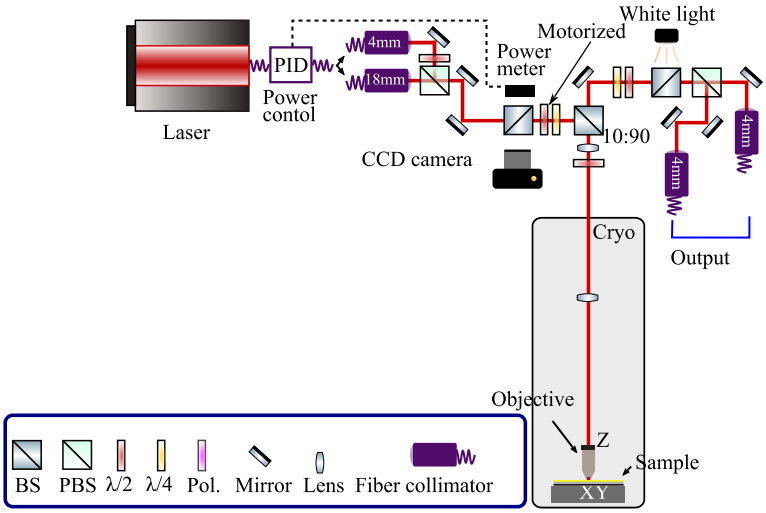

Figure 3.2: Schematical layout the attoDry 2100 cryostat and its characterization setup. Courtesy of Freja T. Pedersen.

Compared to the flow cryostat, where all the components are mounted on an optical table to fit the cryostat configuration, here a 50×50 cm^2 portable optical breadboard integrates the excitation and collection optics in a small space. The input laser, controlled via a PID setup, can be coupled to one of the two input fiber couplers that collimate the beam to different spot size. One coupler is for fitting the back focal plane of the objective aiming to achieve a diffraction-limited beam spot on the sample surface, while the other one is used for mode matching to shallow etched gratings used to couple the light in the sample. Then the two inputs are combined in a PBS to maximize the throughput of both.

The excitation beam is sent through a 50:50 BS, where the reflected port is aligned to a PM to monitor and stabilize the input power. A CCD camera is aligned on the other side of the same BS for imaging. A set of motorized half-wave plate and quarter-wave plate are used for precisely controlling the input beam polarization. This enables to populate a typical QD exciton dipole or match grating coupler orientation. A 10:90 (R:T) BS is used to guide the excitation laser to the cryostat. Since the BS is polarization and wavelength sensitive, we performed a calibration scan of the incident polarization using motorized waveplates and PID power control for correction at the specific wavelength. The excitation beam goes through a low-temperature confocal microscope objective which focuses it onto a spot on the sample surface.

The microscope is a $4f$ imaging system with focal length $f = 2.39$ mm and numerical aperture $NA_{\text{obj}} = 0.81$. The light emitted from the sample is sent to the output path through the same microscope used for focusing the excitation beam. Another set of half-wave plates and quarter-wave plates are used to manipulate the polarization in the output path, introduced after the 10:90 BS. The emitted light goes through a 50:50 BS and PBS. The reflection port of the 50:50 BS is aligned to a white light source on a flip mount with a diffusion lens to illuminate the sample. This configuration is applicable because it allows white light imaging and laser output alignment simultaneously and removing the white light when carrying out experiments. The PBS allows collecting from two orthogonally-polarized device gratings simultaneously.

The cryostat consists of a central unit, a support unit, a helium gas storage vessel, a scroll pump, and a compressor. The support unit contains the control electronics, the pulse tube valve, and the pulse tube cooler buffer reservoirs. Fig. 3.3 sketches the side view of the central unit, and the sample space is cooled by continuous gas flow in a variable temperature insert (VTI), which allows controlling the temperature on the sample position typically from 1.5K to 300K. An exchange gas should be applied between the sample and VTI space for thermal contact. In the figure, I and II indicate the connection to the cooling gas system, which contains a pulse tube, a gas storage vessel, a dry sealed scroll pump, and a condense line.

When the cold head of pulse tube reaches its base temperature, helium gas is pumped from the storage vessel into the condense line. The condense line is composed of a cold trap at the 1^{st} cold stage of the pulse tube and the 2^{nd} cold stage. Below the second cold stage 4K, the condense line is connected to a small reservoir that plays a role as a buffer for liquid helium. Helium gas passes the cold trap, cools down, condenses, and accumulated in a liquid helium reservoir eventually. Under the action of gravity,

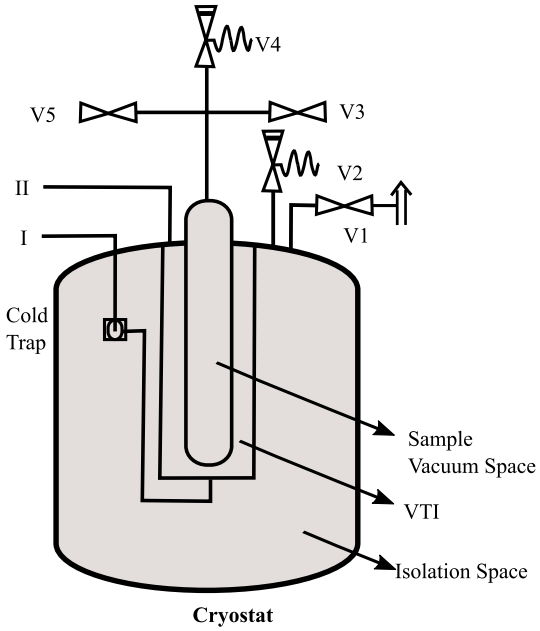

Figure 3.3: Side view of the main unit of the attoDry 2100 cryostat. I and II is the connection point ports to the gas-handling system. A set of valves on the top of the mainbody are employed for control over the pressure inside.

liquid helium flows to VTI, evaporates, and cools down the VTI below 4K. Pumping helium gas back to the condensing line through the sealed scroll pump thus provides a closed-circle operation of the system and a stable base temperature below 2K at the sample position.

The sample is mounted on a PCB as described in section 3.1.1 and placed on top of three XYZ nano-positioner stages. A low-noise and high-resolution voltage source made by Physics Basel is used here instead of a Keithley source meter. The output has a 24-bit resolution, which allows adjusting the voltages with a step size of only 1.2 μV . The output voltage noise is below 1 μV RMS, measured in a frequency range of 0.1 Hz to 100 Hz.

3.1.3 Excitation laser

In this work, we employed two type of lasers for QD excitation, a continuous wave (CW) diode laser, and a pulsed laser, to characterize QDs. The CW laser has a continuous mode-hop-free tuning bandwidth > 50 nm centered at 940 nm and can be frequency-locked using a wavemeter. It is used to perform resonant transmission (RT). The QD resonant frequency and linewidth can be determined with high accuracy by RT, and then, accordingly, resonant fluoresce (RF) can be performed. However, the emission

time of the photons can not be controlled under CW excitation, which undermines the indistinguishability of single photons. Pulsed excitation is therefore required for RF. Here, an exciton is created by the laser pulse, which decays to the ground state by emitting a photon. Ideally, a single photon is emitted at each pulse excitation.

The pulse laser has a transform-limited frequency bandwidth of ≈ 100 GHz. The QDs transitions that we addressed are much narrower. Therefore the pulsed laser can excite other unwanted transitions on high QD density samples. In addition to that, the signal-to-noise ratio is also relevant to the bandwidth of the pulse. Therefore, using a proper laser pulse bandwidth can benefit QDs excitation. Here we employed a volume Bragg grating (VBG) as a narrow frequency filter with a ~ 18 GHz bandwidth to reduce the pulse bandwidth.

3.1.4 Filtering setup

To measure the indistinguishability of the emitted photons, it is crucial to suppress the spectral contributions which do not come from the QD transition. Generally these unwanted contributions arise from the laser background, a second dipole emission, or from the phonon sideband. A filtering setup is employed to cut off part of these unwanted spectral contributions taking advantage of the bandwidth mismatch between the emitted photons and these unwanted contributions as illustrated in Fig. 3.4.

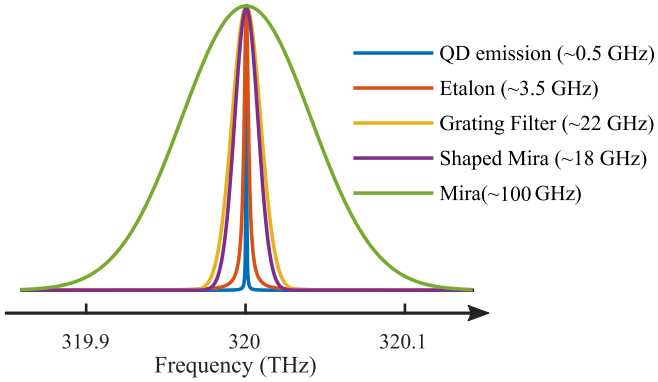

Figure 3.4: Sketch of the bandwidth of different systems involved in QD spectroscopy.

Grating filters and etalons are employed in this project, which can efficiently filter the unwanted frequencies, thereby enhancing indistinguishability. The standard grating filter works in the following way, the different frequency components of the 100 GHz broad laser pulse are dispersed using a grating and reflected off the grating at slightly different angles leading to spatial separation. Fig. 3.5 a) sketches the grating setup employed in our characterization system. The laser goes through a polarization paddle and then into a beam expander comprising a pair of lenses before it is sent to the grating. The expanded beam size should roughly match the grating area, and the larger

the beam diameter, the higher resolution between different frequency components. A large focus lens is introduced to focus the dispersed beam down to a spot with diffraction-limited size. Finally, the rejection of the unwanted frequency components is realized when the collimated beam is coupled into a $NA_{fiber} = 0.13$ fiber. For the grating filter, the experimentally measured efficiency is ~ 65 % limited by grating diffraction efficiency. Moreover the quantum dots emission linewidth we addressed is around 500 MHz, and the bandwidth of the grating filter is measured ~ 22 GHz shown in Fig. 3.4, indicating that the grating filter can not efficiently filter unwanted spectra.

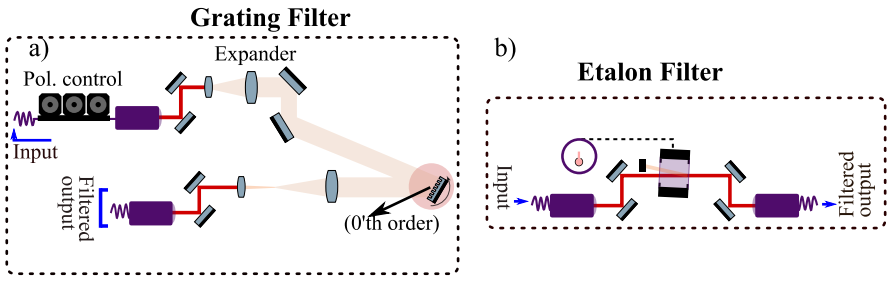

Figure 3.5: Sketch of the filtering setups for SPS characterization. a) The grating filter setup, b) The etalon filter setup. Courtesy of Freja T. Pedersen.

Etalon filters are widely used for filtering QD emissions. Fig. 3.5 b) sketches the etalon setup. It is a temperature-tunable Fabry-Perot filter made of Silica. The etalon is oriented with an angle to adjust the spatial separation of the reflection and transmission. The setup has an experimentally measured efficiency of around 85 %, which is limited by the reflectivity at the end faces and losses in Silica. Compared to the grating filters, etalon offers higher efficiency and smaller bandwidth (3.5 GHz), which is closer to the linewidth of the QDs emission we addressed, and thus can filter the phonon sideband efficiently.

3.1.5 Setup efficiency

The setup efficiency consists of the collection path efficiency and the detection efficiency. In this work, the SPS efficiency is defined as the in-fiber efficiency. So the efficiency of detectors is used to calibrate the efficiency and allow us to compare the SPS efficiency across different setups.

Collection path efficiency

As shown in Fig. 3.2, the collection path contains several free-space optical elements, including an objective, two lenses, the optical window of the cryostat, a beam splitter, two waveplates, a polarization beam splitter, and two mirrors. Each of these components introduces loss. To estimate the collection losses, a CTL at a wavelength of 947 nm has been shone free-space through each of these optical components to measure the

transmission efficiency. The result is listed in table 3.1.5. The mirrors, waveplates, and polarizers show very similar efficiency with variations lower than one percent. Therefore, these components are listed together for simplicity. The loss of lenses and entrance window is too small to be measured accurately and is therefore neglected here. Single optical component refers collectively to mirrors, waveplates, and polarizers. The total collection path efficiency is

$$\eta_{\text{collect-path}} = \eta_{\text{obj}}\eta_{\text{opt}}\eta_{\text{BS}}\eta_{\text{opt}}{}^{4}\eta_{\text{PBS}}\eta_{\text{fiber}} = (41 \pm 3)\% \tag{3.1}$$

Single optical component	η_{opt}	98±1%
Objective	η_{obj}	82±0.2
Beam Splitter	η_{BS}	95±2
Polarization Beam Splitter	η_{PBS}	98±0.5
Fiber Connector	η_{fiber}	59±2

Table 3.1.5 generalizes the efficiencies of every single element employed in the collection path of Fig. 3.1.2.

Detector efficiency

All the detectors used in this thesis and the corresponding typical performance values are listed in table 3.1.5. The resolution refers to the time jitter of the detectors. The standard fiber-coupled avalanche photo-diodes (APD) provide low efficiency but it is well calibrated, thus it allows to precisely estimate the photon counts and calibrate the setup efficiency. The time resolution of APD is 450 ps, which limits some measurements such as the decay of fast QDs. For faster detection, superconducting nanowire single-photon detectors (SNSPD) are used, which offer a better timing resolution, higher efficiency and more importantly very few dark counts. In this project two kinds of SNSPD are employed: a general one (SNSPD) and a super fast one (Fast SNSPD). The Fast SNSPD are typically employed for QDs with decay dynamics in the 50 ps range, which require higher timing resolution detection system. In this case, only the Fast SNSPD with optimized timing resolution can be used to perform the measurements.

Detector	Efficiency at 940 nm	Resolution (FWHM)	dark cts.
APD	30%	450 ps	$\sim 100Hz$
SNSPD	70%	200 ps	$< 5Hz$
Fast SNSPD	$\sim 50\%$	15 ps	$< 10Hz$

3.2 Quantum dot excitation schemes

As discussed in chapter 1 Fig. 1.5, the investigated QDs are self-assembled In(Ga)As. Excitons in QDs can be formed by thermal, electrical, or optical excitation. In this work, we utilize optical excitation methods since it provides, to date, the highest degree of control and emission quality.

The three-dimensional confinement in QDs produces discrete energy levels for electrons and holes. Therefore, just like atoms, QDs only emit one photon at a time. To emit photons, an electron from one of the confined energy levels (or electronic shell) in the conduction band recombines with a hole from the valance band according to optical selection rules. Depending on the energy at which excitons are created, one can devise three corresponding optical excitation schemes, i.e., above-band excitation, quasi-resonant excitation, and resonant fluorescence (RF).

3.2.1 Above-band excitation

Above-band excitation is the quickest method to measure the spectral distribution of a QD sample. Fig. 3.6 a) sketches the process of how to create excitons with above-band excitation. The excitation laser has higher energy than the bandgap of the GaAs. Thus the electrons generated in the conduction band and the holes generated in the valance band undergo relaxation simultaneously, and some of them are captured by the QDs and then relax to the lowest unoccupied QD energy through phonon interaction around a time scale of tens of ps. Due to the uniformity of QDs size in self-assembled QDs and the different excitonic states, many transitions are possible, all with different frequencies.

Figure 3.6 b) shows the spectrum of the QDs under above-band excitation, which provides an estimate of the QDs density by looking at the emission lines per beam spot area and spectrum range. The relaxation time spent from the generation of electrons and holes to the creation of the exciton is typically much shorter than the decay time of the exciton. The energy difference between the excitation light and the emitted photons allows us to filter the laser background spectrally and thus only get the single photon emission in the spectrum. However, the relaxation process leads to larger dephasing, which deteriorates indistinguishability. Moreover, above-band excitation can not selectively excite specific QD in a relatively high QD density area. So the above-band excitation can not be employed to generate high indistinguishability photons.

3.2.2 Quasi-resonant excitation

Compared to the above-band excitation, in the quasi-resonant excitation (or sometimes called p-shell excitation) method, shown in Fig. 3.6 c), excitons are formed directly in the QD. The laser light directly populates the electron in a higher QD electronic shell of the conduction band and then decays to lower shells and recombines to emit photons. This process suppresses phonon interactions and dramatically reduces the relaxation time, providing a cleaner spectrum. The spectrum of the p-shell excitation shown in Fig. 3.6 d) only has one prominent photon emission. We can get near-unity purity single photons by p-shell excitation as spectral filtering can be employed, and thereby, less background from other transitions is present. However, the short time relaxation can still cause non-trivial dephasing, which affects indistinguishability.

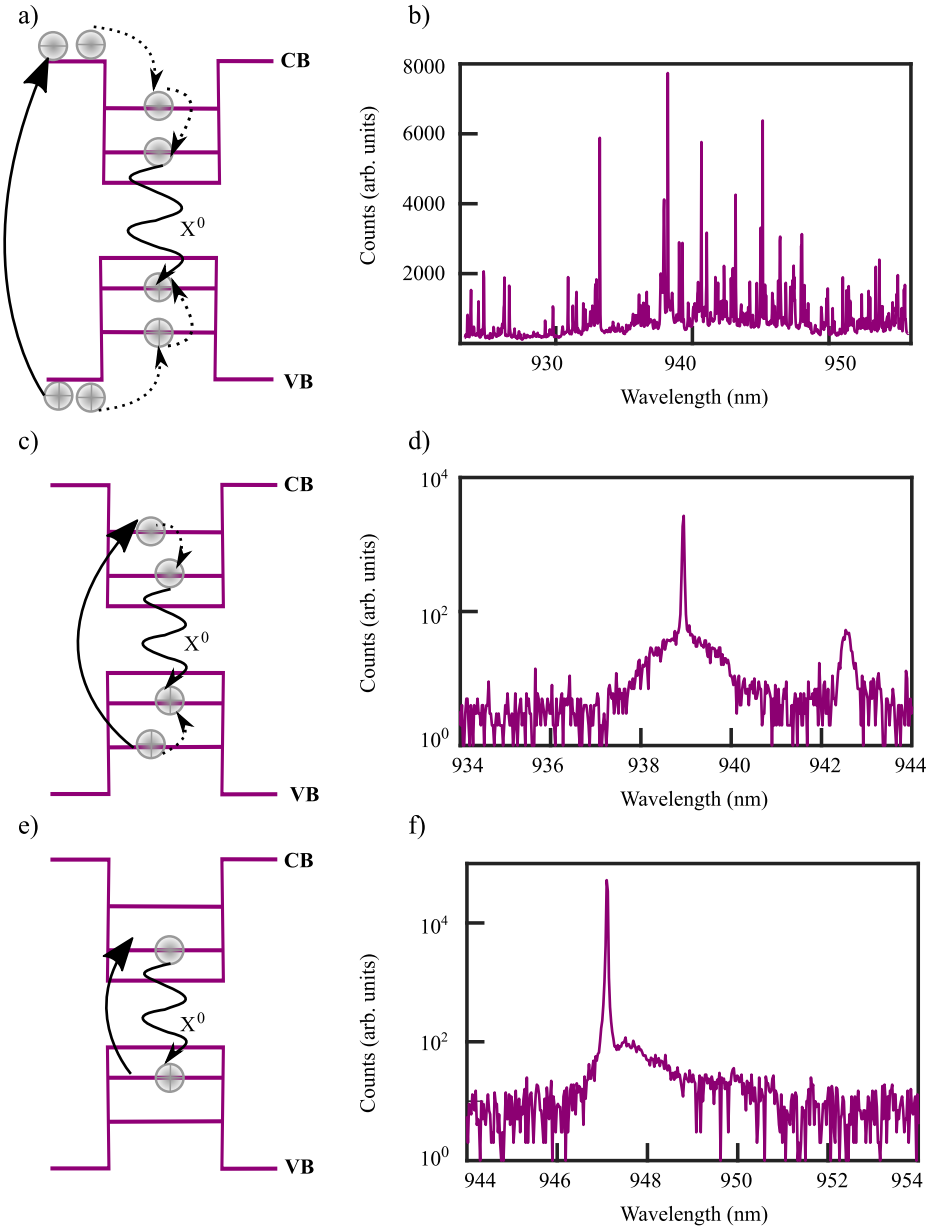

Figure 3.6: Quantum dot excitation schemes. Schematic of the process for creating excitons in QDs by a) above-band excitation, b) p-shell excitation, c) resonant excitation. The corresponding spectra are shown in b), d), f), measured on QDs in a photonic crystal waveguide.

3.2.3 Resonance fluorescence

To generate highly indistinguishable single photons, a resonant excitation scheme must be employed. Fig. 3.6 e) shows that the s-shell is driven directly with a resonant laser which completely eliminates the time jitter. In this case, the residual dephasing is due to the phonon-induced emission from the lattice vibration, which can be significantly suppressed below 4K and filtered using the etalon. Additionally, applying an electric field to the QDs suppresses charge noise in the vicinity of the QDs, thereby considerably reducing any spectral diffusion.

The challenging aspect in RF is that the laser background, which has the same frequency as the single photons, is much harder to suppress efficiently. In this thesis, a cross-polarized configuration is employed to extinguish the excitation laser (the laser and the collected light are cross-polarized from each other and spatially separated in the chip). Using this method, a clean RF spectrum shown in Fig. 3.6 f), is observed. The QD emission line (zero phonon line) and its phonon sideband are observed without an etalon filter.

* * *

In this chapter, we introduced the two main cryogenic optical setups used for the single-photon source characterization. The apparatus and the relevant elements comprising the optical setups have been described in detail. Moreover, three standard excitation schemes for QDs (above-band excitation, p-shell, and resonance fluorescence) have been discussed. The experimental results are discussed in Chapter 4 and 5.

CHAPTER 4

Characterization of Single-Photon Sources

Overview of the fundamental properties required for a single photon source, and characterization of high quality single photon sources from planar nanostructures.

The recent advances in photonic quantum technologies are strongly linked to the availability of near-ideal single-photon sources (SPSs). Quantum dot (QD) based SPS have progressed tremendously in recent years, and are expected to play a key technological role in the development of future quantum information devices. What defines a good single-photon source? And how can we improve them further? This chapter outlines the most important requirements and specifications that a modern solid-state SPS should meet and review the state-of-the-art in the field. By applying the fabrication techniques outlined in Chapter 2, the generation of high quality single photons in planar nanostructures is demonstrated.

4.1 Requirements for single-photon sources

An ideal SPS should *deterministically* and *efficiently* delivery only *one photon at a time* in a well-defined polarization and spatial-temporal mode, and each of the single photons must be completely identical. The following three essential properties are commonly used to assess the quality of an SPS: purity, indistinguishability, and brightness. Fig. 4.1 schematically depicts how an ideal source differs from actual sources: a sequence of input optical pulses should ideally trigger the emission of a train of perfectly indistinguishable single photons. In a real-life scenario, some photons are lost, or are

distinguishable, or mix with other photons (from other QDs or from laser background).

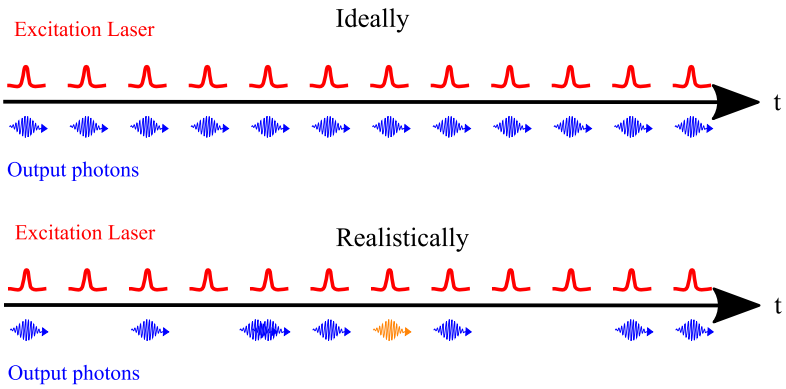

Figure 4.1: Illustration of an ideal deterministic single-photon source (above) versus reality (below). Realistically, some output single photons are lost on the way, as illustrated with missing photons. Further, two photons events can exist, and finally, some photons could be non-ideal and distinguishable from the others, presented with the orange photon.

4.1.1 Purity

A single-photon source is considered pure if every photon is emitted exactly one at a time. If this is the case, every photon impinging on a 50/50 beam-splitter would either be detected at one output port or the other, but never simultaneously. This experiment, known as the Hanbury Brown and Twiss experiment1.2.3, provides a measurement of the second-order intensity correlation function $g^{(2)}(\tau)$ given in Chapter 1.2.3 equation 1.29. The function gives the joint probability of detecting one photon at time t and $t+\tau$, only depends on the time-difference τ. At $\tau = 0$ a pure single-photon source should have $g^{(2)} = 0$. A photon wavepacket is expressed as [72]

$$|\Psi\rangle = \sum_{\mathrm{k},\epsilon,\mathrm{c}} c_{\mathrm{k},\epsilon} \, |n\rangle_{\mathrm{k},\epsilon} \,, \tag{4.1}$$

where $|n\rangle_{\mathrm{k},\epsilon}$ denotes a number state or Fock state having exactly n ($n = \langle \hat{\alpha}^\dagger \hat{\alpha} \rangle$) photons. Each mode is a quantized harmonic oscillator with spatial frequency k, defined polarization ϵ. $g^{(2)}(\tau = 0)$ for the Fock state is $1 - \frac{1}{n}$. Therefore $g^{(2)}(0) = 0$ only for the superposition of single-photon state and vacuum state, while higher values are expected for multi-photon states. For instance, coherent states have $g^{(2)}(0) = 1$, and thermal states have $g^{(2)}(0) = 2$. The value of $g^{(2)}(0)$ is therefore used to characterize the purity of the SPS as it is inversely proportional to the probability of having two- or higher photon states. A highly-pure single photon source is key to photonic quantum technologies. For example, it increases the security of quantum communication

[73] (protection against beam splitter attacks) and minimizes errors in quantum and simulation and computation [74].

4.1.2 Indistinguishability

One of the most challenging aspects of photonic quantum information processing is to achieve photon-photon interactions to implement multi-photon gates. Linear optical quantum computing relies on quantum inference between two indistinguishable photons. The indistinguishability indicates how identical the photons in a stream are compared to each other in terms of frequency, temporal shape, and polarization. It can be characterized by means of photon wavepacket overlap, which is measured through Hong-Ou-Mandel (HOM) interference [75]. The experimental characterization of indistinguishability is discussed in section 4.2.3.

4.1.3 Brightness

Brightness refers to the overall efficiency of the SPS, which includes the generation efficiency (i.e., what fraction of input pulses is effectively converted in single photons by the QD) and collection efficiency (i.e., what fraction of the emitted photons are delivered to the optical mode of interest, whether it is a fiber, a waveguide, or the inputs of a photonic integrated circuit). A deterministic SPS should deliver single photons without vacuum components. However, it very challenging to avoid an optical loss to the vacuum component. In the SPS community, there is no unified way to define collection efficiency. Two main definitions are found in the literature, count rates on the detector, or number of photons per second on first lens, which makes the comparison of brightness from different sources not straightforward.

The lower efficiency of an SPS source, the poorer of scaling the system. In fact, when scaling to N single photons with efficiency η, the overall system efficiency drops proportionally with η^N. Because of this, the low efficiency of SPS is one of the main roadblocks to developing scalable quantum photonic technologies. QD-based sources offer near-unity generation efficiency as they can be operated on-demand, so the true challenge lies in the fabrication of ultra-low loss waveguides and devices to improve the collection and boost the photon counts at the detector.

4.2 Experiments for meeting the above requirements

4.2.1 Purity measurement

For a SPS generated from an ideal two-level system, the exciton radiative decay time is on the order of the Rabi frequency, thus it is impossible to re-excite the emitter before it decays to ground state. Naturally, there is no chance to observe concurrent emission events at the same time for such a two-level system. This is the phenomenon known as anti-bunching with the observation of $g^{(2)}(\tau = 0) = 0$. Fig. 4.2 a) sketches the Hanbury Brown and Twiss (HBT) [76] setup used to measure the SPS purity. Single photons emitted from a QD are sent to a 50:50 BS and detected at two outputs. The detectors

outputs are connected to correlation electronics that measure the time delay between coincidence detection events, that is, events where both detectors click.

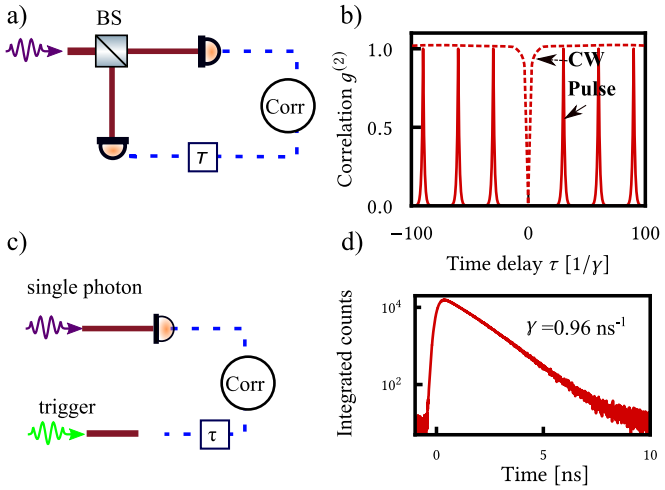

Figure 4.2: a) Sketch of the setup to perform Hanbury Brown and Twiss (HBT) experiment. c) To perform radiative decay rate measurement. b) Correlation histogram from HBT measurement for an ideal SPS under pulsed laser excitation (solid line) and continuous wave excitation (dashed line). d) Decay rate curve for the QD in the bulk GaAs membrane.

To describe the HBT experiment more in detail, we highlight the quantum mechanical description of the beam splitter (cf. Fig. 4.3 a)). The figure illustrates the four modes at the input and output of a BS with generic transmittances t, t' and reflectances r, r'. For a dielectric 50/50 BS the transformation matrix given by [77]

$$\begin{pmatrix} \hat{a}_2 \\ \hat{a}_3 \end{pmatrix} = \frac{1}{\sqrt{2}} \begin{pmatrix} 1 & i \\ i & 1 \end{pmatrix} \begin{pmatrix} \hat{a}_0 \\ \hat{a}_1 \end{pmatrix}, \tag{4.2}$$

where $\hat{a}_0$ and $\hat{a}_1$ are the input modes and $\hat{a}_2$ and $\hat{a}_3$ are the output modes. The complex coefficient in the transformation matrix indicates that a $\pi/2$ phase difference is typically obtained between the transmitted and reflected beams. The output modes result in a superposition of the two input modes. $\hat{a}_0^\dagger$ and $\hat{a}_1^\dagger$ denote the creation operator of input fields, while $\hat{a}_2^\dagger$ and $\hat{a}_3^\dagger$ are the creation operators of output fields.

In the Schrödinger picture, any input state is transformed to an output by the BS given

$$|\Psi_{\text{in}}\rangle \xrightarrow{BS} |\Psi_{\text{out}}\rangle\,. \tag{4.3}$$

A single photon impinging on mode $\hat{a}_1$ can be written as

$$|\Psi_{\text{in}}\rangle = \hat{a}_1^\dagger\,|0\rangle_0\,|0\rangle_1\,, \tag{4.4}$$

which leads to the output state

$$|\Psi_{\text{out}}\rangle = \frac{1}{\sqrt{2}} \left(i\,|1\rangle_2\,|0\rangle_3 + |0\rangle_2\,|1\rangle_3 \right), \tag{4.5}$$

which indicates that each detector at each output yields a random result, 0 or 1, each has a probability of 50 % at one time.

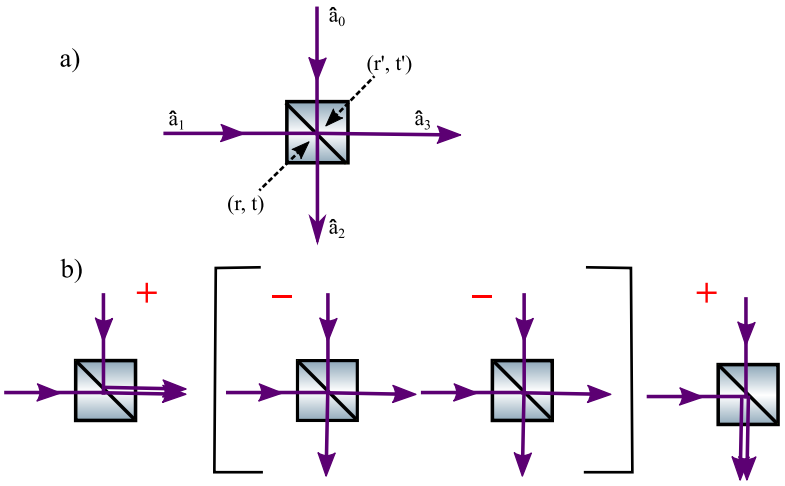

Figure 4.3: a)The quantum-mechanical description of a beam splitter with corresponding quantized optical modes. b) Possible paths taken by two photons interfering in a beam splitter. For perfectly indistinguishable photons, the probability amplitude of the events where both photons are transmitted or reflected cancels out (in the bracket).

Figure 4.2 b) illustrates the ideal $g^{(2)}(\tau)$ histograms in the case of pulsed (solid line) and continuous wave (dashed line) excitation. Under continuous wave (CW) excitation, the excited state is populated continuously, leading to a dip at $\tau = 0$. Experimentally, it is not easy to resolve the dip as the signal is convoluted with the response function of the detectors. A more precise measurement can be achieved under pulsed excitation, where a single photon is generated on every pulse. Correlation peaks show up at times corresponding to the laser repetition rate, and decays exponentially on two side with a rate corresponding to the QD radiative decay rate. At $\tau = 0$, the central peak is suppressed, indicating that the photons are anti-bunched. The purity $g^{(2)}(0)$ is defined as the ratio of central peak area $A(0)$ over the neighboring peak area A ($g^{(2)}(0) = \frac{A(0)}{A}$).

4.2.2 Lifetime measurement

Chapter 1.2.3 presents another important characterisatic of a two-level system, radiative decay rate Γ, indicating how fast of an emitter relaxes from its excited state to its ground state. The measurement of the emitters' Γ is performed using the setup shown in Fig. 4.2 c), where the photon emitted from the QD is sent to the detector and registered in

the counter with a trggered pulse. The corresponding correlation histogram, shown in Fig. 4.2 d), measures the average time of arrival of photons from the time when the pulse has been emitted. The curve shows a typical exponential decay due to spontaneous emission. In our system, the lifetime of self-assembled QDs is typically ~ 1 ns, while the pulse width used to excite QDs is about tens of ps, in this way we can avoid double excitation and hence that only one photon is emitted per excitation.

4.2.3 Indistinguishability measurement

As motivated in 4.1.2, the indistinguishability is crucial for quantum applications and it is measured by the Hong, Ou, and Mandel (HOM) experiment [78]. In the HOM configuration, the incident state is now

$$|\Psi_{\text{in}}\rangle = |1\rangle_0 |1\rangle_1 = \hat{a}_0^\dagger \hat{a}_1^\dagger |0\rangle_0 |0\rangle_1 \tag{4.6}$$

When interfering at the beam splitter, the output state will be

$$|\Psi_{\text{out}}\rangle = \frac{i}{\sqrt{2}} (|2\rangle_2 |0\rangle_3 + |0\rangle_2 |2\rangle_3) \tag{4.7}$$

indicating that the two photons will always emerge together such that the two detectors will never register simultaneous counts. The reason for this outcome we can be understood intuitively from Fig. 4.3 b) illustrating the four different events for the two photon interference. The events where both photons are transmitted and reflected have an amplitude that destructively interferes leading to zero probability of the outcome that we have a photon in each detector. The absence of $|1\rangle_2 |1\rangle_3$ component indicate these two events process are indistinguishable. On the other hand, for distinguishable photons, simultaneous clicks at the detectors are possible. The layout of the HOM setup used in this thesis to carry out the measurement is shown in Fig. 4.4 a), the emitted single photons are interfered in a Mach-Zehnder interferometer. Firstly, the single photons go through a rotatable half-wave plate before entering a 50:50 BS, splitting the signal into two arms. This configuration allows tuning the splitting ratio accurately so that the signal intensity of the two arms is equal. A delay fiber in the lower arm is employed to produce a time delay of τ_{rep} with respect to the upper arm. The delay time τ_{rep} corresponds to the repetition rate of the excitation laser. When the first emitted photon is reflected and travels along the lower arm, and the following emitted photon is transmitted and travels along the upper arm, the two photons will arrive at the FBS simultaneously.

The rotating half-wave plate in the upper arm is introduced to change the polarization of the photons with respect to the polarization of the photon entering into the lower arm. It allows to map out the interference visibility fringes as a function of the waveplate angle, thereby accurately measuring the interferometer visibility in co-polarization and cross-polarization. A polarization paddle is used to ensure the co-polarization at the FBS to achieve maximum interference. After interference on the FBS, the signal is sent into detectors and time correlated in the same manner as the

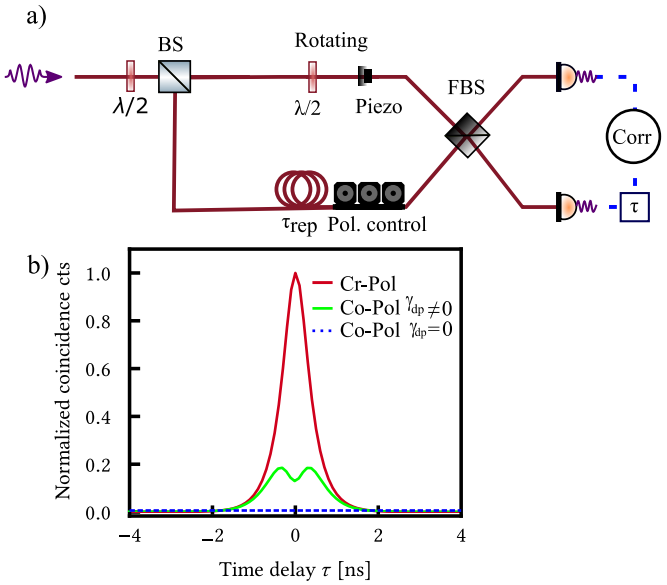

Figure 4.4: HOM visibility measurement. a) Sketches of the HOM interferometer. Single photons are split by a 50:50 beam splitter (BS), guided into two arms, and subsequently interfered in a fiber beam splitter(FBS). The half-wave plate placed before the BS is used to balance the photon counts at the two arms. The half-wave plate (called rotating waveplate) in the upper arm allows swapping between co-and cross-polarized configurations. b) The corresponding correlation histograms for different configurations. The red curve corresponds to the cross-polarized configuration that the two photons are orthogonally polarized. Thus, they are distinguishable. The blue curve and green curve gives the co-polarization configuration of completely indistinguishable single photons ($\gamma_{\mathrm{dp}} = 0$) and partially indistinguishable single photons due to pure dephasing γ_{dp}, respectively.

HBT measurement. If one detector measures a photon at time t and the other detector detect another at time $t+\tau$, they create a coincident event. For the time delay $\tau = 0$, the probability of detecting coincident events is zero indicating the photons are completely indistinguishable. Vice versa, if the two photons are distinguishable, they can exit the beam splitter through different ports, and zero-time delay coincidences can be detected.

By applying the quantum regression theorem and solving optical Bloch equations discussed 1.2.3 equation 1.30, allowing deriving an expression for the HOM correlation [79] as a function of the emitter lifetime Γ and pure dephasing rate Γ_{dp}

$$G^{(2)}(\tau) = \frac{1}{4\Gamma} e^{-\Gamma|\tau|}(1 - e^{-2\Gamma_{\mathrm{dp}}|\tau|}). \tag{4.8}$$

In the co-polarization configuration, if the two incoming photons interfering on the FBS are perfectly identical ($\Gamma_{\mathrm{dp}} = 0$), the correlation histogram in the form of Fig. 4.4 b) (dashed blue line). In an experimental case, i.e.,$\Gamma_{\mathrm{dp}} \sim 0.15\Gamma$, a visible pure dephasing dip is shown in Fig. 4.4 b) with green solid line. In the cross-polarization configuration, the two incident photons are fully distinguishable, corresponding to the solid red curve

in Fig. 4.4 b). The indistinguishability is quantified by the visibility in this configuration as measured *raw* HOM visibility given

$$V_{\text{raw}} = \frac{A_{\perp} - A_{\parallel}}{A_{\perp}}, \tag{4.9}$$

where $A_{\perp}$ and $A_{\parallel}$ are the area under central peaks at $\tau = 0$ for co-polarization and cross-polarization, respectively. In terms of pure dephasing rate, the V_{raw} can be expressed as [79]

$$V_{\text{raw}} = \frac{\gamma}{\gamma + 2\gamma_{\text{dp}}}. \tag{4.10}$$

Before each measurement, the HOM setup is calibrated by adjusting the polarization difference and the signal intensity of the two arms. This is done by sending a CW laser through the setup, while one of the output ports from the FBS is sent to an oscilloscope. A piezoelectric mirror is introduced (cf. Fig. 4.4) to modulate the path length in a controlled way. The oscilloscope displays the intensity of classical interference fringes of the setup by adjusting the fiber paddles precisely. Thus the polarization overlap of the two arms is maximized. By setting the oscilloscope to DC mode, we can modulate the signal intensity at the two arms and balance the splitting ratio by tuning the half-wave plate placed before the first BS. As the interferometer is very sensitive to polarization drifts, we stabilize all the fiber elements properly and tape them to the optical table, ensuring mechanical stability. Thus we can perform robust measurement without introducing any phase shift.

The visibility V_{raw} obtained from the HOM measurement is limited by imperfections of the interferometer and by single photons purity. The imperfection of the interferometer stems from non-perfect 50:50 splitting ratio and from unbalanced arms, producing a limited contrast of the classical interference visibility $(1 - \epsilon)$. Moreover, if the SPS purity $g^{(2)}(0)$ is not zero, typically due to scattering from the excitation laser background, the HOM visibility is further reduced. Imperfections will affect the coincidences of the central peak in the following way [80]

$$A(V) = \left(R^3T + RT^3\right)\left[1 + 2g^{(0)}(0)\right] - 2(1-\epsilon)^2R^2T^2V, \tag{4.11}$$

where R and T are the reflectivity and transmission of the BS and V is the intrinsic visibility of the source. For an ideal source of indistinguishable single photons, this allows us to write the ideal source visibility base on equation 4.9 as

$$V_{\text{ideal}} = \frac{2RT\,(1-\epsilon)^2}{(R^2+T^2)\left[1 + 2g^{(0)}(0)\right]} \tag{4.12}$$

The ideal visibility is utilized to normalize, and correct the measured raw visibility, thus we can derive the expression for the intrinsic visibility

$$V = \frac{V_{\text{raw}}}{V_{\text{ideal}}} = \frac{(R^2+T^2)\left[1 + 2g^{(0)}(0)\right]}{2RT\,(1-\epsilon)^2}V_{\text{raw}} \tag{4.13}$$

The intrinsic visibility allows to compare the indistinguishability across different HOM experiment setups.

In this thesis, all the HOM visibity measurements were carried out in the same setup, the parameters and corresponding methods are implemented to correct raw HOM visibility as shown in table 4.2.3, where CTL denotes the continuously tunable laser. The correction column indicates how much of the corresponding parameters contributed to the corrected visibility value.

Parameter	Value	Correction	Measurement Method
R	0.476	0.5 %	Resonant transmission with CTL
T	0.524	0.5 %	Resonant transmission with CTL
(1-ϵ)	0.998	0.4 %	Fringe contrast measurement with CTL

Table 4.2.3 lists the parameters for HOM visibility correction.

4.3 Single photon source efficiency

In section 4.1.3, we discussed how challenging it is to achieve highly efficient SPS for quantum information. To characterize the efficiency, all the losses that single photons experience along the propagation path should be carefully measured. In Chapter 3, we performed a detailed analysis of losses in the Attocube closed-cycle cryostat section 3.1.2, which collectively introduces (41±3) % loss including fiber. In the following, we discuss the single-photon generation efficiency and derive the total efficiency and brightness of our source. The whole characterization has been carried out using the continuous-wavelength laser (CTL) operating at 947 nm, i.e. close to the QD emission wavelength.

4.3.1 Single-photon generation efficiency

The single-photon generation efficiency consists of the QD source efficiency and the chip to fiber efficiency.

QDs source efficiency

The intrinsic efficiency of the QD source is determined by the single photon coupling efficiency, residual minor coupling to other states and the phonon decoherence. We operated the QDs at a specific gate voltage to populate a neutral exciton X^0. X^0 has two bright states corresponding to dipoles with orthogonal linear polarizations due to the fine structure splitting. The QD location in photonic crystal waveguide (PCW) determines the coupling efficiency of the dipoles, given by β factor introduced in chapter 1.2.4.

The dipole that couples best to the fundamental PCW mode can be selectively excited by optimizing the excitation laser polarization. However, complex scattering of the excitation beam due to the nanostructure, it can result in imperfect extinction, which deteriorates the purity. Therefore, the excitation polarization is optimized to achieve

the maximum ratio of the single photons emission intensity over the excitation laser background. This leads unavoidably to simultaneous excitation of two dipoles. We label the preferred dipole excitation probability as η_Y (Y represents the polarization axis of the electric field mode in the PCW). The radiative decay probability for an exciton is $\eta_{rad} < 1$ due to the blinking induced by the dark exciton (cf. section 1.2.3). The phonon

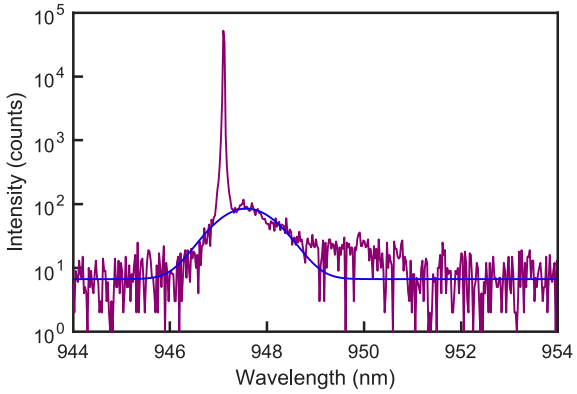

Figure 4.5: The emission spectra of the QD under resonant fluorescence. The blue curve is the Gaussian fit of the emission in the phonon side band.

sideband has to be filtered for the realization of high indistinguishability. As shown in Fig. 4.5, the fraction of light (η_{zpl}) emitted in the zero phonon line is estimated $\sim 95\%$ by Gaussian model. Thus, the intrinsic QD efficiency is given by

$$\eta_{QDs} = \beta \eta_Y \eta_{rad} \eta_{zpl}. \tag{4.14}$$

Chip-to-fiber coupling efficiency

The emitted photons from the QDs couple into the waveguide and propagate to the shallow etched grating (SEG), which diffracts the photons off-chip in a direction quasi-orthogonal to the chip. Subsequently, photons are collected by the objective and coupled into the output fiber as shown in Fig. 4.6. The designed far-field of the grating scattered mode matches a Gaussian profile with a low numerical aperture of $NA_{seg} \approx 0.21$ and 0.16 along two orthogonal axes [70]. Thus the beam is slightly elliptical. The SEG efficiency (η_{seg}) is defined as the fraction of light diffracted by the SEG out-coupling and measured by the method given in ref [70]. The deviation of the measured η_{seg} in this work compared to the literature is due to fabrication imperfection. In order to maximize the collection, the focal length of the collimation lens should be carefully chosen to match the SEG mode perfectly. In addition, we should also include the propagation loss η_g characterized in Chapter 6, so the total chip to fiber efficiency η_{c_f} can be written as

$$\eta_{c_f} = \eta_g \eta_{seg} \tag{4.15}$$

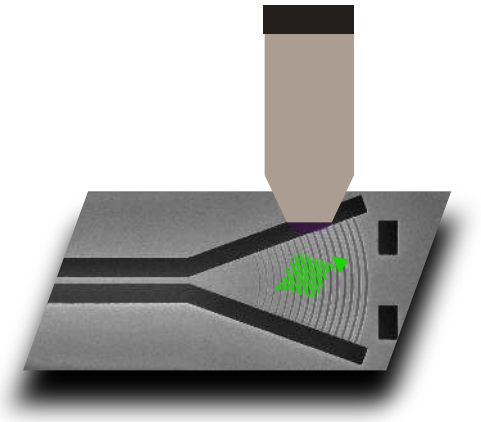

Figure 4.6: Illustration of the photon collection using shallow-etched gratings and an objective.

Total efficiency

We conclude by summarizing the total efficiency of the SPS (see details in table 4.3.1).

$$\eta_{\text{total}} = \eta_{\text{Source}}\eta_{\text{Collection}} \tag{4.16}$$

	component	efficiency
Source	β	$> 90\%$
	η_{Y}	$> 94\%$
	Zero photon line η_{zpl}	$> 95\%$
	Radiative emission η_{rad}	$> 97\%$
	chip to SEG $\eta_{\text{c}_{\text{seg}}}$	40%–60%
	on-chip propagation η_{p}	$> 95\%$
Collection	Directionality	50%–100%
	Collection path $\eta_{\text{collect-path}}$	$(41 \pm 3)\%$
	Etalon filter η_{etalon}	$78\% - 87\%$

Table 4.3.1 gives the details of the elements efficiency relevant to a SPS.

Regarding collection efficiency, which consists of collection path efficiency described in section 3.1.5, Etalon filter efficiency presented insection 3.1.4, and directionality efficiency typically for our specific planar devices described in this article [25].

A comprehensive losses characterization has been done on this setup, which helps us understanding where the losses arise from, and therefore help to improve the maximum collection efficiency. Specifically, in terms of the source efficiency, β in a PCW is a function of lattice constant and radius as well as the QDs spatial position as described in chapter 1. Near-unity β can be routinely achieved in our system.

The chip-to-fiber coupling efficiency η_{c_f} is very sensitive to the fabrication imperfections as discussed in 2.3.2. When the QD emission wavelength matches the central transmission peak of SEGs, η_{c_f} can reach >60 % [70]. Potentially, this value can be boosted to > 80% with the introduction of an additional distributed Bragg reflection (DBR) mirror below the membrane. Additionally, the waveguide propagation efficiency η_p, limited by surface roughness as described in section 2.3.3 and by the Franz-Keldish effect which will be discussed in chapter 6, should be taken into account when waveguides are longer than 100 μm. Waveguide losses exceeding 7 dB/mm, mostly limited by roughness, are routinely observed. However these losses can be neglected for short waveguides.

4.4 Results of single-photon source characterization

In the following, the results from the characterization of a SPS, fabricated with localized gates as described in Chapter 2, are reported. A SPS based on single-side photonic cyrstal waveguides, with ~ 8.47 % total in-fiber efficiency is described. Then two other types of sources based on the same fabrication process, are described: a source based on dual-mode waveguides for in-plane resonant excitation (published in [69]) and a PCW source capable of producing streams of > 100 indistinguishable photons [25].

4.4.1 A bright single-photon source from single-sided photonic crystal waveguide

In order to improve the SPS efficiency due to bi-directional coupling, the two-sided waveguide is modified by terminating one side with a PhC mirror serving as back reflector (see Fig. 4.7 a)). The slow light PCW with length of 5 μm is joined to a fast-light PCW section with equal length. The fast-light PCWs is implemented here for the purpose of reducing impedance mismatch between the slow-light PCW and the nanobeam waveguide and to achieve ≈ 95% transmission efficiency in the device. The lattice constant a and hole radius r of the slow light PCW is 248 nm and 70 nm, respectively. The corresponding cut-off frequency is measured by laser transmission. The CW laser transmission spectrum, shown in Fig. 4.7 b), was measured across a two-side waveguide designed with the same geometric parameters. We assume that the device size fluctuation from one structure to another can be neglected thanks to the highly reproducible nano-lithography. The measured cut-off frequency of the PCW is 316.525 THz (947.18 nm).

Considering the transmission spectrum of shallow etched grating presented in section 2.3.2 and the potential Purcell enhancement, we focus on the QDs spectrally located in the slow light PCW, whose emission wavelength is in the range of (940-947) nm. The QDs density is relatively high in this sample($\approx 10\mu m^{-2}$), for this reason it is not straightforward to perform resonant excitation. We identify three potential QDs in single-sided waveguides by performing p-shell excitation to find the dots physical position. The corresponding emission frequency of the three QDs has been marked with triangles in Fig. 4.7. We notice that the QD1 and QD2 are spatially very close to the interface between the slow light PCW and fast light PCW, but their emission

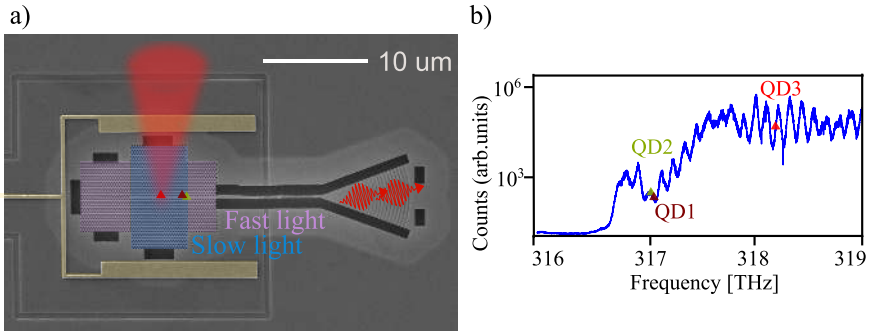

Figure 4.7: A bright SPS is obtained from QDs coupled to single-side photonic crystal waveguide system. a) SEM image of the device used in this measurement, one side is terminated with mirrors serving as a back reflector aiming to double the SPS efficiency. A slow light region is used to find a QD with Purcell enhancement, while the fast light photonic crystal section serves as a mode adapter to the nanobeam waveguide. There are three promising QDs located in the slow light region marked by triangles. b) Laser transmission spectrum of the two side photonic crystal waveguide having identical design parameters in a). The corresponding QDs emission frequencies are also included.

frequencies are close the band-edge which makes them interesting for obtaining a significant Purcell enhancement.

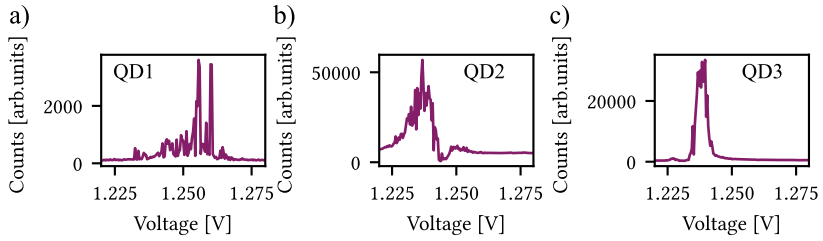

Figure 4.8: Voltage scans of the three QDs located in Fig. 4.7 under cw resonance fluorescence.

We performed CW resonant excitation at a forward bias voltage of 1.24 V. Voltage scans with a step size of 0.4 mV are carried out and shown in Fig. 4.8. The QD3 as expected displays quite smooth spectrum under CW resonant excitation, while the spectra of the QD1 and QD2 are quite noisy. Especially the QD1 displays very pronounced spectrum wandering. This is due to the exciton coupled to charge noise, leading to dephasing. [62]. The QD3 is the only potential candidate for generating high-quality SPS.

The pulse width is shaped by a Volume Bragg Grating (VBG) setup, to reduce the excitation bandwidth and thus the laser background. Subsequently, a optimized pulsed laser is employed for the deterministic resonance fluorescence (RF). Before operation of the RF, quasi-resonant pulsed excitation was performed to measure the radiative lifetime of the three QDs shown in Fig. 4.9. The measured lifetime are 2.5 ±0.007 ns,

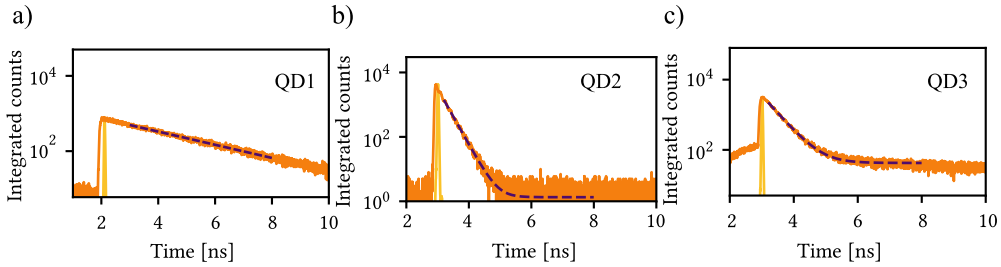

Figure 4.9: The radiative lifetime measurements of the three dots under pulsed p-shell excitation shown in orange. The instrumental response function (IRF) of the SNSPD is printed in yellow. Equation 1.8 is used to fit the data printed in dashed purpel.

250 ±2 ps, 420±4 ps, respectively. The average lifetime of the QDs in the nearby bulk is ∼ 1.1 ns see appendix A.3. Using equation 1.31, we calculate the Purcell factors to be 0.44, 4.4, 2.6. QD1 shows a suppressed emission rate compared to bulk, likely due to its position being in a node of the PCW Bloch function. QD2 instead, is probably located closer to the anti-node of the optical waveguide mode as it shows Purcell enhancement while having a similar frequency as QD1. However, the Purcell enhancement does not seem enough to mitigate the spectral noise in this dot. Therefore, this confirms the initial choice of using QD3, on which further characterization have been carried out.

In order to characterize the purity of the single photons emitted by QD 3, we perforemed an HBT experiment. The resulting second order correlation measurement is shown in Fig. 4.2 a). Which shows the correlation histogram at long time scales $g^{(2)}(\tau)$, a bunching towards $\tau = 0$ is Remarkable. We attribute this partially to the blinking of the transition exchange between a bright exciton to a dark exciton induced by spin-flip. The dark exciton transformed from an bright exciton via spin-flip is possible to go back while the dot is in a bright state. Therefore one more bright exciton is ready to emit a photon as discussed in section1.2.3. The main reason is attributed to artifacts of the time-tagger. Compared to the time jitter at longer time delay, the shorter delay time shows lower jitter. Since the time-tagger has an intrinsic delay-time-dependent jitter. This artifact can be mitigated by calculating the area under the peaks instead of the peak maxima. For the $g^{(2)}(0)$ calculation, we normalized the central peak to a peak at long time scale.

The correlation curve decays exponentially at long time scale ∼ 1 μs, which falls in the time scale of QDs blinking [81]. Zooming in to the short time scale window of the correlation histogram, intensity fluctuation of individual correlation peak caused by the time-tagger jitter is visible.

A good spatial separation between the excitation spot and the collection grating ensures a very high suppression of the pumping resonant laser. This has been obtained without using any polarization filtering, that could result in collection losses by increasing in the laser power. A clear Rabi oscillation under pulsed resonant excitation of QD3 is observed shown in Fig. 4.11 a). Here, the laser background has been subtracted

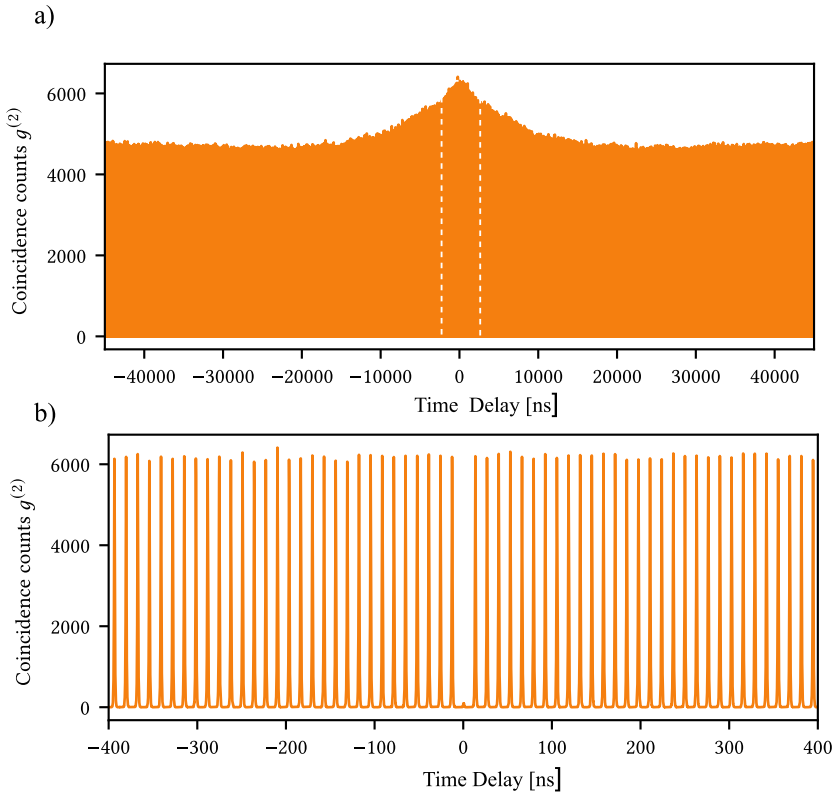

Figure 4.10: The second order correlation histograms at different time scales. a) shows the correlation histogram at long time scales where individual peaks can not be distinguished. b) Zoom in to the central correlation histogram in a narrow time window, the correlation intensity fluctuates.

from the intensity data. The maximum count rate extracted at π pulse is 12.58 MHz in-fiber. On QD3, we can achieve a noise-to-signal ratio of 0.0054 at π pulse after etalon filtering. The center region of the correlation data from Fig. 4.11 b) is fitted in order to extract the area under the cental peak. The fit is displayed in Fig. 4.11 b), and by comparing to the area of a long timescale peak we calculate a $g^{(2)}(0)$ is (1.7 ±1%. The main contribution to the non-zero g2, is a small amount of residual laser background.

The indistinguishability of the single photons emitted from the QD3 at π pulse was measured using the HOM setup presented in Fig. 4.4 a). Two-photon interference coincident intensity was measured as a function of angles of the $\lambda/2$ waveplate and thereby gradually changing between cross- and co- polarized configurations. We calculate and plot the integrated number of counts in the central peak relative to the side peaks in Fig. 4.11 c). This shows a visibility fringe following a cosine, where the ratio of the max and min corresponds to the the interference visibility. The corresponding co-polarization and cross-polarization correlation central peaks are plotted in 4.11 d).

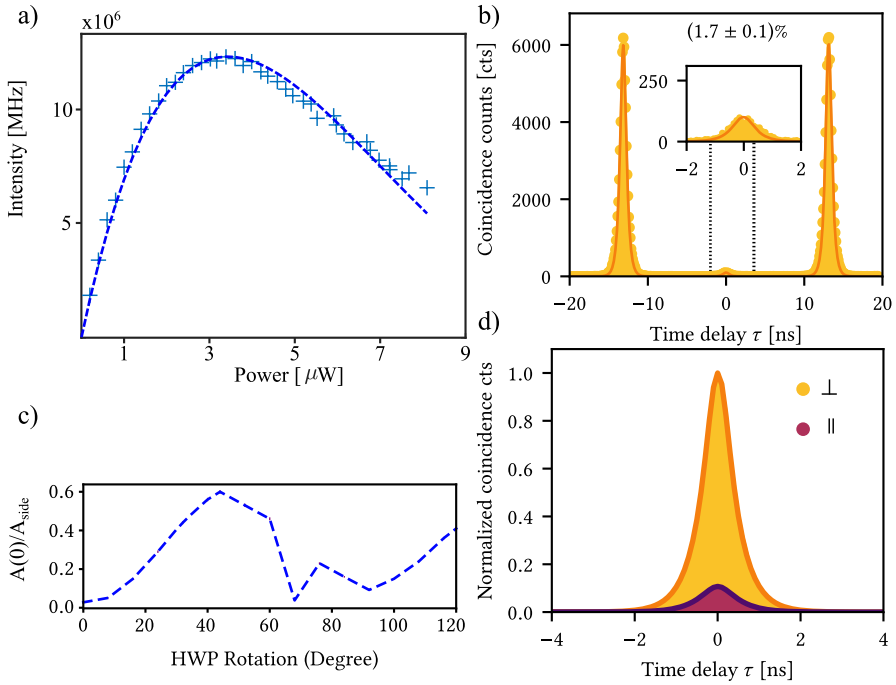

Figure 4.11: Characterization of the single-photon source. a) Intensity as a function of excitation power, showing Rabi oscillations (dashed blue line is a fit to the data). b) Photon purity measurement in the HBT setup under π pulse excitation. c) Two-photon interference measured at various half-wave plate angles to identify the co-polarization and cross-polarization configuration in the setup. d) Photon indistinguishability measurement under π pulse excitation.

The orange curve denotes the cross polarization meaning that the photons will be distinguishable and the purple curve denotes the co-polarization, i.e the indistinguishable case, which displays a clear suppression of the central peak. As already discussed in section 4.1.2, the residual central peak counts in co-polarization configuration result from 1) the laser background, which can be identified by $g^{(2)}(0)$, 2) the imperfection of the HOM setup (see table 4.2.3), 3) distinguishable photons. The measured HOM visibility is $V_{\text{raw}} = (93.36 \pm 0.08)\%$. By compensating for the setup imperfections and the purity, according to equation 4.13, the intrinsic HOM visibility is $V_{\text{intrinsic}} = (97.14 \pm 0.89)\%$.

In conclusion, a deterministic and on-demand SPS with 12.58 MHz count rate in-fiber, high indistinguishability ($(97.14 \pm 0.89)\%$) and purity ($(98.3 \pm 0.1)\%$) has been achieved in a QD coupled to single side PCW system.

4.4.2 Other types of single photon sources

In this project, I also developed additional devices used for near-ideal SPS, In the following these two will be briefly introduced.

Dual-mode waveguide-based resonant excitation source

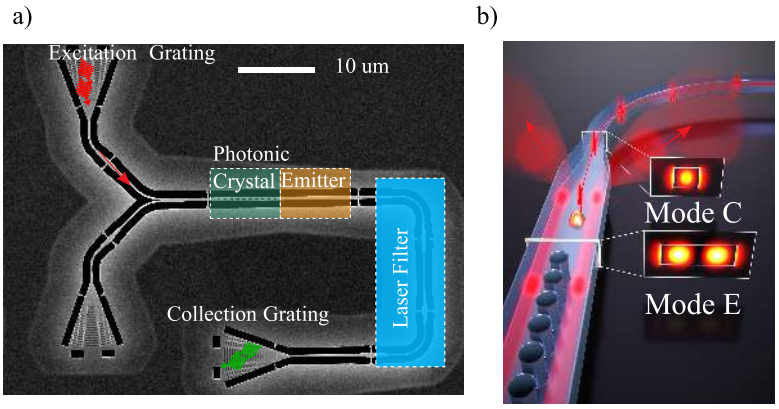

Figure 4.12: On-chip realization of in-plane resontant excitation, using QDs coupled to a dual-mode waveguide. a) SEM image of the device. A Y-splitter couples the excitation laser in a superposition of even and odd modes, while the photonic crystal selectively transmits only the first-order mode to the emitter section. b) Artistic view of the mode filtering operation, where the first-order mode carrying the resonant excitation laser is squeezed out of the waveguide using a linear taper. From [69].

A SPS based on QDs coupled to dual-mode waveguides has been realized [25] using the fabrication process outlined in Chapter 2. A special designed planar nano-photonic waveguide has been designed, enabling the resonant pulsed excitation using a laser directly launched into the first-order mode of a waveguide (instead of out-of-plane excitation). The emitters emit predominantly in the fundamental mode of the waveguide, while the excitation laser is filtered out by an adiabatic taper. The operational principle of this device is presented in Fig. 4.12. Selectively coupling the excitation laser into the first-order mode (Mode E), the QD is excited and the emitted single photons are collected through fundamental mode (Mode C) is shown in Fig. 4.12 b). A tapered waveguide is inserted to realize filter out the excitation laser and transmitting the emitted single photons. The key components of this device are highlighted in Fig. 4.12 a), namely a photonic crystal that selectively prepares the laser in Mode E and acts as a back-reflector for Mode C, the emitter section, and the laser filter.

Deterministic single photons with high purity and indistinguishability have been demonstrated in this system. The $g^{(2)}(0)$ is (2 ± 0.5) % indicating an efficient laser background filtering, while the measured indistinguishability reaches (96 ± 2) %. Besides the high source quality, there are two pronounced advantages of this planar

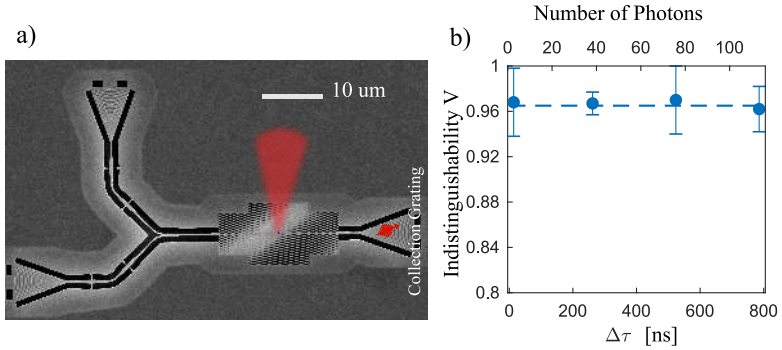

Figure 4.13: Single-photon sources obtained by QDs coupled to a photonic crystal waveguide. a) SEM image of the device. b) Indistinguishability of photon pairs in a string of 115 photons exceeds 96 % [25].

nanophotonic circuit system 1) it shows a broadband and robust excitation process implying that the device can be performed continuously without any alignment for days. 2) it is a plug-and-play design, potentially suitable for integration and scaling. In fact, unlike out-of-plane excitation, it enables pumping multiple QDs parallelly by one excitation pulse and a waveguide distribution network. The results presented here has been published in [69].

A source of multiple indistinguishable photons

A source of > 100 photons with pairwise photon indistinguishability beyond 96% has been achieved using a QDs coupled to a photonic crystal waveguide (PCW) system. Fig. 4.13 a) displays the device used in this measurement, which consists of an central slow-light PCW region with a length of 10 μm between two fast-light PCW with length of 5 μm. An optimized laser pulse with a pulse duration of $\sim$ 20 ps is used to deterministically populate the exciton transition. The emitted single photons are coupled to the PCW which enables the embedded QDs be coupled with near-unity efficiency. Subsequently the single photons are efficiently out-coupled from the chip by shallow etched gratings. Similar as for the single-sided device we have high efficiency and good laser suppression. And the high quality material as well as low-noise electrical gates control the decoherence time over a large time scale.

Long strings of indistinguishable photons are shown in Fig. 4.13 b), where four representative time intervals $[1\tau_p, 38\tau_p, 76\tau_p, 114\tau_p]$ are measured (τ_p is the laser repetition period). The last one corresponds to maximum time delay between two photons of 786.6 ns. The indistinguishability remains stable and over 96% for delays corresponding to 115 subsequently emitted photons, which is potentially enough to demonstrate quantum advantage, provided an efficient de-multiplexing scheme is used [27].

At π pulse, a single-photon count rate of 10.4 MHz for a 145 MHz pump laser repetition rate has been observed, which indicates an in-fiber efficiency of 7 %. The collection efficiency is limited by the directionality efficiency for this device being 50 %,

because the device employed for this measurements is two-sided, while the collection path and filtering efficiency is optimized to $(35 \pm 1)\%$. The data presented here has been published in [25].

4.5 The state-of-the-art of single-photon sources based on quantum dots

To conclude this chapter, we provide a comparison of the SPS developed in this work with the state-of-the-art.

The integration of a QD source in a nanophotonic structure typically leads to a reduced photon indistinguishability due to the increased charge noise from the nearby etched surface. A promising approach to overcome this effect is to introduce Purcell enhancement to shorten the radiative emission time. Fig. 4.14 a) shows an example of QDs coupled to a photonic crystal cavity that we measrued, and is terminated with out-couplers. Such a system is favored since the dephasing on the QDs emission can be mitigated as well as the count rate can be maximized by the Purcell effect. The lifetime of the emitter in this system is 22.7 ps corresponding to a Purcell factor $F_\mathrm{p} \sim 40$. The $g^{(2)}(0)$ at π pulse is 0.0026, which is limited by the extinction of the laser background using spatial separation similar to us. The measured HOM visibility is 93.9 %, which can be further improved by increasing the cavity quality factor, which is limited by the surface roughness [23].

A high laser background extinction has been realized in the devices shown in Fig. 4.14 b) and c). A QD is coupled to an elliptical vertical cavity in the Purcell regime. Compared to the isotropic microcavity, this cavity system can single out a polarized two-level system and obtain a near-background free collection of single photons under resonant fluorescence with little efficiency loss. In [24] the authors designed two types of the polarized cavity to realize such a two-polarization scheme. Fig. 4.14 b) illustrates narrow-band elliptical micropillar cavities, where the two non-degenerate cavity modes are aligned to the minor and major axes. Fig. 4.14 c) shows a similar concept, using broadband elliptical Bragg gratings for collecting light.

Near-unity indistinguishability and high efficiency SPSs are obtained (see table 4.5). The imperfection of $g^{(2)}(0)$ for the micropillar cavity caused by laser leakage. Detailed photon loss characterization indicated that in the elliptical micro-pillar system, the predominant loss mechanisms contain imperfect sidewall scattering, mode leakage, and imperfect inter quantum efficiency. For the elliptical Bragg grating system, the main loss comes from the QD blinking since the QD position is close to the etched surface [24].

Gated QDs coupled to an open, tunable microcavity is illustrated in Fig. 4.14 d). The gate can give an control of the charge noise and Stark-tune the emission frequency. The tunability of such a microcavity allows compensating for the lack of control over the QD emission frequency and position. Moreover, the output of the cavity mode matches the single-mode fiber well, which allows multiple degrees of freedom on the control of QDs performance.

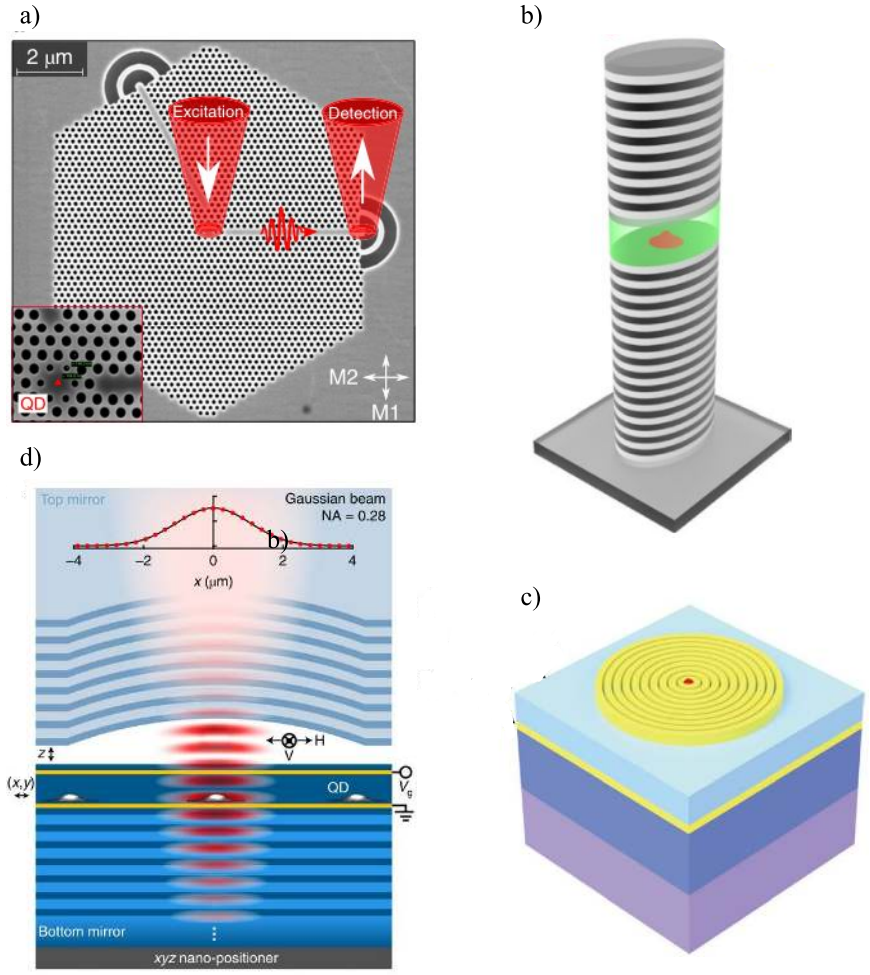

Figure 4.14: Illustrate three representative In(Ga)As QDs based SPSs systems. a) High indistinguishable SPS is generated by QDs coupled to a photonic crystal cavity system. The SEM image of the device, QDs are excited on top of the cavity and collected through the out-coupler [23]. b) and c) An optimal SPS is generated by QDs coupled to polarized microcavities [24]. b) Schematic structure of a QD coupled to an elliptical micropillar cavity device. c) A QD coupled to an elliptical Bragg grating structure consisting of a central elliptical disk, surrounding elliptical grating, and fully etched trenches. d) A bright and efficient SPS is generated by QDs coupled to an open cavity system [26]. Schematic display of the system, an open cavity is formed by a top concave mirror fabricated in a silica substrate, and the counterpart is a distributed Bragg reflector making up the emitters substrate. A simulation curve shows (red points) the output is very close to the Gaussian beam. The position of the bottom ensemble can be adjusted with respect to the top mirror using an xyz nano-positioner.

On-chip laser background filtering is also realized in this system. The radiative lifetime of the QDs in this system is around 47.5 ps, Purcell enhanced by a factor

of ~ 10. The measured $g^{(2)}(0)$ is limited by small amount of the laser leakage into the detection channel and double excitation events. It is really impressive that the chip-to-fiber efficiency reaches valuies as high as (96 ± 2%) and the limitation on the overall efficiency lies in the efficiency of the collection optics [26].

In conclusion, table 4.5 summarizes the key properties of some state-of-the-art SPSs based on self-assembled QDs coupled to different nanophotonic devices. A comparison to the devices shown in this work is also provided.

Reference	Lifetime (ps)	$g^{(2)}(0)$	HOM visibility	SPS efficiency
Phc-Cavity [23]	22.7	0.026± 0.007	0.939	
Micro-Cavity [24]	61	0.025±0.005	0.975±0.006	0.56±0.02
	69.1	0.009±0.003	0.951±0.005	0.6±0.02
Open-Cavity [26]	47.5	0.021±0.001	0.967	0.57
PCW [25]	346	0.015±0.005	0.96 ±0.02	0.07
In-plane [69]	700	0.020±0.005	0.96 ±0.02	0.05
This work	440	0.017±0.001	0.97 ±0.0089	0.0847

Table 4.5 concludes the state-of-the-art SPSs produced from self-assembled QDs coupled to nanostructures.

* * *

In this chapter we presented the high-performance SPSs generated by self-assembled InAs/GaAs QDs coupled to photonic nano-structures developed in this thesis. We provided an overview of the three fundamental properties used to evaluate SPS quality and review the state of the art. We have achieved optimized sources of single photons with high purity and indistinguishability. These sources constitute the starting point towards the demonstration of quantum advantage using photonic qubits.

CHAPTER 5

Phonon Decoherence of Quantum Dots Coupled to Photonic Crystal Waveguides

Observing and quantifying the effect of photons on decoherence of single-photon emission from In(Ga)As QDs couple to photonic crystal waveguides (PCW).

Near-ideal and coherent single-photon sources (SPS) generated using QDs coupled to solid-state nanostructures are realized [23–26, 69]. Coherence depends sensitively on the noise inherent to the nano-structures and the environment surrounding the QDs, therefore understanding the noise mechanism allows us to optimize the SPS performance. To date, experimental investigation of the decoherence of QDs is mostly performed on bulk systems, but is not yet fully developed for QDs coupled to nano-devices systems. In this chapter, the relevant decoherence processes are presented, with a special focus on phonon-induced dephasing. Experimental evidence of the temperature-induced decoherence is quantified, allowing us to derive a relation between the photon indistinguishability and operation temperature.

5.1 Decoherence mechanisms

Decoherence arises from the coupling between a quantum system with its fluctuating environment. Solid-state emitters like QDs in nanostructures naturally couple with their host material, making the control of the noise coupled from the surroundings particularly challenging. There are three main decoherence processes specific to solid-

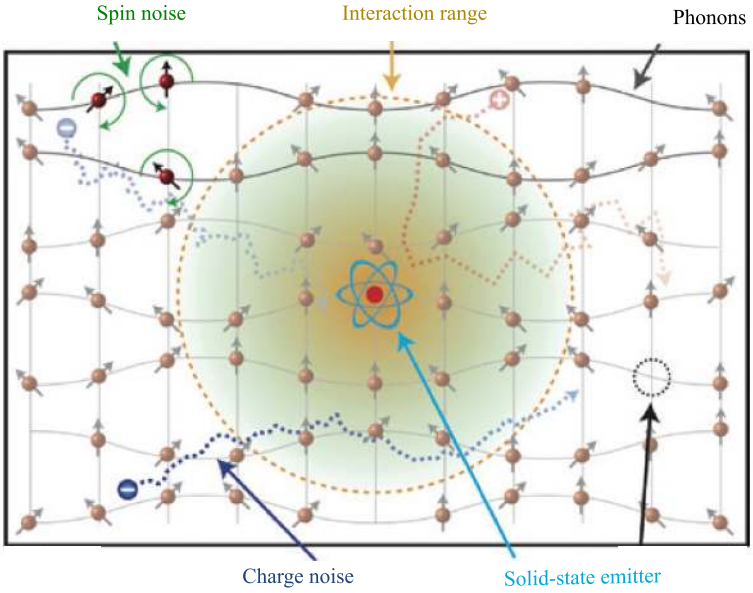

Figure 5.1: Schematic representation of relevant decoherence processes for solid-state emitters coupled to various noise sources, including charges, nuclear spins, and phonons [82].

state system as sketched in Fig. 5.1, that is, phonon noise due to temperature, charge noise due to trapped charges in the vicinity of the emitter, and spin noise due to coupling of the emitters' electron spin to the nuclear spins of the atoms.

5.1.1 Charge noise

Surface states and defects inherent to the host material can trap charges in the proximity of a QD. Therefore, the fluctuating electric field due to charges being continuously trapped and released leads to decoherence in the QD excitons. This is illustrated in Fig. 5.2 a), b), which sketches the simplest case of an exciton coupled to either a loaded trap or an empty trap nearby. A visible energy shift of exciton transition is observed as shown in Fig. 5.2 c), d). Such an energy shift results in the tuning of the QDs emission wavelength. This mechanisms causes spectral diffusion and broadens the optical linewidth of a self-assembled QDs [84–86]. It is reported that the charge noise is typically small ≈ 1.2 µV and is limited to low frequencies [50]. The energy shift of the transition ΔE due to electric field $F_{h,z}$ created by charge noise shows direct proportionality $\Delta E \propto F_{h,z}$ [50]. This is the case for a single hole trapped in the QD as shown in Fig. 5.2 b) and where we only consider an electric field in the QDs growth direction z contributing to the Stark tuning. Both the hole and its corresponding charge in the metallic gates can contribute to the electric field, depending on the material configuration [50].

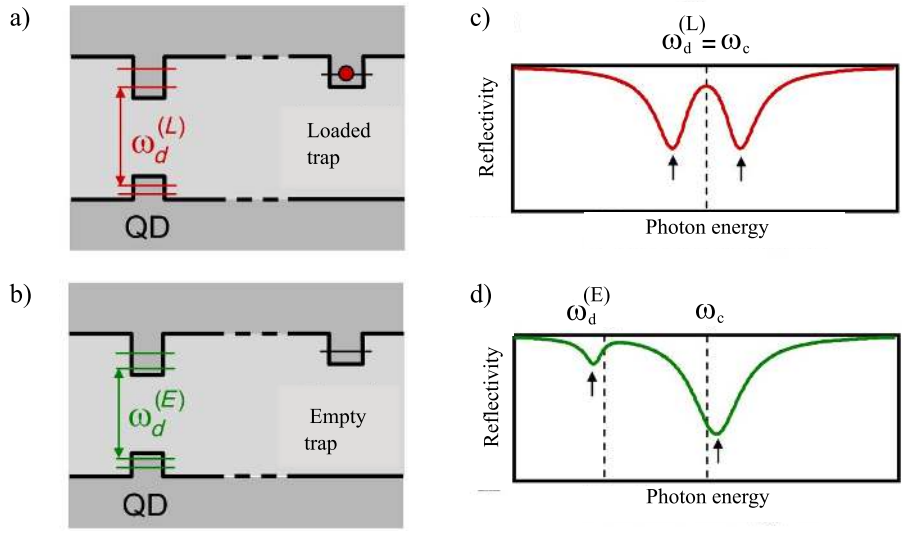

Figure 5.2: Energy shift of the exciton transition induced by capturing or releasing a single charge in the vicinity of a QD [83]. a), b) Sketch of the band diagrams of an In (Ga)As QD with respect to nearby loaded and empty trap, the corresponding transition energies of the QD are $\omega^{(L)}$d and $\omega_{\mathrm{d}}^{(E)}$. c), d) Reflectivity as a function of photon energy for a loaded and an empty trap.

To mitigate the effect of charge noise it is necessary to explore ultra-pure epitaxial growth of materials [87] and minimize the fabrication imperfections for reducing the density of defects. High-quality contact gates are employed to stabilize the electric field created by charge noise. Finally, experiments have demonstrated that applying a resonant excitation scheme on an ultrahigh quality material gated device can suppress charge noise to a large extent [25, 26, 50].

5.1.2 Spin noise

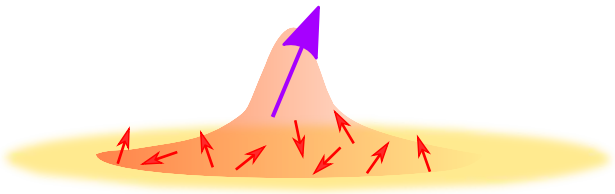

Figure 5.3: Sketch of the interaction picture of an electron spin (purple arrow) with many nuclear spins (red arrow) in a QD.

The nuclear spins of thousands of atoms forming the QDs orient randomly (as sketched in Fig. 5.3), thus result in a fluctuating magnetic field which couples to a confined electron spin in a QD [88–91]. This effect is known as the Overhauser field which can be as large as a few T in some cases, and generally with a standard deviation of few tens mT [90, 92]. The hyperfine interaction between the electron spin and the surrounding nuclear spins is reciprocal [92]. Akin to the Overhauser field, an effective magnetic field sensed by the nuclear spins is called the Knight field which originates from fluctuation of the confined electron spin. Importantly, such a hyperfine interaction also gives rise to a dynamical effect for the transfer of the two spin systems [93]. The existing and dynamical Overhauser field in a QD can result in decoherence of both spin and optical states.

We mainly focus on the spin noise that affects the optical states. Compared to charge noise, spin noise is predominant at higher frequencies, and offers essentially weaker noise powers but quite larger bandwidth [50]. Experiments have shown that spin noise significantly depends on the charges [94]. So once the charge noise can be quenched using a high-quality gated devices, spin noise effects can be circumvented [94]. Consequently, transform-limited QD emission linewidth has been achieved [50, 62, 94, 95], which provides a coherent light-matter interface for realizing quantum applications.

5.1.3 Phonon noise

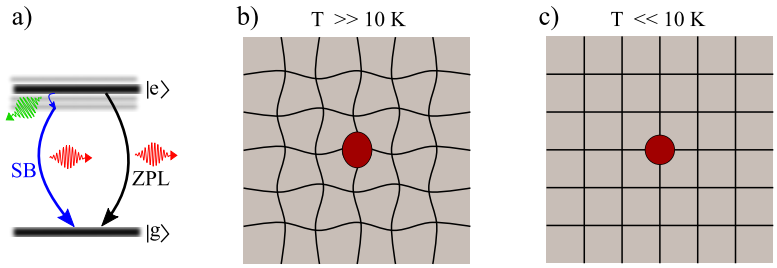

Figure 5.4: A QD two-level system coupled to phonons. a) Describe the scenario of a QD decaying from its excited state, $|e\rangle$, to its ground state,$|g\rangle$, emitting or absorbing a phonon, leading to an emission spectrum composed of a broad phonon sideband (SB) and a narrow zero-phonon line (ZPL). b) Sketch of the surrounding lattice vibration strength of a QD at relatively high temperature, c) Suppressed lattice vibration at low temperature.

An exciton created in a QD inevitably couples to phonon modes induced by vibration of its host solid-state lattice, leading to a decoherence process in the QD transition. This decoherence is a fundamental limitation for QD-based SPS. The phonon coupling transforms a QD two-level system into a multiple level system as sketched in Fig. 5.4 a). A photon is emitted with energy lower than a QD exciton when the QD decays from its excited state to ground state with the emission of a phonon simultaneously. Similarly, a phonon can also be absorbed by the QD, resulting in the emission of blue-tuned

photons. The photons emitted in such phonon-mediated transitions possess various energies depending on the emitted (absorbed) phonon energies. This "jitter" in the emission energy (or equivalently the frequency) of the photons causes subsequent photon emissions to be distinguishable. The resulting emission from the QD exhibits a broad sideband (SB) in the vicinity of a narrow zero-phonon line (ZPL) that corresponds to a transition without phonon as shown in Fig. (4.5) in chapter 4.

The incoherent photons can be filtered benefiting from the large spectrum mismatch between the SB and ZPL. Such filtering is widely applied in the indistinguishability measurement on the QDs-based SPS [22], but it undermines the source efficiency due to the intrinsic absorption from the filter. Vibrational phonons influence both efficiency and coherence of the SPS [48, 96–98]. The energy exchange of an exciton with phonons results in emission of distinguishable photons in SB, known as non-Markovian process [99]. When an exciton is elastically scattered by phonons (Markovian process), it results in a broadening of the ZPL. Such a process simply “blurs” the transition energy without causing any relaxation of population, and it is therefore called pure dephasing [96]. The density of the vibrational phonon modes depends on the temperature, and hence cooling down the sample is the most effective way to suppress phonon noise. As artistically illustrated in Fig. 5.4 b) and c), the vibration strength can be greatly suppressed at cryogenic temperature. Alternatively, coupling QDs to nano-devices like micro-cavities with a narrow bandwidth enables to selectively enhance the ZPL due to Purcell enhancement, as well as filter the phonon SB [100]. The photonic nano-devices designed for QDs can be divided into two categories, waveguides or cavities. Compared to a micro-cavity which works only in a narrow bandwidth, a waveguide provides a broadband radiation modes allowing almost all the exciton transitions of inhomogeneous QDs stemming from the nature of SK-growth mode, but lacks of selection of spectrum.

5.2 Theoretical model of phonon decoherence in QDs transitions

Earlier work developed a general model for the interaction of vibrational phonons with In(Ga)As QDs in four typical experimental systems of bulk, slab, waveguide, and cavity [101]. These photonic structures correspond to different dimensions (3D, 2D, 1D, and 0D) of the nanostructure embedding the quantum dot. A general electron-phonon Hamiltonian any of the systems above read as [101]

$$H = \hbar\omega_{01} |1\rangle \langle 1| + \sum_{q} \hbar\omega_q a_q^\dagger a_q + V |1\rangle \langle 1| , \tag{5.1}$$

Here $|1\rangle$ is the excited state of the QD and $\hbar\omega_{01}$ is the transition energy, $a_q^\dagger$ (a_q) is the phonon mode creation (annihilation) operator with momentum q and energy $\hbar\omega_q$. The interaction Hamiltonian $V=V_L + V_Q$ contains a linear and a quadratic coupling of phonons with the QD. The linear coupling leads to the broad phonon SB emission due to rapid phonon absorption (emission) on a ps time scale, while the quadratic coupling results in the broadening of the ZPL on the time scale of the QD radiative decay since

the exciton is elastically scattered to a higher state. Phonon SB can be filtered, and the fundamental limit to the QD decoherence is thereby the quadratic coupling. However the free mechanical expansion of nano-devices leads to long wavelength vibration, which can broaden the ZPL in the form of linear coupling.

Figure 5.5 displays the error in two photon indistinguishability (TPI) of the four systems as a function of temperature. TPI in terms of decay rate can be written according to equation 4.10 discussed in chapter 4.

$$TPI = \frac{\Gamma}{\Gamma + 2\Gamma_{dp}}, \tag{5.2}$$

where Γ and Γ_{dp} are radiative rate decay and depahsing rate,respectively.

We will briefly summarize the phonon decoherence mechanisms of different dimension systems shown in the Fig. 5.5.

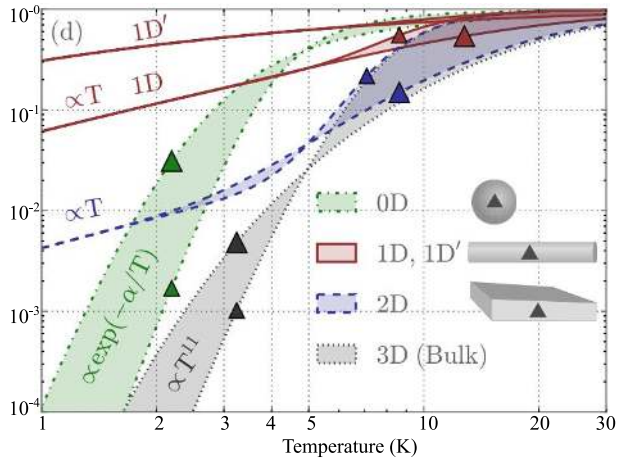

Figure 5.5: Error in two-photon indistinguishability (TPI) as a function of temperature for QDs coupled to nano-devices of different dimentionality. 0D denotes a QD located in a sphere (R= 80 nm) center, 1D (1D') is a QD placed in a cylindrical waveguide (ρ =80 nm)of the central cross-section(halfway off the center), 2D is for a QD positioned in the center of a free-standing membrane with a thickness of 160 nm, and 3D is a QD in the bulk. Each structure is illustrated with two curves corresponding to a small (L=1.5 nm) and large (4.5 nm) QD denoted by triangles [101].

- In bulk (3D), Γ_{dp} is only from the quadratic coupling and we label it as Γ_{3D}. At low temperatures, 1-TPI $\propto T^{11}$.
- In 0D cavity, Γ_{dp} is also only from the quadratic coupling because the phonons interact with QDs periodically. At low temperatures, 1-TPI $\propto \exp(-\hbar\omega 2k_B T)$.
- In a slab (1D) and a waveguide (2D), the total dephasing rate stems from the linear and quadratic coupling. The quadratic coupling does not deviate remarkably from

the bulk, because the nanostructure size is large enough that it does not influence the phonon modes. $\Gamma_{1(2)\mathrm{D}} = \Gamma_{\mathrm{L}}^{1(2)D} + \Gamma_{3\mathrm{D}}$. Regarding the linear interaction , it is quite complicated, and closely linked the nanostructure cross-sectional shape and the QD position. At a low temperature, 1-TPI $\propto$ T.

5.3 Experimental investigation of phonon decoherence in QDs

5.3.1 Preliminary characterization

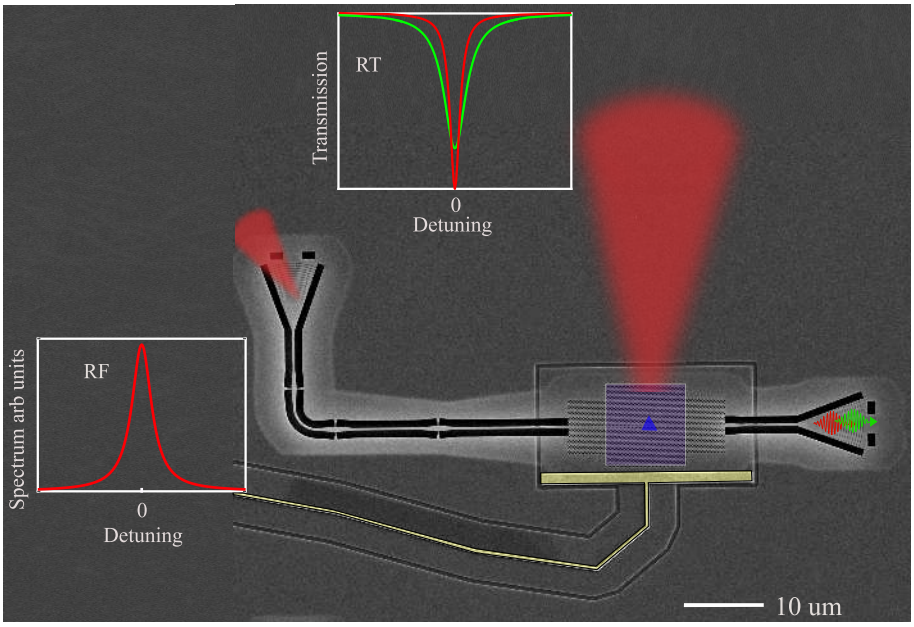

Figure 5.6: Illustrate the optical excitation schemes of resonant fluorescence (RF) and resonant transmission (RT) in PCW. For the RT (RF) characterization, the laser is coupled through input SEG (free space), and collected in the same SEG. The corresponding spectra (in red) are the ideal case of RT and RF without any dephasing. Considering a practical scenario, introducing pure dephasing (green curve) weakens the light-matter interaction and thereby allows transmission of partial on-resonant photons, resulting in broadening of the RT linewidth and decrease the RT dip.

In this work, we estimate the effect of phonon noise on the SPS realized by using by In (Ga)As QDs coupled to PCWs from two different approaches, measuring TPI under resonant fluorescence (RF) and linewidth of resonant transmission (RT) [85] spectra, as shown in Fig. 5.6. Strict RF is necessary here since the time jitter introduced by p-shell or above-band excitation leads to an uncertain single-photon emission time, which deteriorates HOM visibility. The linewidth is obtained from the RT spectrum mainly because it is a much more straightforward and robust measurement compared to recording RF spectrum. In RT, a weak laser is coupled to the QD through the waveguide.

Interference between the incident photons and the scattered photons is created. For a QD well coupled to the waveguide ($\beta = 1$) without any dephasing, the incident photon on-resonant with the QD results in destructive interference in transmission leading to reflection of resonant photons. Further, laser photons off-resonant with the QD transition will not interact with the QD and are transmitted.

Non-zero dephasing of the QD transition , shown as green curve in Fig. 1.6 RT spectrum inset, leads to a broader width and shallower dip, due to a reduced coherent interaction at the light-matter interface. The analytical expression used to model the RT spectra is [30, 102, 103]

$$T = \frac{[(\Gamma + 2\Gamma_{dp})((\beta-1)^2\Gamma + 2\Gamma_{dp}) + e\Delta\omega^2](1+\xi)^2}{(\Gamma + 2\Gamma_{dp})^2 + 4\Delta\omega^2 + 4\beta\Gamma\Delta\omega\xi + [((\beta-1)\Gamma - 2\Gamma_{dp})^2 + 4\Delta\omega^2]\xi^2}, \tag{5.3}$$

where Γ is the spontaneous decay rate, Γ_{dp} is the pure dephasing rate, β is the waveguide coupling factor, $\Delta\omega$ is the detuning between the laser frequency and the QD transition frequency, and ξ is the Fano factor of the nano-structure stemming from the residual reflection from the waveguide interface. The corresponding linewidth is given by $\Gamma_{RT} = (\Gamma + \Gamma_{dp}) + \sqrt{(1+S)}$ [30] with S being the power parameter presented in chapter 1.27. The following measurements are carried out on the setup presented in chapter 3.1.2.

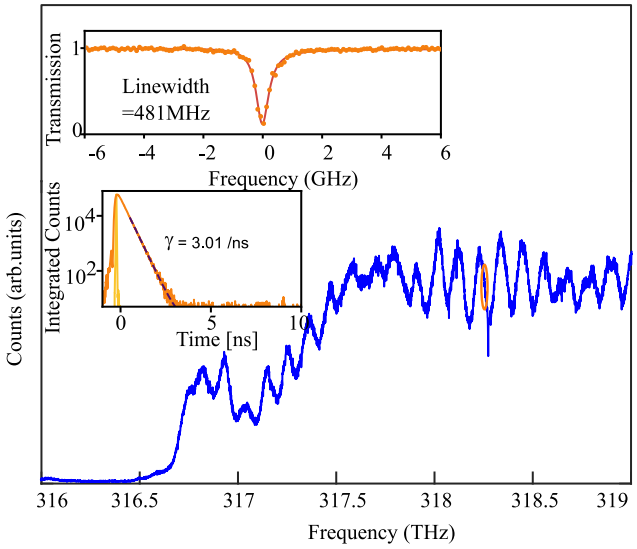

Figure 5.7: The basic characterization for the QD used in the following measurements. The cut-off frequency of the PCW (a= 248 nm and r= 70 nm) is 316.525 THZ, and the QD emission frequency is 318.2459 THz marked by a circle (orange) in the transmission spectrum (blue), 1.7 THz off the PCW bandedge. The QD under RF exhibits single exponentially decay and the fitting gives a radiative decay rate γ=3.01/ns. And the RT spectrum gives the linewidth using the model 5.3

.

The transmission spectrum of the PCW is shown in Fig. 5.7 and provides the frequency distance between the QD transition and the band edge, which is 1.7 THz (4.9 nm). The lifetime measurement is performed under pulsed RF as presented in chapter 4. The extracted decay rate γ is 3.01 $\pm$0.008ns^{-1}, corresponding to a lifetime of 333 $\pm$12.5 ps. The corresponding natural linewidth is $\Gamma = \gamma/2\pi$ =479.1$\pm$1.3 MHz. The average lifetime of QDs in the nearby bulk measured in the appendixA.3 $\approx$ 1 ns, indicating that the QD coupled to the PCW shows a small Purcell enhancement with Purcell factor $\approx$ 3.

The RT spectrum is fitted using the model equation 5.3, extracting a linewidth of Γ_{RT}=481 MHz shown in Fig. 5.7 top. The RT line shows a slight Fano-asymmetric shape resulting from the interference of the QD RF and the weak reflection from the interface of fast light and slow light (Fig. 5.6 SEM shows the false-color region interfaced with the slow region) [30]. We measure Γ_{RT}/Γ = 1.004, indicating that we achieve near transform-limited QD transition benefiting from strong suppression of the charge noise and spin noise. Thus the decoherence is created only by the phonon noise in the following measurements.

5.3.2 TPI measurement

As presented in chapter 4.2.3, we can apply corrections on the raw HOM visibility to get an intrinsic value for comparing the TPI values from different setups. So the $g^2(0)$ measurements here are not only acquired for extracting the purity of the SPS but also for calibrating the indistinguishability. We carry out HBT and HOM measurements from 1.6K to 8.5K with a step of 1K and from 10K to 18 K with a step of 2K.

Here, we selectively display four typical temperature figures fitted using relevant models. Fig. 5.8 shows the correlation histogram of the HBT measurement. Each row corresponds to the HBT measurements acquired at the same temperature, but with different excitation power, the $g^{(2)}(0)$ value is larger at π-pulse, mainly because of increased laser background. Each column compares the HBT measurements at the same excitation power, but at different temperature. Here the $g^2(0)$ value stays roughly 1 % level with some fluctuations. Under low power excitation, some of the data sets could not be fitted well due to the small number of coincidence counts in the central peak.

Alongside the fluctuations, at low-power there could be a weak increase in $g^{(2)}(0)$, which we speculate that increasing temperature gradually activates surface states, and the surface scattering thereby strengthens. On the one hand, the higher the temperature, the more the scattering, which consequently weakens the laser background suppression. Surface states are usually not stable, probably resulting in fluctuating laser scattering at high power. But this does not affect our TPI value calibration because we trace the extinction on both HBT and HOM measurement and ensure the extinction on HOM measurement is larger than the HBT, thus ensure not to overestimate the corrected TPI value.

HOM interference multi-peaks are fitted also using equation $g^{(2)}(\tau)$, but the central peaks are fitted with an additional dephasing contribution presented in equation 4.8.

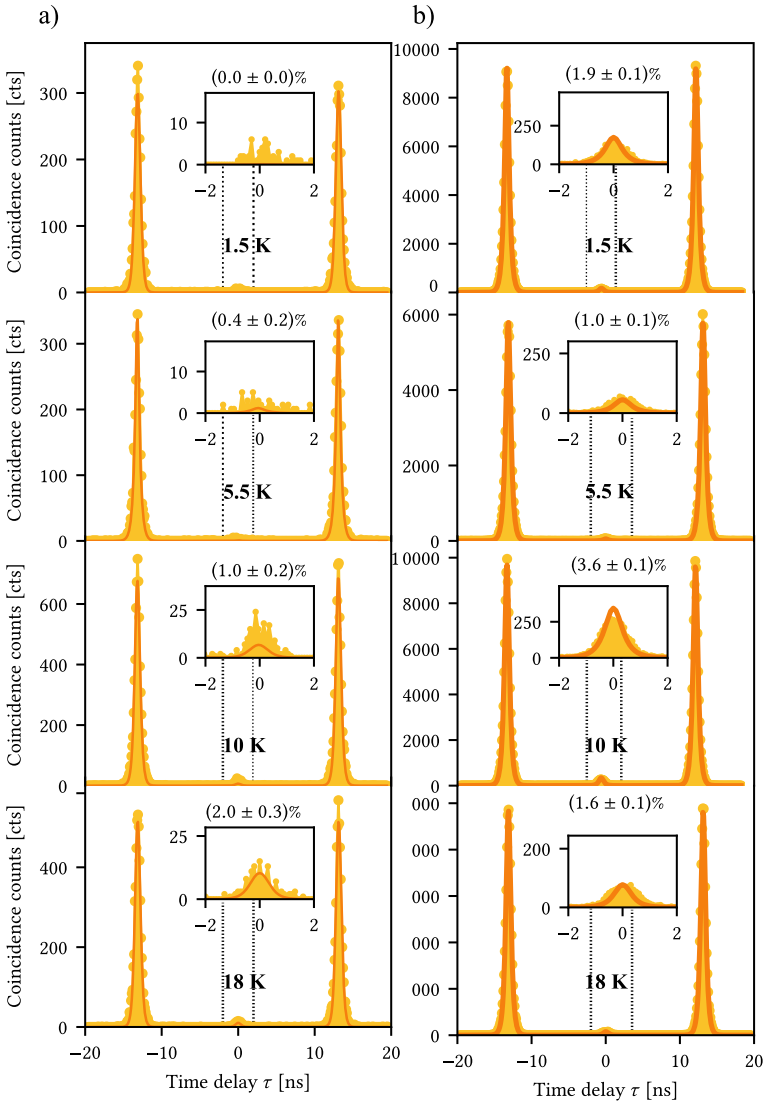

Figure 5.8: Correlation histograms are obtained on HBT measurements at varying temperatures from 1.6 K to 18 K under a) 10 % π pulse and b) π pulse RF, respectively. Here we show the fits at 1.5K, 5.5K, 10K, and 18K.

Fig. 5.9 shows the fits of central peaks of cross (orange) and co-polarized (red) HOM interference measurements. A strong central peak suppression is observed in the co-polarized configuration. We attribute the residual counts in the central peak to 1) imperfect single-photon purity due to coupling laser background, 2) the imperfection of the HOM setup described in 4.2.3, 3) a small degree of distinguishability of the single

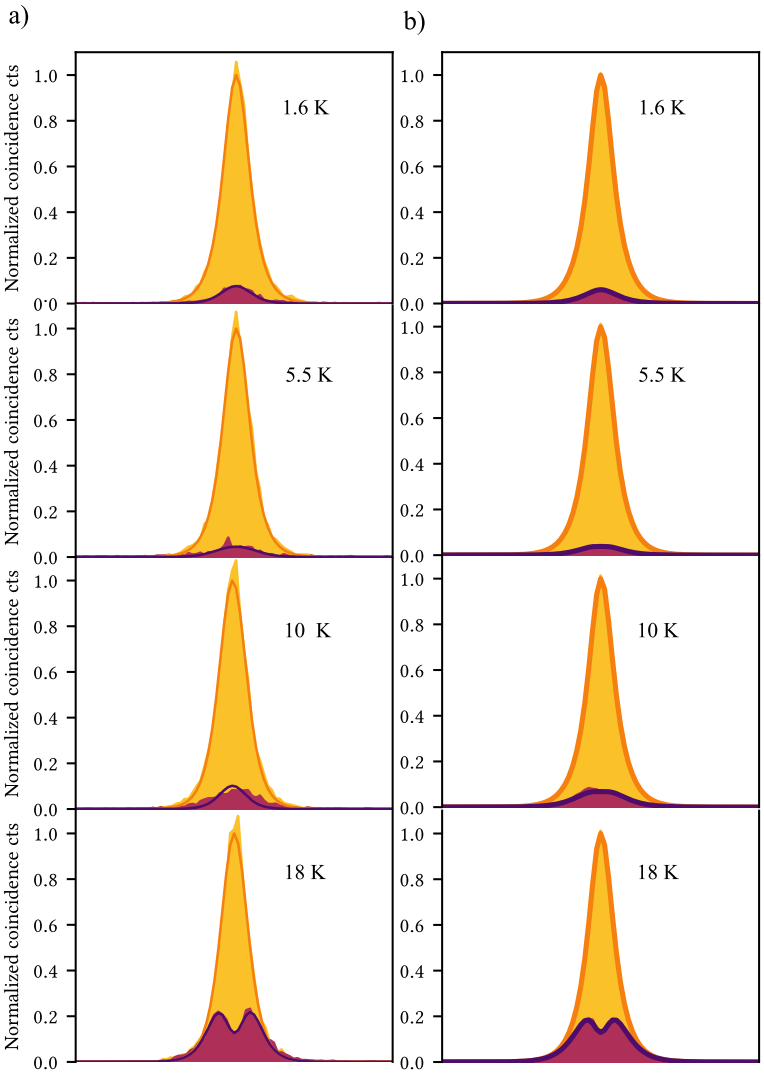

Figure 5.9: TPI measurements on the HOM setup at varied temperatures under a) 10 % π pulse and b) π pulse RF respectively. Both cross (red) and co-polarized central peaks are normalized a peak of longer time scale. As expected, pure dephasing is visible at high temperature.

photons because of arising from elastic phonon scattering induced. A dip appears at the co-polarized central peak at high temperature, indicating pure dephasing (Fig. 4.4 b)) [79].

In Fig. 5.10, the extinction, $g^{(2)}(0)$ and TPI are plotted as a function of temperature. The extinction fluctuations decrease with an increment of the temperature . Generally,

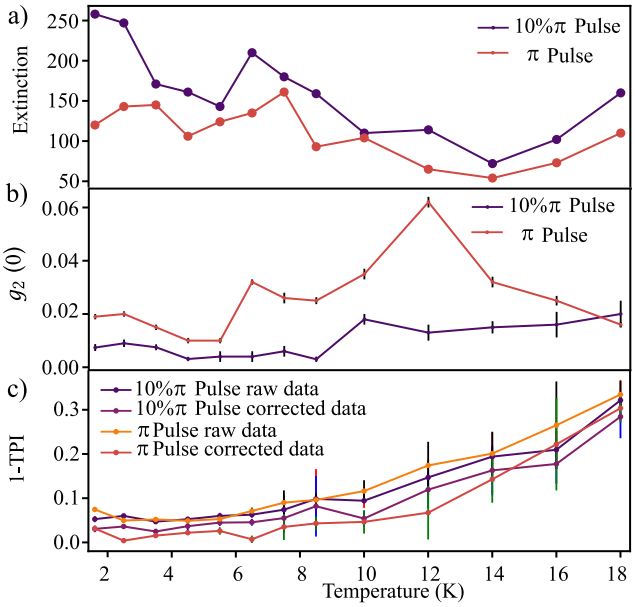

Figure 5.10: Temperature tuning measurements of the QD under RF with 10% π pulse and π pulse respectively. a) Extinction (signal to noise ratio) vs temperature. b) Extracted $g^2(0)$ shows anti-bunching at all temperatures. c) Raw data and intrinsic data (applying corrections) of error TPI as a function of temperature. At a temperature below 5.5K, the error TPI slightly fluctuates, then slowly increases until 10 K, and subsequently goes up fast from 12 K to 18 K.

multi-photon emission and un-rejected laser background mainly contribute to the non-zero $g^{(2)}(0)$. This measurement is done in RF with a bandwidth-shaped (short pulse length 20 ps) pulsed laser. Thus the purity imperfection arises from the limited suppression of the laser background and $g^{(2)}(0)$, therefore, it shows a variation consistent with the extinction (Fig. 5.10 b). Here one could use $g^{(2)}(0) = 2\xi - \xi^2$($\xi$=1/extinction) if you use purity as the metric. The error in TPI given in Fig. 5.10 c) provides information about the phonon impact on the decoherence of SPS generated by QDs in PCWs.

We plot both TPI curves of raw data and corrected data to confirm our characterization operates properly. And only the corrected data are used to model the impact of phonon scattering in the subsequent discussion. Firstly, Fig. 5.10 c) shows that the discrepancy between the curve of 10 % π pulse (purple) and the curve of π pulse (red) is mostly due to measurement errors. At a defined excitation power, for example, at π pule, it shows that the 1-TPI asymptotically approaches 0.015 as T$\geqq$ 0, with measured values nearly error-limited below 5.5K., indicating the phonon noise is effectively quenched in PCW within the resolution of the detectors. 1-TPI slowly increases between 5.5K and 10K, but subsequently increases rapidly as temperature increases to 18K.

As discussed in section 5.2, only ZPL broadening comprising a quadratic and linear interaction contributes to the dephasing. The quadratic coupling in the PCW is sup-

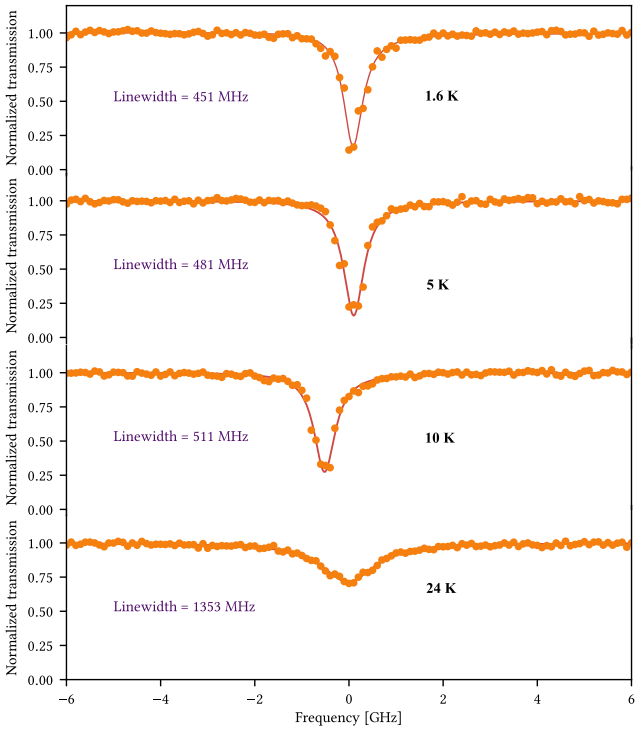

Figure 5.11: RT measurements on the QD from temperature 1.6 K to 24 K for the corresponding linewidth. It is estimated as the full width at half maximum (FWHM) of fitting model 5.3.

posed to degrade the indistinguishability in a similar strength as in bulk. It has been demonstrated for QDs in bulk, that if the temperature is kept below 10K, the mean energy of phonons is not enough to trigger the virtual transitions ($\Gamma_{dp} \ll \Gamma$). In contrast, at a temperature over 10K, the thermal energy is sufficient to populate the exciton in a higher state of p states, resulting in pure dephasing and consequently degrading indistinguishability [99]. Compared to quadratic coupling, the linear interaction can be either the Markovian or Non-Markovian in nature. In conclusion, our measurement indicates: 1) the phonon noise effect can be strongly suppressed 5.5k, 2) The dephasing process from 5.5K to 10K is induced by linear interaction due to long-wavelength vibration created by free vibrations of the nano-structures [101], and 3) The dephasing is dominant by the acoustic-phonon coupling [48, 99]over 10K.

Compared to the 2D model in equation.5.5, the 1-TPI value obtained from our measurements shows a similar variation trend as a function of temperature, but slightly larger than than the model value at a temperature below 5K, indicating a worse coherence. Since the PCW has a more complicated structure, the etched holes can slow down long-wavelength phonons [101].

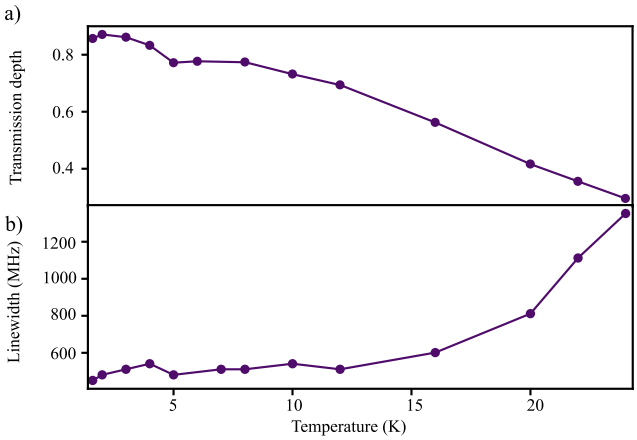

Figure 5.12: The extracted fitting data of RT depth and linewidth from model (5.3) are plotted as a function of temperature.

5.3.3 RT linewidth measurement

Temperature tuning of RT linewidths are measured from 2K to 8K with a step of 1K and from 10K to 24K with 2K steps. Model 5.3 is used to fit RT line shape and extract the line width as FWHM, and here we selectively show four typical temperature RT line fit figures as shown in Fig. 5.11. Compared to the line shape at 1.6K, the dip gets shallower and broaden remarkably. We use four free fitting parameters of β, Γ, Γ_{dp} and ξ. Thus the pure dephasing Γ_{dp} extracted from this fitting model is not reliable since the competition of different parameters reduces the confidence of the fit. So we focus on the RT depth and especially the line width to see how phonons broaden the line width as a function of temperature.

As shown in Fig. 5.12, below 10K, the RT line depth slowly reduces, and the line width slightly fluctuates around the natural linewidth, while over 10K, the RT depth decreases rapidly, and the line width broadens pronouncedly. As expected, the phonon behavior on the linewidth broadening is consistent with what we observed in the TPI. At a temperature below 10K, $\Gamma_{\text{dp}} \ll \Gamma$, and linewidth broadening is minor. However, over 20K, the linewidth broadening is >2 Γ implying the $\Gamma_{\text{dp}} > \Gamma$.

* * *

In this chapter, we experimentally characterized the decoherence behavior induced by phonon noise for In(Ga)As QDs in PCWs. We found that ZPL broadening induced by phonon scattering comprises a quadratic and linear coupling. At a temperature below 10K, the long-wavelength vibration due to the nano-device is the predominant dephasing mechanism, which leads to ZPL broadening with linear proportionality. Above 10K, virtual phonon transitions in QD is the dominant dephasing process. The

RT line width measurements indicate that the phonon impact on the broadening of the linewidth is consistent with the impact on TPI.

Chapter 6

Propagation Loss in Gated GaAs Nanophtonic Waveguides

Study of the electric field induced optical absorption in gated GaAs nanophotonic waveguides as function of the electric field, wavelength and temperature.

As presented in chapter 4, GaAs membranes with embedded self-assembled Ga(In)As QDs provide a mature platform to couple single quantum emitters with planar photonic nano-devices for generating high performance single photons sources. Such sources greatly benefit from the electric contacts, not only enabling to Stark tune the emission wavelength, but also allowing to suppress the decoherence caused by charge noise. However, implementing the metal gates introduces additional absorption due to free-carrier absorption and the Franz-Keldysh effect (FKE) [104]. The optical absorption is a fundamental challenge for scaling up the photonic integrated circuits towards on-chip quantum information processing. Therefore, a detailed characterization of the optical losses in such a system has been carried out to quantify the various losses and to identify their origin, and how to further minimize them. Most of the data presented here has been published in [105].

6.1 Propagation loss mechanisms

Several loss mechanisms are typically observed in waveguides. Scattering loss caused by the waveguide roughness is typically independent of the applied electric field and, at least within the emission range of QDs, of wavelength and temperature. In GaAs devices, a large discrepancy between the theoretical and fabricated photonic nano-devices is usually observed due to roughness. Additionally, unpassivated surfaces lead

to additional loss due to the presence of defect states, leading to absorption below the gap. Surface passivation has been successfully employed to improve the surface quality and thus reduce the optical loss [71, 95].

In doped waveguides, additional losses arise due to free-carrier absorption in the doped regions and an electric-field induced loss (electroabsorption) due to the FKE.

Theoretical description of the Franz-Keldysh effect

The FKE in gated waveguides originates from the built-in electric fields across the p-i-n junctions. The wavefunctions of the electron and holes distort when applying a static electric field through semiconductor junction, thereby enabling the absorption of photons possessing energy lower than bandgap. Assuming the electric field F is oriented along the z direction, the Schrödinger's equation for an electron in a semiconductor potential V_c reads

$$[\frac{p^2}{2m_0} + V_{\mathrm{c}}(r) - eF(z)]\psi(r) = E\psi(r), \tag{6.1}$$

Expanding the wavefunction $\psi(r)$ in terms of Bloch functions $|nk\rangle = u_{n,k}e^{ik\cdot r}$

$$\psi(r) = \sum_{\mathrm{n,k}} \alpha_n(k)\,|nk\rangle\,, \tag{6.2}$$

and projecting it on the basis function $|NK\rangle$ allows us to derive the Schrödinger's equation for the coefficients $\alpha_{\mathrm{N}}(k)$ as

$$-ieF\frac{\partial\alpha_{\mathrm{N}}(k)}{\partial K_{\mathrm{z}}} - eF\sum_{n} z_{\mathrm{Nn}}(K)\alpha_{\mathrm{n}}(K) = (E - \varepsilon_{\mathrm{N}}(K))\alpha_{\mathrm{N}}(k). \tag{6.3}$$

Here $\varepsilon_{\mathrm{N}}(K)$ is the permittivity and $z_{\mathrm{Nn}}(K) = \langle NK|\, z\,|nk\rangle$ is the field-induced transition element. Using a perturbative approach, equation 6.3, can be solved leading to a close expression for the wavefunctions [106]. The absorption is given by transition rates between the solutions at the conduction and valence band, leading to

$$\alpha(\hbar\omega, F) = \alpha_{\mathrm{b}}\beta^{1/2}\pi[Ai'^2(-\zeta) + \zeta Ai^2(-\zeta)], \tag{6.4}$$

where the β $((\frac{2m_{\mathrm{r}}}{\hbar^2e^2F^2})^{-1/3}$)is the FK characteristic energy, ζ $(\frac{\hbar\omega - E_{\mathrm{g}}}{\beta})$ is the dimension variable and Ai is the Airy function, which is the electron and hole wavefunction in the presence of a static field.

Model of FKE in gated GaAs nanophotonic waveguides

The devices used in this work are single-mode rectangular waveguides fabricated on GaAs membranes. Fig. 6.1 a) layouts the layer structure of the membrane while Fig. 6.1 b) shows the transverse electric (TE) mode profile confined in the rectangular waveguide with a width of 300 nm and height of 180 nm.

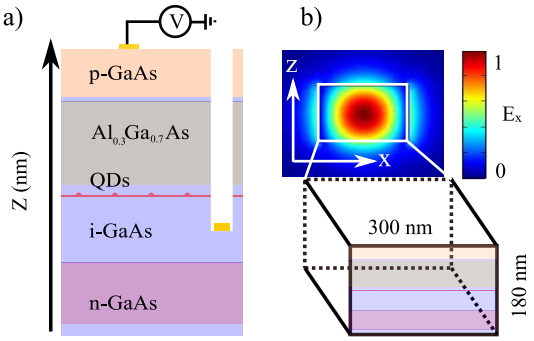

Figure 6.1: Sketch of the devices employed for the loss characterization [105]. a) The layout of the wafer layer structure along the growth direction z. b) Finite element simulation of the transverse electric (TE) mode profile and the corresponding waveguide cross-section.

A one-dimensional Poisson equation solver [107] is used to simulate the band diagram of this *p-i-n* heterostructure without applying external voltage. The results are shown in Fig. 6.2 a). The solid lines show the conduction and valance band profile in the case that the Ohmic contacts to the p-doped and n-doped layers are perfect. However, in a realistic case, the waveguide surfaces have been inevitably oxidized during sample processing, leading to plenty of defects whose energy level is within the GaAs bandgap. As a result, the surface charge density is increased due to the population of these mid-gap states. The surface defects 'pin' the Fermi-level inside the bandgap and thus bend the conduction and valance band in the proximity of the surface [108] as shown in Fig. 6.2 a) by dashed lines. The pinned Fermi-level above the conduction band is estimated using a Schottky boundary condition with a barrier height of 1 eV on both sides of the p-i-n diode. Assuming a density of the surface states ($\sim 10^{13}$ cm^{-2}) [109], the corresponding Fermi-level pinning occurs ~ 0.5 eV above the valence band [110].

The corresponding electric field is displayed in Fig. 6.1 a) right axis. The electric field across the intrinsic region is calculated using $F = (V_{\mathrm{BI}} - V)/d$, where V_{BI} is the built-in voltage of the diode junction and d is the total length of the depletion and intrinsic layers. The electric field on the surfaces are determined by Fermi-level pinning, which is over 1 MV/cm at top surface. Such a large electric field can contribute significantly to the absorption owing to the FKE. The surface electric field is independent of the external applied voltage, allowing us to separate the electro-absorption produced by the band bending from the bulk absorption.

According to equation 6.4 and the given electric field calculated and plotted in Fig. 6.2 a), the (bulk) Franz-Keldysh absorption $\alpha_{FK}(\lambda, F)$ can be estimated as a function of electric field F and wavelength λ. Fig. 6.2 b) illustrates a simple electro-absorption profile as a function of the wafer growth direction z. The electro-absorption in the $Al_{0.3}GaAs_{0.7}As$ region is neglected, since the bandgap is blue-shifted to 1.77 eV. Here we spatially separate the electro-absorption in two distinct regions: (1) the intrinsic

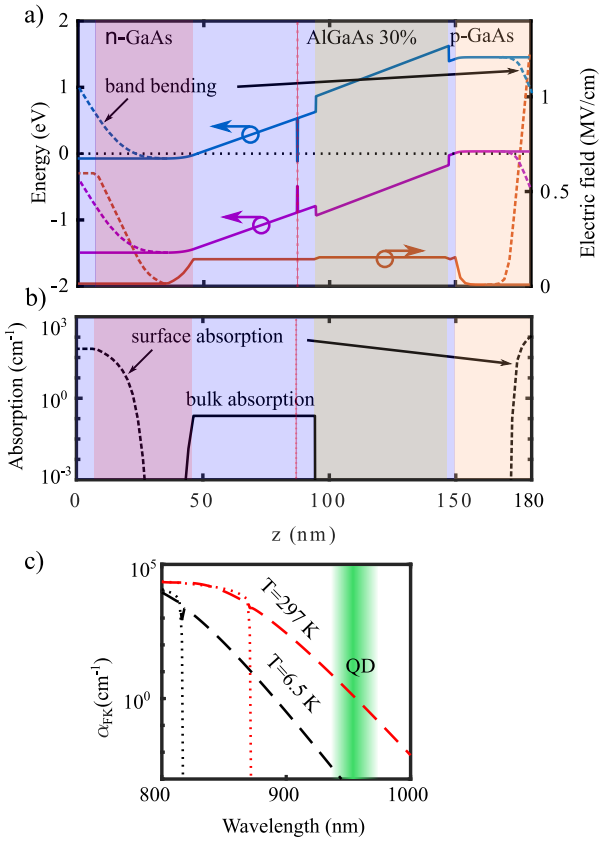

Figure 6.2: Electroabsorption in GaAs nanophotonic waveguides [105]. a) Band structure diagram at equilibrium without applying external voltage bias. The blue (purple) solid line denotes the conduction (valence) band, and the black dotted line is the Fermi level. The built-in electric field is plotted on the right axis in red solid line. Dashed lines display the band-bending at the doped-layer due to Fermi-level pinning. b) Electroabsorption is calculated from the electric field in a) at a wavelength of 930 nm at T=6.5 K. c) Bulk electroabsorption as a function of wavelength for room and cryogenic temperature. The dashed (dotted) line represents the absorption at en electric field of F=100kV/cm (F=0). And the green region illustrates the typical emission range of the In(Ga)As QDs.

region inside the p-i-n diode, where the absorption is dependent on the external applied voltage (solid line in Fig. 6.2 b), (2) The surface regions, where the absorption is only relevant to surface electric field created by the Fermi-level pinning and does not depend on the external electric field (dashed lines). So the total optical loss in the waveguide is written as

$$\alpha(\lambda, F) = \alpha_{\mathrm{R}}(\lambda) + \Gamma_{\mathrm{b}}\alpha_{\mathrm{FK}}(\lambda, F), \tag{6.5}$$

where $\alpha_R(\lambda)$ is the residual absorption without the voltage dependent FKE and Γ_b is the mode confinement factor for the intrinsic GaAs region, given by the overlap integral [111]

$$\Gamma_b = \frac{c}{2n} \frac{\int_{\mathrm{b}} \varepsilon(x,z) |\overrightarrow{E}(x,z)|^2 dxdz}{\int \left\langle S_{\mathrm{y}}(x,z) \right\rangle dxdz}. \tag{6.6}$$

In the above equation, $\varepsilon(x,z)$ is the spatial distribution of the permittivity. $\overrightarrow{E}(x,z)$ and $\left\langle S_{\mathrm{y}}(x,z) \right\rangle$ are the simulated two-dimensional profiles of the electric field optical mode (Fig. 6.1b)) and the average Poynting vector component in the waveguide propagation direction, respectively. The subscript 'b' indicates that the integral is taken in the bulk GaAs layer in the waveguide.

Figure 6.1 c) shows the profiles of $\alpha_{\mathrm{FK}}(\lambda, F)$ as function of wavelength λ and electric field F separately based on the experimental model [112]. This model has been validated at room temperature in bulk GaAs. Here, we assume that a change in temperature only influences the bandgap of GaAs, shifting it from 1.44 eV at room temperature to 1.52 eV at cryogenic temperature of 6.5 K. Obviously, the cryogenic temperature lowers the absorption.

The QDs emission range is pictured in green in Fig. 6.1 c). When the electric field is F=0 (dotted line), no electro-absorption is expected at energies below the bandgap for direct-gap un-doped semiconductors, while for F=100 kV/cm, the FKE becomes pronounced in the QDs emission range. In this model, the absorption induced by QDs is neglected because the density of QDs in the our sample is quite low , thus the QDs absorption is not observable since other absorption mechanisms are dominant. Further, the quantum-confined Stark effect can been neglected as well in our data analysis. Chapter 4 indicates the spectral tuning by the Stark tuning is lower than 1 meV/V, while the QDs' inhomogeneous broadening is 30-50 meV, which is much lager than the Stark tuning.

6.2 Propagation loss characterization

A series of rectangular waveguides with various lengths are prepared (following the fabrication procedure presented in chapter 2) to measure the optical loss per unit length in GaAs nanophotonic waveguides. Fig. 6.3 a) shows the top-view SEM image of the processed sample. The p-type electrode, highlighted in yellow, is employed to apply an external voltage to the p-i-n diode in the GaAs membranes.

A pair of shallow etched gratings (SEG) are designed to couple light in and out of the waveguides and cross-polarized with the purpose of avoiding collecting any scattered light from the excitation port. The SEGs are spaced at a fixed distance from one to another aiming to avoid re-aligning the angle and position of the excitation and collection of light. Our optimized sample processing recipe enables to produce devices with high precision, which in turn ensure the transmission spectrum is highly reproducible as demonstrated in Chapter 2.

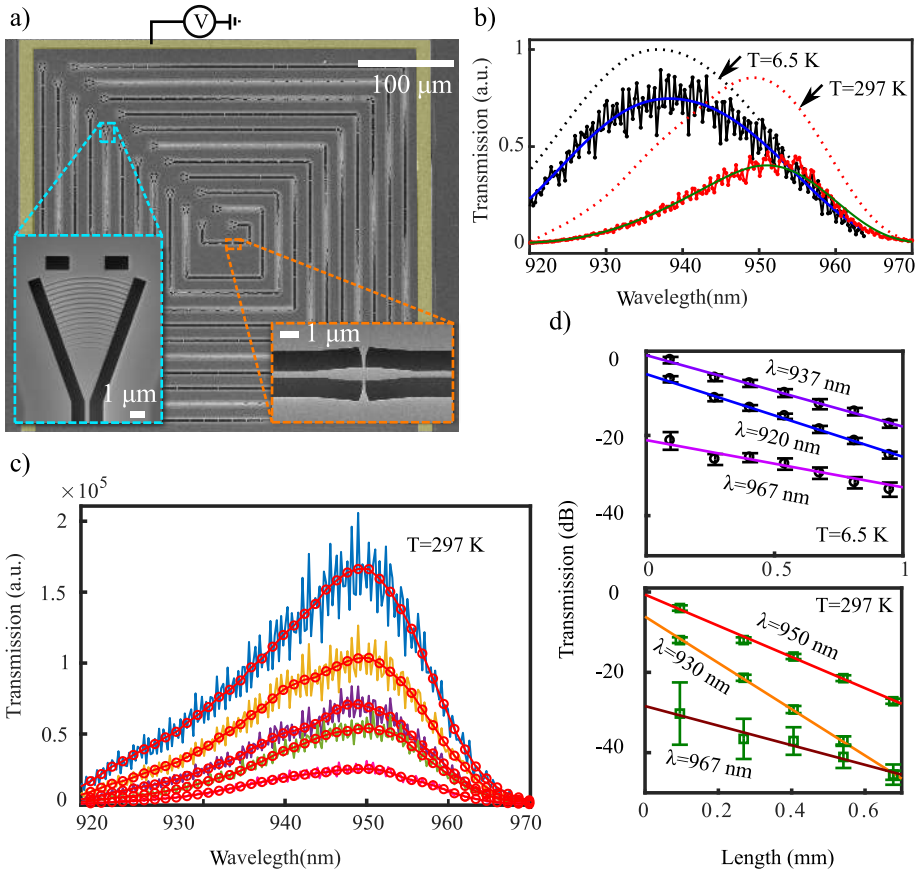

Figure 6.3: Propagation loss measurement in gated nanophotonic waveguides [105]. a) SEM image of the suspended concentric waveguides, the details of the supporting tethers and shallow etched gratings (SEG) are displayed in the inset. b) The transmission spectra of the shortest waveguide in a) with a length of L=95 μm at room temperature (red dots connected by solid lines) and 6.5 K (black dots connected by solid lines) without applying external voltage. The solid lines are the smoothed data, the dot lines are the gratings transmission profiles. c) The transmission profiles of series of waveguides with different lengths. The red solid lines are the smoothed data. d) Transmission (in dB) normalized to the peak transmission of the grating at cryogenic temperature (top) and room temperature (bottom) as a function of the waveguides' length. The solid lines are the linear fits where the slopes provide the loss per unit length.

The tethers shown in Fig. 6.3 a) inset are used to support the suspend waveguides in the air. The insertion loss due to the tethers are negligible since varying the number of tethers per unit length does not influence the transmission [113]. In addition, all waveguides are designed with identical terminating SEGs as well as the same number of 90-degree bends, which allows factoring out the loss caused by the SEGs and bends. This approach ensures the propagation loss is only as a function of waveguides length.

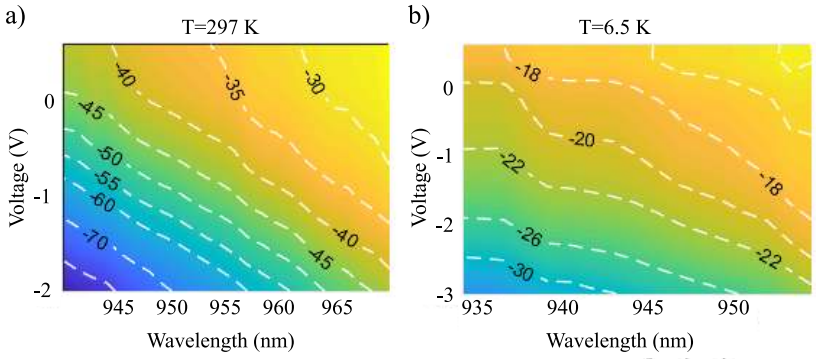

Figure 6.4: Color maps of external applied voltages and wavelengths dependency of absorption at room temperature a) and b)cryogenic temperature T=6.35 K respectively. The dot lines are the contours with the corresponding loss per unit length.

The sample is characterized in a closed-cycle cryostat and a supercontinuum laser (super K) is employed to carry out the transmission measurement. Fig. 6.3 b) shows the transmission spectra of the shortest concentric waveguide at room temperature and cryogenic temperature without applying external voltage. Compared to cryogenic temperature, a visible drop of the transmission at room temperature is observed, due to the larger absorption caused by the built-in electric field. The SEG transmission peak is red-shifted by 15 nm at room temperature due to the thermo-optic effect. The small fringes appearing in the transmission curves are probably caused by the reflectivity of SEGs. To provide a better comparison , a smooth filter is applied to extract the maximum transmission, and plotted as a function of wavelength. The magnitude of the fringes is used as an error bar for the transmission data. The waveguides transmission is gradually attenuated as a function of length as shown in Fig. 6.3 c). The total transmission is given by

$$T(L) = T_{\mathrm{B}}^{3} T_{G}^{2} e^{-\alpha L}, \tag{6.7}$$

where T_{B} is the transmission of a 90° bend, which, from numerical simulations, causes <0.005 dB loss in the wavelength range studied here for a waveguide length of ~ 7 μm, and can therefore be neglected. T_{G} is the transmission of a single SEG. The coefficient α is the loss per unit length obtained by linearly fitting the logarithmic transmission according to

$$log(T(L)) = 2log(T_{\mathrm{G}}) - \alpha L, \tag{6.8}$$

T_{G} is derived from the intercept of the transmission profile with the ordinate where the length of the waveguide is zero, and its response as a function of wavelength is shown in Fig. 6.3 b) (dotted lines).

The transmission in dB is linearly dependent on the waveguides' length within the error bar shown in Fig. 6.3 d), allowing to extract the loss per unit length over the

response bandwidth of SEGs. At room temperature T=297 K, α is (39 ±3) dB/mm for the peak transmission wavelength of λ=950 nm, while it reduces to (17±1) dB/mm (at λ=937 nm) at cryogenic temperature. For both temperatures the loss is larger at short wavelengths as predicted by the FKE model.

The electric field dependency of the FKE is quite remarkable as well. A voltage scan from -4 V to 0.6 V in steps 0.4 V is carried out at both room temperature and cryogenic temperature. The loss per unit length is mapped out as a function of external applied bias and wavelength as shown in Fig. 6.4. For both temperatures, the absorption increases significantly at shorter wavelengths and for an increasing reverse bias. Interestingly, a wavelength dependency of absorption is observed in forward bias, i.e. close to the flat-band condition, where the electro-absorption due to FKE is supposed to be strongly suppressed. We attribute this phenomenon to the surface electric field caused by the Fermi-level pinning and band bending, which can not be removed by applying an external voltage.

6.3 Residual loss modeling

To distinguish the various contributions to loss in the doped nanophotonic waveguides, we fit the full surface of the Fig. 6.4 using a non-linear least squares methods with the model of equation 6.5 as shown in Fig. 6.5 a). At cryogenic temperature T=6.5 k, the waveguide loss α as a function of wavelength fit within the error bars.

The fitting parameters are the residual loss α_R which remains after compensating the built-in voltage, and the confinement factor of the intrinsic region Γ_b. Fig. 6.5 b) shows the propagation loss measured on an un-doped wafer with identical waveguides geometry (blue line), which is wavelength independent. The residual loss α_R obtained on this gated nanophotonic waveguides shows instead a strong wavelength dependency, suggesting that an additional FKE exists in this doped waveguides most likely because of the surface electric fields created by the Fermi-level pinning.

In order to confirm this, we fit the residual loss as a function of wavelength by the FKE model,

$$\alpha_R(\lambda) = \alpha_0 + \Gamma_s \alpha_{FK}(\lambda, F_s). \tag{6.9}$$

Here F_s is the average surface electric field obtained by simulation shown in Fig. 6.2 b)(dash line). The room temperature and cryogenicΓ_s data are fitted and shown in Fig. 6.5 c). The confinement factor Γ_s and α_0 are extracted from the fitting. The fitting parameters of Fig. 6.5 a) and c) and finite-element simulation values are summarized in table 6.3.

	T=297 K	T=6.5 K	Simulation
Γ_b	±7)%	(51±7)%	52%
Γ_s	(6.6±0.5)%	(6.3±0.5)%	4%
α_0	(10.4±0.9) dB/mm	(10.9±1) dB/mm	
α_{FC}	~ 4 dB/mm (estimated)		
α_{INT}	~ 7 dB/mm (measured)		5–8 dB/mm

Table 6.3 is a summary of extracted fitting parameters from equation 6.5 and equation 6.9, relevant simulation and experimental values. As expected, a constant loss of $\alpha_0 = (11 \pm 2)$ dB/mm is extracted from both room temperature and cryogenic temperature fitting, suggesting this loss is temperature independent. According to the absorption coefficient for *n*-type and *p*-type GaAs provided in [114] and the confinement factor, a free-carrier absorption $\alpha_{FC} \sim 4$ dB/mm is estimated. The remaining absorption mainly results from the scattering caused by the sidewall roughness, which has been measured in an un-doped wafer with identical waveguides geometry resulting in $\alpha_{INT} \sim 7$ dB/mm.

High resolution SEM images taken from the sidewalls of our waveguides are used to estimate root-mean square roughness (RMS), which is in the range of 3-4 nm. Roughness can cause unwanted coupling between the fundamental modes and the radiation modes based on the waveguide scattering theory [115], which is stronger in high contrast waveguide.

6.4 How to minimize the absorption

The p-doped layer is the main contribution to the free-carrier absorption. Luckily, it is only needed in the emitter region. Thereby, we can selectively remove the p-layer from the surface, suppressing free carrier absorption as well as FKE due to the built-in electric field in the passive waveguide regions.

To remove the surface electric fields, it is necessary to unpin the Fermi-level. Several works have reported that de-oxidation followed by surface passivation can greatly reduce the surface states, thus greatly enhancing the quality factor of various systems like micro-resonator [116], photonic crystal micro-cavities [71], Gaussian cavities [95] etc. Adding surface passivation and other strategies like hard mask etching [117] and resist reflow [118] can reduce the waveguides RMS lower than 1 nm, and thus potentially reduce the $\alpha_{INT} < 1$ dB/mm.

* * *

In this chapter, a complete characterization of propagation loss in gated GaAs nanophotonic waveguides as a function of wavelength, electric field, and temperature has been reported. A detailed analysis attributes the main origin of loss to electro-absorption and free-carrier absorption. Such a loss can be neglected for devices with a footprint < 100 μm. However, when scaling up, it is necessary to reduce the loss further.

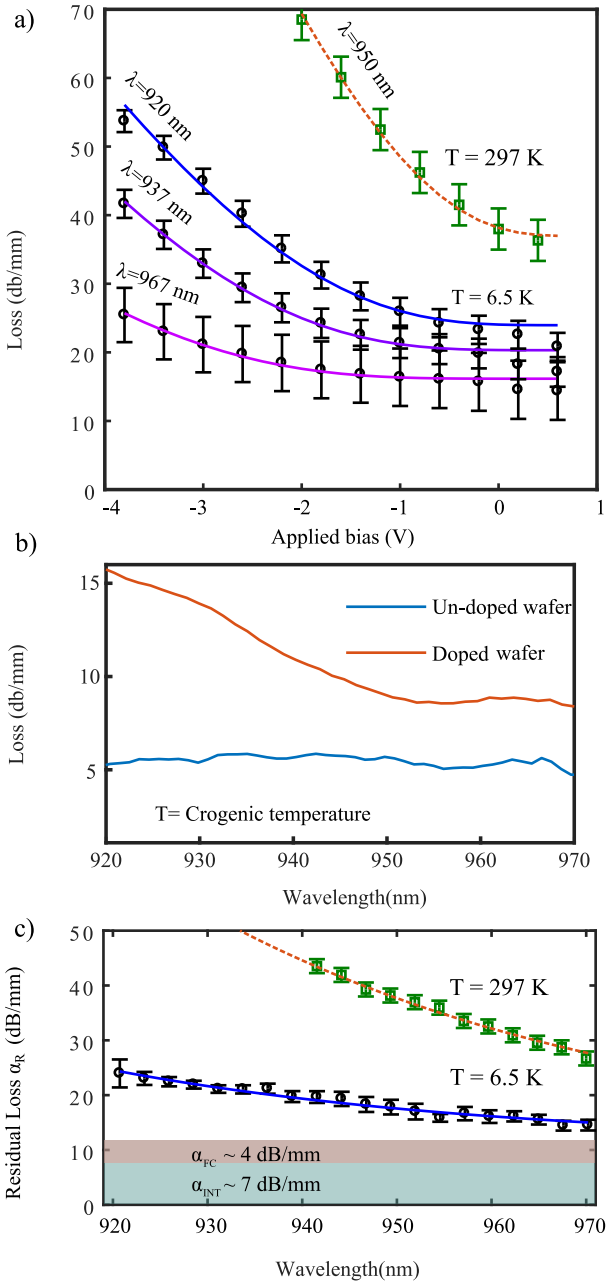

Figure 6.5: Voltage and wavelength dependency of the FKE [105]. a) Propagation loss as a function of the external applied voltage at room temperature and cryogenic temperature. The three bottom solid lines are the fits of the loss for different wavelengths (black circles) at T=6.5 K. The loss (green squares) and fit (red dash line) at room temperature is given for comparison. b) The loss measured on un-doped nanophotonic waveguides vs doped nanophotonic waveguides with external applied voltage V=0.6 V at cryogenic temperature. c) Residual loss extrapolated from the fits in a) as a function of wavelength. The room temperature (green squares) and cryogenic temperature (black circles) data are fitted using an electro-absorption model with a fixed surface electric field. The remaining loss contribution including free-carrier absorption and intrinsic absorption are indicated in shaded areas.

CHAPTER 7

Conclusions and Outlook

Several devices like single photon sources, photon routers, and filters, have been developed in the GaAs platform with integrated quantum emitters, pushing us towards the on-chip integration of multiple functionality for a scalable photonic quantum technology.

7.1 Summary

This project set out to investigate scalable circuits developed on the GaAs material platform with embedded quantum dots. To this end, a new generation of 'local' gated nano-structures have been realized. These gates exhibit outstanding advantages regrading yields, response speed and scalability. A comprehensive optical characterization was carried out for assessing and understanding the self-assembled QDs-based GaAs platform. In summary, the project has shown that

1. Near-ideal SPSs have been realized in planar nanostructures. A deterministic SPS with near-unity indistinguishability of (97 ±0.89) %, purity of (98.3 ±0.1) %, and improved efficiency of 8.4 % has been developed in a QD coupled to single-sided photonic crystal waveguide. Based on these results, a plug-and-play SPS has been realized in a dual-mode waveguide [69]. Apart from possessing the excellent properties of high indistinguishability and purity, on-chip mode-filtering of the laser background allows one to operate the device for long times without losing alignment. Moreover, it offers the potential to produce scalable SPS by parallelly exciting multiple QDs by one pulse.

2. Decoherence processes have been investigated. Indistinguishability is used to probe the decoherence of SPS. Benefiting from the high-quality material and metal gates, the charge noise and spin noise are suppressed to a large extent. The decoherence thereby is dominated by phonon noise, which is dependent on the surrounding nanostructure. Here, we investigated for the first time the phonon behavior on the 2D nanostructure of photonic crystal waveguide. We found that below 10 K, the ZPL is induced by linear phonon coupling due to long-wavelength vibration created by the finite size of the nanostructure. Above 10 K, a remarkable decrease of indistinguishability is observed because the thermal energy is large enough to achieve quadratic phonon coupling, causing virtual transitions in QD. Additionally, the linewidth broadening measured by resonant transmission vs. temperature shows a behavior consistent with the photon indistinguishability.

3. Optical losses have been characterized. Optical propagation loss undermines the SPS efficiency. A detailed loss characterization depending on temperature, wavelength, and external electric field, has been carried out. An important source of loss stems from the electric field in *p-i-n* junctions due to Franz-Keldish effect (FKE). Additionally, we found evidence of an additional surface electric field due to Fermi-level pinning at the waveguide surface, which contributes to an absorption over 20 dB/mm at room temperature. The optical loss is negligible for the devices with a footprint < 100 μm, however, when scaling up, it will be necessary to reduce the loss.

7.2 Outlook

7.2.1 Why on-chip integration is promising

As motivated in chapter 1.1.2, an ambitious goal for photonic quantum technologies is to perform information processing in a single chip instead of free-space. To date, the key building blocks in such a photonic architecture, consisting of generation, linear(non-linear) processing, and detection of quantum state light, have been demonstrated on solid-state platforms using various materials. Developing a single platform to implement all these functionalities is challenging and ambitious, but the benefit in terms of efficiency is also great. In the following, we outline the future challenges towards integrating multiple devices in a GaAs platform.

7.2.2 Integrated devices developed in the GaAs platform

Figure 7.1 shows an example of integration of a single-photon source based on dual-mode waveguides with a nanomechanical beam-splitter [113]. The local gates enable isolating each device electrically without introducing optical loss. However, there are still outstanding challenges in building a fully scalable platform. A basic requirement for integrated circuits is that there is no-cross talk between every single building. We should therefore implement additional insulation components for the metal wires of the different building blocks, especially when working with doped wafers. Moreover,

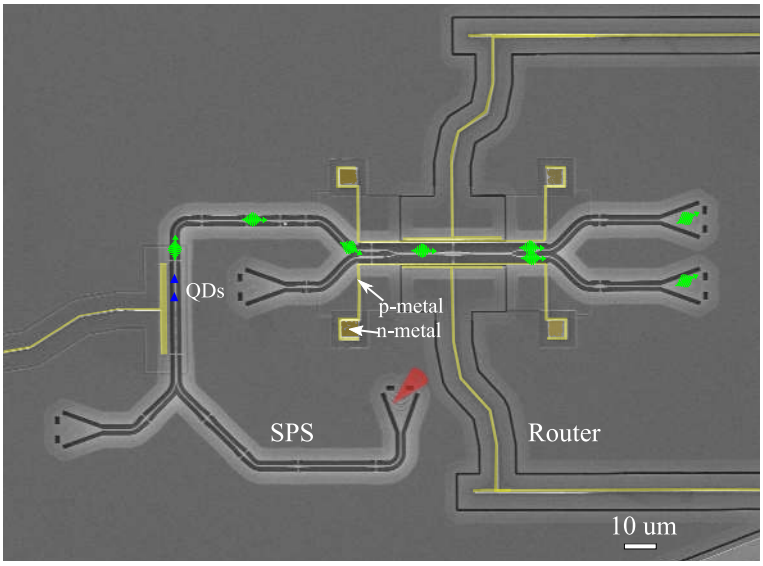

Figure 7.1: SEM image of integrating an SPS device with a single-photon router on GaAs membrane with embedded QDs.

as mentioned in chapter 2.3.3, there is a long-standing problem with dealing with residues produced during the ICP-RIE process, which cause unwanted loss and makes the fabrication of nanomechanical routers (as the one shown in Fig. 7.1) more complex.

Finally, it should be noted that while the local gates provide novel methods to build electrical interconnects between the various elements, the existing interconnects are not suitable for scaling up. Methods for wire-to-wire and wire-to-waveguide crossing need to be developed in order to address the scalability issues. Such methods may require new fabrication techniques (for example including polymers) but also more advanced design software to handle the complexity of electrical and optical routing.

In conclusion, to perform a practical quantum photonic technology, a higher level of scalability is required. This thesis has demonstrated that individual SPS with high quality can be built but the nature of high propagation loss in GaAs membrane limits the scalability.

To this end, the heterogeneous integration of GaAs with low loss material, such as SiN, is a promising approach. In the future, pioneering fabrication techniques for heterogeneous integration of multiple materials, may enable interfacing the various building blocks in a coherent and efficient manner. Therefore, the on-chip integration is expected to play a key role in the coming years, for the development of photonic quantum technologies.

Appendix

APPENDIX A

A.1 Layer structure of the wafer

Material Thickness (nm)	Doping (cm^{-3})	
GaAs	25	p=1e19
GaAs	5	p=1e18
GaAs	3	intrinsic
$Al_{0.3}Ga_{0.7}As$	52.8	intrinsic
GaAs	7.2	intrinsic
AlAs	0.3	intrinsic
InAs QDs		
GaAs	41	intrinsic
GaAs	38.5	n=2e18
GaAs	7.5	intrinsic
$Al_{0.75}Ga_{0.25}As$	1150	intrinsic
GaAs	100	intrinsic
GaAs/AlAs	20x(2.6/2.6)	intrinsic
GaAs	100	intrinsic
GaAs	substrate	Undoped

A.2 Optimized recipe for processing device

A.2.1 Recipe for depositing metal contact

Etch Mesa

1. Cleave a chip of ≈ 10 mm×10 mm from the wafer.
2. Clean the chip in sequence: immerse in Acetone for 2 minutes, transfer to Isopropanol (IPA) for 2 minutes, flush by IPA, blow dry by Nitrogen gas.

3. Dehydrate: bake at 185°C for 5 minutes on a hot plate.
4. Spin-coat ZEP 520A at 2100-2400 (rpm) for 1 minute and bake at 185°C for 5 minutes on a hot plate. The spin coating speed depends on how old the resist is once it is taken out of the fridge, and adjusting the spinning speed ensures the resist thickness ~ 550 nm. Generally the thickness should be reasonable if the resist looks green after baking.
5. Electron beam exposure and development: Exposure parameters (dose 210 μC/cm^2, current 10 nA, pitch 16), develop in room temperature N-Amylacetate for 70s and then rinse in IPA for 10s at room temperature, blow dry using N_2 and descum in O_2 plasma (100W, 45s).
6. RIE: Gas BCl_3 (5sccm)/Ar((10sccm)), Chamber pressure 10 m Torr, DC bias ~220 V, table temperature 15 °C. The target depth here is 110 nm which is 25 nm over the n-doped layer.
7. Strip the resit: soak in hot NMP at 70°C for 10 minutes, then transfer to room temperature NMP for 2 minutes and finally flush by IPA and blow dry by N_2.
8. Measure the etching depth by profilemeter.

Deposit n-type metal

1. Dehydrate: bake at 185°C for 5 minutes on a hot plate.
2. Spin-coat ZEP 520A at 2100-2400 (rpm) for 1 minute and bake at 185°C for 5 minutes on a hot plate.
3. Electron beam exposure and develop: dose 210 μC/cm^2, current 10 nA, pitch 16, develop in N-Amylacetate for 70s at room temperature and then rinse in IPA for 10s at room temperature, blow dry using N_2 and descum in O_2 plasma (100W, 1 minute).
4. De-oxidation: Soak in H_3PO_4:H_2O(1:5) for 2 minutes and then rinse in Milli-Q (MQ) water for 1 minute and blow dry by N_2.
5. Deposit Ni/Ge/Au/Ni/Au(4/40/60/27/150 nm) in electron beam evaporator.
6. Lift-off:Soak in hot NMP at 80°C for 5 minutes and then sonicate 1 minute (80 kHz,50%), return to hot NMP at 80°C for 5 minutes. Finally sonicate (80 kHz,50%) 1 minute and transfer to room temperature NMP and stay for 2 minutes, flush by IPA and N_2 blow dry.
7. Rapid thermal annealing at 420 °C for 40 s.

Deposit p-type metal

1. Dehydrate: bake at 185°C for 5 minutes on a hot plate.

2. Spin-coat ZEP 520A at 2100-2400 (rpm) for 1 minute and bake at 185°C for 5 minutes on a hot plate.

3. Electron beam exposure and develop: dose 210 μC/cm^2, current 10 nA, pitch 16, develop in N-Amylacetate for 70s at room temperature in a black box and then rinse in IPA for 10s at room temperature, blow dry using N_2 and descum in O_2 plasma (100W, 1 minute).

4. De-oxidation: Soak in H_3PO_4:H_2O(1:20) for 2 minutes and then rinse in Milli-Q (MQ) water for 1 minute and blow dry by N_2. This is operated in the dark.

5. Deposit Cr/Au(10/170 nm) in electron beam evaporator.

6. Lift-off:Soak in hot NMP at 80°C for 5 minutes and then sonicate 1 minute (80 kHz,50%), return to hot NMP at 80°C for 10 minutes. Finally sonicate (80 kHz,30%) 1 minute and transfer to room temperature NMP and stay 2 minutes, flush by IPA and N_2 blow dry.

A.2.2 Recipe for patterning nano - structures

Pattern shallow etched gratings and isolation trenches

1. Dehydrate: bake at 185°C for 5 minutes on a hot plate.

2. Spin-coat CSAR 9% at 4000 (rpm) for 1 minute and bake at 185°C for 1 minute on a hot plate. The resist thickness should be ~200 nm.

3. Electron beam exposure and development: Electron beam exposure parameters for shallow etching gratings (dose 350 μC/cm^2, current 1 nA, pitch 4), for isolation trenches (dose 350 μC/cm^2, current 10 nA, pitch 12). Develop in cold N-Amylacetate at -5 °C for 40 s and then rinse in cold IPA at -5 °C for 20 s, blow dry using N_2 and descum in O_2 plasma (100W, 45s).

4. RIE Etch: BCl_3 (5 sccm)/Ar (10 sccm), chamber pressure 10 m Torr, DC bias ~220 V, table temperature 15 °C. The target depth is 70- 80 nm.

5. Strip the resist :soak in hot NMP at 70°C for 10 minutes, then transfer to room temperature NMP for 2 minutes and finally flush by IPA and blow dry using N_2.

6. Measure the etching depth by profilemeter.

Deep-etch photonic crystals and waveguides

1. Dehydrate: bake at 185°C for 5 minutes on a hot plate.

2. Spin-coat ZEP 520A at 2100-2400 (rpm) for 1 minute and bake at 185°C for 5 minutes on a hot plate.

3. Electron beam exposure and development: electron beam exposure parameters of dose 350 $\mu C/cm^2$, current 1 nA, pitch 4, develop in cold N-Amylacetate at -5 ∘C for 60s and then rinse in cold IPA at -5 °Cfor 10s, blow dry using N_2 and descum in O_2 plasma (100W, 1 minute).

4. ICP etch: BCl_3(3 sccm)/Cl_2 (4 sccm)/Ar (25 sccm), Chamber pressure 4.7 m Torr, DC bias ≈ 300 V, ICP power 300 W, table temperature 0 °C.

5. Srip the resist :soak in hot NMP at 70°C for 10 minutes, then transfer to room temperature NMP for 2 minutes and finally flush by IPA and blow dry using N_2.

A.2.3 Recipe for releasing the membrane

1. HF etch: Place the sample placed in a small home-made plastic boat and place them in 5% HF for ~ 50 s, ensuring that the undercut of the waveguide is ~2.7 μm. Then transfer to MQ water for 10 minutes. Prepare 4 beakers of MQ water before starting the etching and move the sample in from one to another in order to progressively dilute the HF solution.

2. H_2O_2 clean: Dip sample in H_2O_2 for 1 minutes and transfer to MQ water and stay 10 minutes as the same as operated after the HF dip.

3. H_3PO_4 de-oxidation: Dip in H_3PO_4:H_2O(1:10) for 1 minute and transfer to MQ wafer as the same as after HF dip.

4. Dip the sample in IPA for 5 minutes. Prepare 3 beakers of IPA and move the sample one to another in order. Remove the boat at the first beaker.

5. Prepare the critical point drying (CPD) holder beforehand and move the sample into the holder.

6. CPD dry.

7. Measure the I-V curve with probe station.

8. Check the morphology of the devices by scanning electron microscopy (SEM).

A.3 Pre-characterization SPS

The characterization of the newly fabricated samples was initially carried out in the flow cryostat to determine the emission spectra, radiative decay rate, brightness, etc.

Single-mode rectangular waveguides with a width of 280 nm, shown in Fig. A.1 (a), terminated with mirrors to reflect the emitted photons to the collection direction, are used for characterization. A shallow etched grating (SEG) directs the photons to the collection optics. The QDs couple mainly to the fundamental transverse electric (TE) mode, whose electric field profile $E_x(x, z)$ is shown in Fig. A.1 (b) A pulsed laser (Mira) tuned to the above-band wavelength of 780 nm is shone on the top of the nanobeam

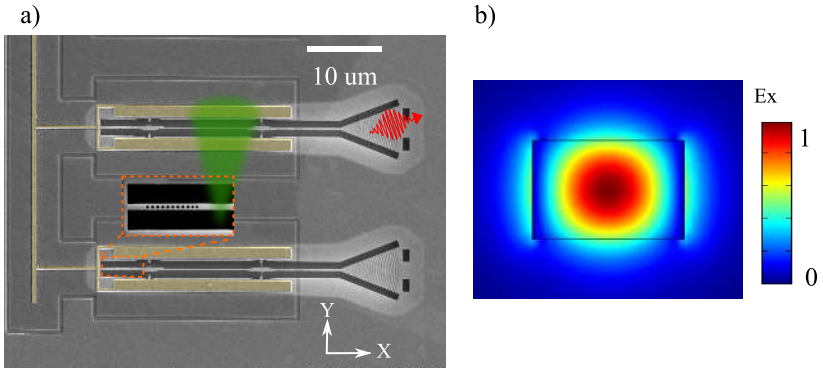

Figure A.1: Single photons are generated by QDs coupled to nanobeam waveguide a) SEM image of nanobeam waveguide with shallow etching grating, excitation, and collection are spatially separated. Inset shows the waveguide is terminated with mirrors on one side. b) Finite element method simulation of the transverse electric (TE) field mode profile of single-mode nanobeam waveguide.

waveguide to excite several QD transitions, while the voltage on the QD is scanned. The dot density in this wafer shows a linear gradient from the edge to the center in the [1-10] direction while it is almost constant in the [110] direction. The sample used in this work was taken approximately 1.8 cm from the edge of a 3-inch diameter wafer. We do see quite noticeable dot density variation in the [1-10] direction, as shown in Fig. A.2. Above-band photoluminescence indicates that the dot density is quite high and that the wavelength of emitted single photons mainly falls within the $930 - -950$ nm range, which matches well the SEG collection bandwidth. Most bright individual lines can be spectrally isolated, implying that even such high dot density is not problematic for resonant excitation for a single QD transition. The variation in line intensity is likely caused by the dot position in the waveguide. The mirror, in fact, produces a standing wave that spatially modulates the density of optical states. Comparing the various photoluminescence spectra of Fig. A.2 a), a clear spatial dependence of the density is observed when moving over just 380 mum in the y direction(Fig. A.2 c)). Subsequently, implementing p-shell excitation, Fig. A.3 a) shows the voltage tuning photoluminescence map. The corresponding spectra at voltage 1.24 V are shown in Fig. A.3 b), is fitted by a Voigt model (convolution of Gaussian and Lorentzian function) in-dash purple line. Fig. A.3 d), intensity dependency of input power was measured. Hereunder a π-pulse excitation, the spectrometer detected $\approx$ 20000 photons per second. Then radiative lifetime measurement of this dot and few dots from the nearby bulk was shown in Fig. A.3 c), the solid red line denotes the dot from the bulk, fitted by dash green line, and the average lifetime is $\sim$ 1.1 ns. The radiative decay rate curve of the dot from the waveguide is fitted by purple dash line, lifetime is $\sim 725ps$, with a moderate Purcell enhancement of $\sim$ 1.5.

To understand more about the dots' behavior, the HBT measurements are implemented. Firstly, the above-band laser excites the same dot characterized above, and

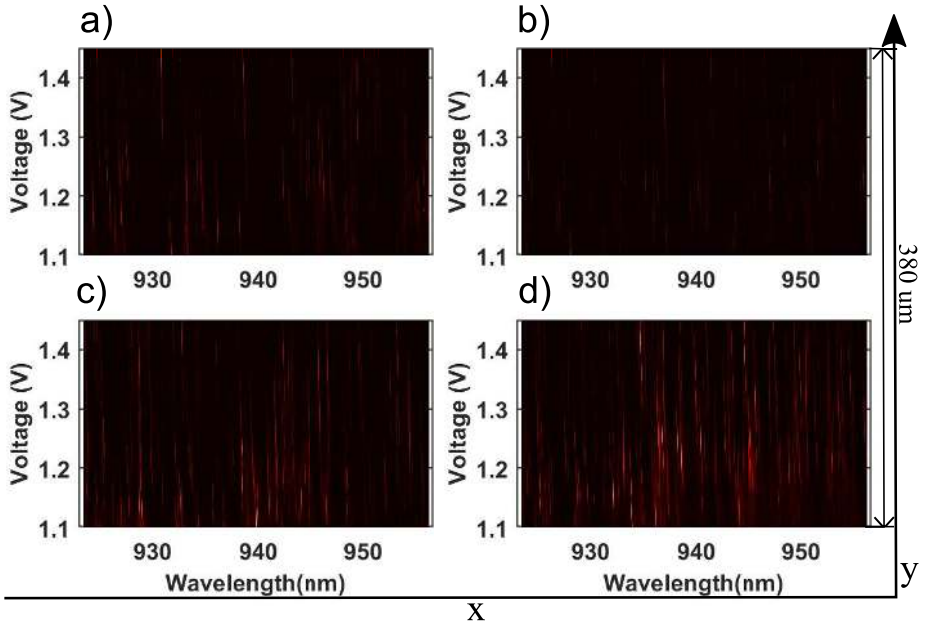

Figure A.2: Above-band excitation of devices on different locations estimates dots density and variation gradient. The sample took from a wafer where the dots' density gradient decreases in the Y direction while not change in the x-direction a), b) are single-mode waveguides with slightly different widths of 280 *nm* 300 *nm* respectively and distributed with a distance of 50 *um*. c,d) is the copy of a, b) with a spatial separation of 380 μm.

the grating filter is used to filter the laser background. The second-order correlations dependency of power are given in Fig. A.4. In the low power regime A.4 a), b), there is a tiny peak at zero time delay, $g^2(0)$ is not perfect probably because the grating filter bandwidth might be too large to completely suppress emission from other quantum dots. In a relatively high power excitation regime, there is a quite pronounced central peak shown in A.4 c), which is contributed by the nearby dots emission because the QDs density is quite high, and it can not avoid exciting multiple dots by one laser spot. In such a situation, it is necessary to employ resonant excitation. $g^2(0)$ of the single photons emitted from the dot is measured under p-shell excitation using a grating filter to excite fewer dots within the same excitation area as the aboveband illumination. As shown in Fig. A.5, the measured $g^2(0)$ is 0.0054 ± 0.0063, 0.0068 ± 0.0011, 0.0088 ± 0.00073, 0.01 ± 0.00052 respectively, for a corresponding power 2.5 of μw, 5 μw, 10 μw and 35 μw. The $g^2(0)$ slightly increases with increasing of the input power, which attributes to laser background leaks to the detection channel. The single photons purity can reach as high as 99.5 %.

The reduction of QDs geometry symmetry lifts the degeneracies among exciton states, which result in fine structure splitting been partly possible in spectroscopic

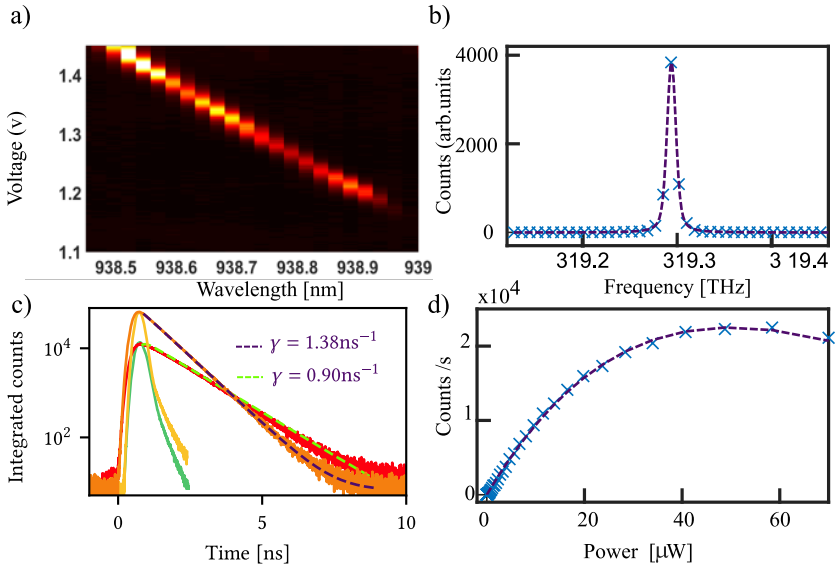

Figure A.3: Quasi-resonant excitation is performed. a) Frequency and voltage tuning of the neutral exciton. b) the Corresponding spectrum at V=1.235 V is fitted by the Voigt model. c) Radiative decay rate measurements of this dot and the one from nearby bulk excited by above-band laser by the setup shown in 4.2 c). The yellow solid curve and green solid curve are the instrument function (IRF) of the measurements done by Mira and PDL, respectively. The solid orange and red curve are fitted single exponentially convolved with the IRFd) Measured intensity dependency of the excitation power.

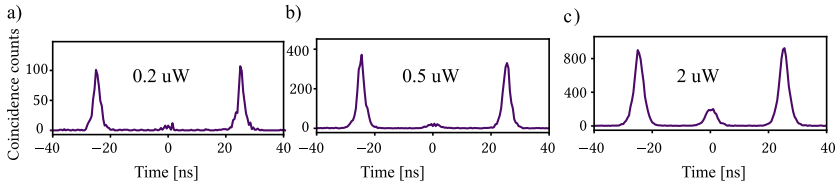

Figure A.4: The second-order correlation is measured under above-band excitation by HBT setup displayed 4.2 a). a), b), c) shows the correlation histogram at different powers.

experiments because of the magnitude of the energy involved, which considerably smaller than the inhomogeneous broadening. For the self-assembled In(Ga)As QDs, the reported fine structure in a frequency span of 0 to 10 GHz. With CW resonant excitation of some of the dots from different devices, most of these dots do not show the fine structure splitting in spectroscopy, while some are really pronounced as shown in Fig. A.6, fitted by Voigt model. For this, we can significantly enhance one dipole while suppress the other by polarization control.

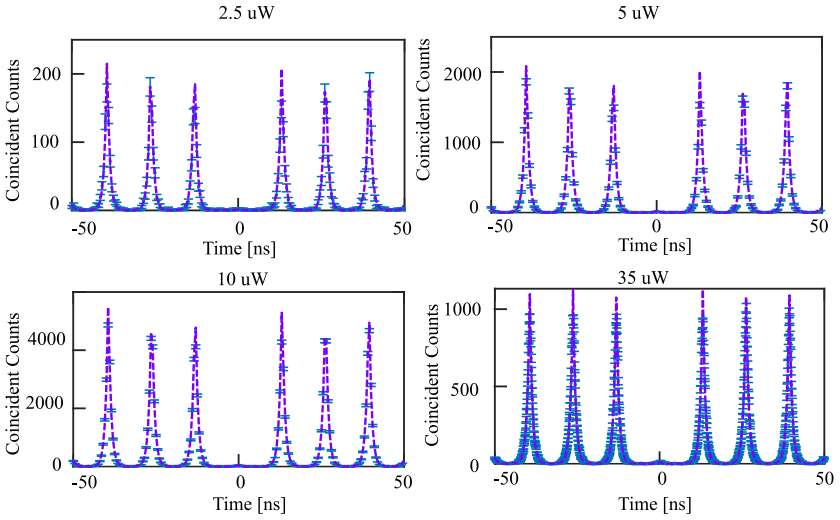

Figure A.5: HBT measurements of the single photons under p-shell excitation. a), b), c). d) gives the $g^{(2)}(0)$ at different powers.

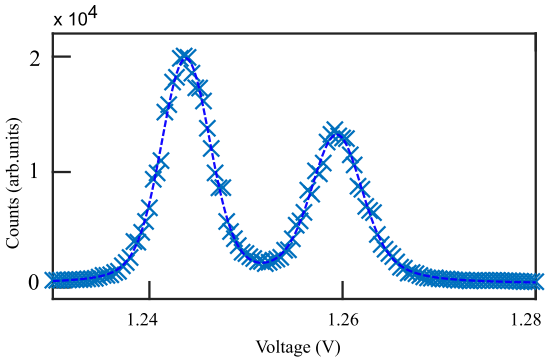

Figure A.6: CW-resonant excitation to investigate the fine structure splitting.

Bibliography

[1] David P. DiVincenzo. The physical implementation of quantum computation. *Fortschritte der Physik*, 48(9-11):771–783, 2000.

[2] Frank A. Bovey. *Nuclear magnetic resonance spectroscopy*. 1986.

[3] R. E. March. *Ion trap mass spectrometers*. Elsevier Ltd., 2016.

[4] Tyler Maxwell, Maria Gabriela Nogueira Campos, Stephen Smith, Mitsushita Doomra, Zon Thwin, and Swadeshmukul Santra. *Quantum dots*. Elsevier Inc., 2019.

[5] Adam M. Larson. Multiphoton microscopy. *Nature Photonics*, 1(5):169–176, 2011.

[6] Avijit Lahiri. *Quantum Optics*. Elsevier Inc., 2016.

[7] Gennady P. Berman, David K. Campbell, Gary D. Doolen, and Kirill E. Nagaev. Electron-nuclear spin dynamics in a mesoscopic solid-state quantum computer. *Microelectronic Engineering*, 47(1):277–279, 1999.

[8] Igor Aharonovich, Dirk Englund, and Milos Toth. Solid-state single-photon emitters. *Nature Photonics*, 10(10):631–641, 2016.

[9] Morten Kjaergaard, Mollie E. Schwartz, Jochen Braumüller, Philip Krantz, Joel I.J. Wang, Simon Gustavsson, and William D. Oliver. Superconducting Qubits: Current State of Play. *Annual Review of Condensed Matter Physics*, 11:369–395, 2020.

[10] Edbert J. Sie, Clara M. Nyby, C. D. Pemmaraju, Su Ji Park, Xiaozhe Shen, Jie Yang, Matthias C. Hoffmann, B. K. Ofori-Okai, Renkai Li, Alexander H. Reid, Stephen Weathersby, Ehren Mannebach, Nathan Finney, Daniel Rhodes, Daniel Chenet, Abhinandan Antony, Luis Balicas, James Hone, Thomas P. Devereaux, Tony F. Heinz, Xijie Wang, and Aaron M. Lindenberg. An ultrafast symmetry switch in a Weyl semimetal. *Nature*, 565(7737):61–66, 2019.

[11] David D. Awschalom, Lee C Bassett, Andrew S. Dzurak, Evelyn L. Hu, and Jason R. Petta. Quantum Spintronics: Engineering and Manipulating Atom-Like Spins in Semiconductors. 339(3):1174–1180, 2013.

[12] H. J. Kimble. The quantum internet. *Nature*, 453(7198):1023–1030, 2008.

[13] P Walther, K J Resch, T Rudolph, E Schenck, H Weinfurter, V Vedral, M Aspelmeyer, and A Zeilinger. Experimental one-way quantum computing. *Nature*, 434:169–176, 2005.

[14] Terry Rudolph. Why i am optimistic about the silicon-photonic route to quantum computing. *APL Photonics*, 2(030901):1–12, 2017.

[15] Anke Lohmann, Bernhard Schrenk, Gianluigi Casse, Christoph Marquardt, Eleni Diamanti, Emanuele Pelucchi, Georgios Fagas, Hannes Hübel, Hercules Avramopoulos, Klaus D. Jöns, Marco Romagnoli, Martin Schell, Michael J. Wale, Moritz Kleinert, Paolo Villoresi, Roberta Ramponi, Roberto Osellame, Segolene Olivier, and Valerio Pruneri. *Quantum PIC Position Paper (Draft)*. 2021.

[16] Erman Engin, Damien Bonneau, Chandra M. Natarajan, Alex S. Clark, M. G. Tanner, R. H. Hadfield, Sanders N. Dorenbos, Val Zwiller, Kazuya Ohira, Nobuo Suzuki, Haruhiko Yoshida, Norio Iizuka, Mizunori Ezaki, Jeremy L. O'Brien, and Mark G. Thompson. Photon pair generation in a silicon micro-ring resonator with reverse bias enhancement. *Optics Express*, 21(23):27826–27834, 2013.

[17] M. J. Collins, C. Xiong, I. H. Rey, T. D. Vo, J. He, S. Shahnia, C. Reardon, T. F. Krauss, M. J. Steel, A. S. Clark, and B. J. Eggleton. Integrated spatial multiplexing of heralded single-photon sources. *Nature Communications*, 4(5):1–7, 2013.

[18] Justin B. Spring, Paolo L. Mennea, Benjamin J. Metcalf, Peter C. Humphreys, James C. Gates, Helen L. Rogers, Christoph Söller, Brian J. Smith, W. Steven Kolthammer, Peter G. R. Smith, and Ian A. Walmsley. Chip-based array of near-identical, pure, heralded single-photon sources. *Optica*, 4(1):90–96, 2017.

[19] F. Kaneda and P. G. Kwiat. High-efficiency single-photon generation via large-scale active time multiplexing. 5(10):1–7.

[20] Yu Ming He, Yu He, Yu Jia Wei, Dian Wu, Mete Atatüre, Christian Schneider, Sven Höfling, Martin Kamp, Chao Yang Lu, and Jian Wei Pan. On-demand semiconductor single-photon source with near-unity indistinguishability. *Nature Nanotechnology*, 8(3):213–217, 2013.

[21] N. Somaschi, V. Giesz, L. De Santis, J. C. Loredo, M. P. Almeida, G. Hornecker, S. L. Portalupi, T. Grange, C. Antón, J. Demory, C. Gómez, I. Sagnes, N. D. Lanzillotti-Kimura, A. Lemaítre, A. Auffeves, A. G. White, L. Lanco, and P. Senellart. Near-optimal single-photon sources in the solid state. *Nature Photonics*, 10(5):340–345, 2016.

[22] Hui Wang, Z. C. Duan, Y. H. Li, Si Chen, J. P. Li, Y. M. He, M. C. Chen, Yu He, X. Ding, Cheng Zhi Peng, Christian Schneider, Martin Kamp, Sven Höfling, Chao Yang Lu, and Jian Wei Pan. Near-Transform-Limited Single Photons from an Efficient -State Quantum Emitter. *Physical Review Letters*, 116(21):1–6, 2016.

[23] Feng Liu, Alistair J. Brash, John O'Hara, Luis M.P.P. Martins, Catherine L. Phillips, Rikki J. Coles, Benjamin Royall, Edmund Clarke, Christopher Bentham, Nikola Prtljaga, Igor E. Itskevich, Luke R. Wilson, Maurice S. Skolnick, and A. Mark Fox. High Purcell factor generation of indistinguishable on-chip single photons. *Nature Nanotechnology*, 13(9):835–840, 2018.

[24] Hui Wang, Yu Ming He, T. H. Chung, Hai Hu, Ying Yu, Si Chen, Xing Ding, M. C. Chen, Jian Qin, Xiaoxia Yang, Run Ze Liu, Z. C. Duan, J. P. Li, S. Gerhardt, K. Winkler, J. Jurkat, Lin Jun Wang, Niels Gregersen, Yong Heng Huo, Qing Dai, Siyuan Yu, Sven Höfling, Chao Yang Lu, and Jian Wei Pan. Towards optimal single-photon sources from polarized microcavities. *Nature Photonics*, 13(11): 770–775, 2019.

[25] Ravitej Uppu, Freja T. Pedersen, Ying Wang, Cecilie T. Olesen, Camille Papon, Xiaoyan Zhou, Leonardo Midolo, Sven Scholz, Andreas D. Wieck, Arne Ludwig, and Peter Lodahl. Scalable integrated single-photon source. *Science Advances*, 6 (50):1–7, 2020.

[26] Natasha Tomm, Alisa Javadi, Nadia Olympia Antoniadis, Daniel Najer, Matthias Christian Löbl, Alexander Rolf Korsch, Rüdiger Schott, Sascha René Valentin, Andreas Dirk Wieck, Arne Ludwig, and Richard John Warburton.

[27] Francesco Lenzini, Ben Haylock, Juan C. Loredo, Raphael A. Abrahão, Nor A. Zakaria, Sachin Kasture, Isabelle Sagnes, Aristide Lemaitre, Hoang Phuong Phan, Dzung Viet Dao, Pascale Senellart, Marcelo P. Almeida, Andrew G. White, and Mirko Lobino. Active demultiplexing of single photons from a solid-state source. *Laser and Photonics Reviews*, 11(3):1600297–1–1600297–5, 2017.

[28] Anthony J. Bennett, Raj B. Patel, Joanna Skiba-Szymanska, Christine A. Nicoll, Ian Farrer, David A. Ritchie, and Andrew J. Shields. Giant Stark effect in the emission of single semiconductor quantum dots. *Applied Physics Letters*, 97(031104):1–4, 2010.

[29] Jiaxiang Zhang, Johannes S. Wildmann, Fei Ding, Rinaldo Trotta, Yongheng Huo, Eugenio Zallo, Daniel Huber, Armando Rastelli, and Oliver G. Schmidt. *Nature Communications*.

[30] Henri Thyrrestrup, Gabija Kiršanske, Hanna Le Jeannic, Tommaso Pregnolato, Liang Zhai, Laust Raahauge, Leonardo Midolo, Nir Rotenberg, Alisa Javadi, Rüdiger Schott, Andreas D. Wieck, Arne Ludwig, Matthias C. Löbl, Immo Söllner, Richard J. Warburton, and Peter Lodahl. Quantum Optics with Near-Lifetime-Limited Quantum-Dot Transitions in a Nanophotonic Waveguide. *Nano Letters*, 18(3):1801–1806, 2018.

[31] Jacques Carolan, Christopher Harrold, Chris Sparrow, Enrique Martín-López, Nicholas J. Russell, Joshua W. Silverstone, Peter J. Shadbolt, Nobuyuki Matsuda, Manabu Oguma, Mikitaka Itoh, Graham D. Marshall, Mark G. Thompson,

Jonathan C.F. Matthews, Toshikazu Hashimoto, Jeremy L. O'Brien, and Anthony Laing. Universal linear optics. *Science*, 349(6249):711–716, 2015.

[32] Jürgen Volz, Michael Scheucher, Christian Junge, and Arno Rauschenbeutel. Nonlinear π phase shift for single fibre-guided photons interacting with a single resonator-enhanced atom. *Nature Photonics*, 8(12):965–970, 2014.

[33] Robert H. Hadfield. Single-photon detectors for optical quantum information applications. *Nature Photonics*, 3(12):696–705, 2009.

[34] Di Zhu, Marco Colangelo, Changchen Chen, Boris A. Korzh, Franco N.C. Wong, Matthew D. Shaw, and Karl K. Berggren. Resolving photon numbers using a superconducting nanowire with impedance-matching taper. *Nano Letters*, 20(5): 3858–3863, 2020.

[35] Han Sen Zhong, Hui Wang, Yu Hao Deng, Ming Cheng Chen, Li Chao Peng, Yi Han Luo, Jian Qin, Dian Wu, Xing Ding, Yi Hu, Peng Hu, Xiao Yan Yang, Wei Jun Zhang, Hao Li, Yuxuan Li, Xiao Jiang, Lin Gan, Guangwen Yang, Lixing You, Zhen Wang, Li Li, Nai Le Liu, Chao Yang Lu, and Jian Wei Pan. Quantum computational advantage using photons. *Science*, 1463(12):1460–1463, 2020.

[36] Ravitej Uppu, Leonardo Midolo, Xiaoyan Zhou, Jacques Carolan, and Peter Lodahl. Single-photon quantum hardware: towards scalable photonic quantum technology with a quantum advantage. *arXiv:2103.01110v1*, pages 1–15, 2021.

[37] Marcelo Davanco, Jin Liu, Luca Sapienza, Chen Zhao Zhang, José Vinícius De Miranda Cardoso, Varun Verma, Richard Mirin, Sae Woo Nam, Liu Liu, and Kartik Srinivasan. Heterogeneous integration for on-chip quantum photonic circuits with single quantum dot devices. *Nature Communications*, 8(1):1–12, 2017.

[38] A. Osada, Y. Ota, R. Katsumi, M. Kakuda, S. Iwamoto, and Y. Arakawa. Strongly coupled single-quantum-dot-cavity system integrated on a CMOS-processed silicon photonic chip. *Physical Review Applied*, 11(024071):1–6, 2019.

[39] Faraz Najafi, Jacob Mower, Nicholas C. Harris, Francesco Bellei, Andrew Dane, Catherine Lee, Xiaolong Hu, Prashanta Kharel, Francesco Marsili, Solomon Assefa, Karl K. Berggren, and Dirk Englund. *Nature Communications*, (5873).

[40] H. Eisele, A. Lenz, R. Heitz, R. Timm, M. Dähne, Y. Temko, T. Suzuki, and K. Jacobi. Change of InAs/GaAs quantum dot shape and composition during capping. *Journal of Applied Physics*, 104(12):1–6, 2008.

[41] S. Huang, S. J. Kim, R. Levy, X. Q. Pan, and R. S. Goldman. Mechanisms of InAs/GaAs quantum dot formation during annealing of in islands. *Applied Physics Letters*, 103(132104):1–5, 2013.

[42] A. Di Carlo. Semiconductor nanostructures. *Physica Status Solidi (B) Basic Research*, 217(1):703–722, 2000.

[43] Charles Michael Santori. *Generation of nonclassical light using semiconductor quantum dots*. PhD thesis, Stanford University, 2003.

[44] D. Leonard, K. Pond, and P. M. Petroff. Critical layer thickness for self-assembled InAs islands on GaAs. *Physical Review B*, 50(16):11687–11692, 1994.

[45] Peter Lodahl, Sahand Mahmoodian, and Søren Stobbe. Interfacing single photons and single quantum dots with photonic nanostructures. *REVIEWS OF MODERN PHYSICS*, 87(2):347–400, 2015.

[46] Matthias C. Löbl, Sven Scholz, Immo Söllner, Julian Ritzmann, Thibaud Denneulin, András Kovács, Beata E. Kardynał, Andreas D. Wieck, Arne Ludwig, and Richard J. Warburton. Excitons in InGaAs quantum dots without electron wetting layer states. *Communications Physics*, 2(1):1–19, 2019.

[47] Y. Toda, O. Moriwaki, M. Nishioka, and Y. Arakawa. Efficient carrier relaxation mechanism in In Gaas/GaAs self-assembled quantum dots based on the existence of continuum states. *Physical Review Letters*, 82(20):4114–4117, 1999.

[48] B. Urbaszek, E. J. McGhee, M. Krüger, R. J. Warburton, K. Karrai, T. Amand, B. D. Gerardot, P. M. Petroff, and J. M. Garcia. Temperature-dependent linewidth of charged excitons in semiconductor quantum dots: Strongly broadened ground state transitions due to acoustic phonon scattering. *Physical Review B*, 69(3):1–6, 2004.

[49] S.M.Sze and Kwok.K.Ng. *Physics of Semiconductor Devices*. 1995.

[50] Andreas V Kuhlmann, Julien Houel, Arne Ludwig, Lukas Greuter, Dirk Reuter, Andreas D Wieck, Martino Poggio, and Richard J Warburton. Charge noise and spin noise in a semiconductor quantum device. *Nature Physics*, 9(9):570–575, 2013.

[51] K. Roszak, V. M. Axt, T. Kuhn, and P. Machnikowski. Exciton spin decay in quantum dots to bright and dark states. *Physical Review B*, 76(19):1–6, 2007.

[52] Yu Huai Liao, Juan I. Climente, and Shun Jen Cheng. Dominant channels of exciton spin relaxation in photoexcited self-assembled (In,Ga)As quantum dots. *Physical Review B*, 83(16):1–7, 2011.

[53] J. M. Smith, P. A. Dalgarno, R. J. Warburton, A. O. Govorov, K. Karrai, B. D. Gerardot, and P. M. Petroff. Voltage control of the spin dynamics of an exciton in a semiconductor quantum dot. *Physical Review Letters*, 94(19):1–4, 2005.

[54] Qin Wang, Søren Stobbe, and Peter Lodahl. Mapping the local density of optical states of a photonic crystal with single quantum dots. *Physical Review Letters*, 107(16):1–4, 2011.

[55] Pierre Meystre and Murray Sargent. *Elements of Quantum Optics* . 2007.

[56] Claude Cohen-Tannoudji and David Guéry-Odelin. *Resonance fluorescence.* 2011.

[57] Alisa Javadi, Sahand Mahmoodian, Immo Sollner, and Peter Lodahl. Numerical modelling of the coupling eciency of single quantum emitters in photonic-crystal waveguides. *Journal of the Optical Society of America B*, 35(3):514–522, 2017.

[58] Joshua N Winn Robert D. Meade John D.Joannopoulos, Steven G. Johnson. *Photonic Crysrals Molding the Flow of Light.* 2007.

[59] R. J. Young, R. M. Stevenson, A. J. Shields, P. Atkinson, K. Cooper, D. A. Ritchie, K. M. Groom, A. I. Tartakovskii, and M. S. Skolnick. Inversion of exciton level splitting in quantum dots. *Physical Review B*, 72(11):1–4, 2005.

[60] S. Hughes. Enhanced single-photon emission from quantum dots in photonic crystal waveguides and nanocavities. *Opt. Lett.*, 29(22):2659–2661, 11 2004.

[61] M. Arcari, I. Söllner, A. Javadi, S. Lindskov Hansen, S. Mahmoodian, J. Liu, H. Thyrrestrup, E. H. Lee, J. D. Song, S. Stobbe, and P. Lodahl. Near-Unity Coupling Efficiency of a Quantum Emitter to a Photonic Crystal Waveguide. *Physical Review Letters*, 113(9):1–5, 2014.

[62] Freja T. Pedersen, Ying Wang, Cecilie T. Olesen, Sven Scholz, Andreas D. Wieck, Arne Ludwig, Matthias C. Löbl, Richard J. Warburton, Leonardo Midolo, Ravitej Uppu, and Peter Lodahl. Near Transform-Limited Quantum Dot Linewidths in a Broadband Photonic Crystal Waveguide. *ACS Photonics*, 7(9):2343–2349, 2020.

[63] ZEON Corporation. *ZEP520 High Resolution Positive Electron Beam Resist*, volume 1.02. 2001.

[64] Cen Shawn Wu, Yoshiyuki Makiuchi, and ChiiDong Chen. *High-energy Electron Beam Lithography for Nanoscale Fabrication.* In Tech, 2010.

[65] Tommaso Pregnolato. *Deterministic quantum photonic devices based on self-assembled quantum dots.* PhD thesis, 2019.

[66] L. E. Ocola and A. Stein. Effect of cold development on improvement in electron-beam nanopatterning resolution and line roughness. *Journal of Vacuum Science Technology B: Microelectronics and Nanometer Structures*, 24(6):3061–3065, 2006.

[67] L. Midolo, T. Pregnolato, G. Kiršanske, and S. Stobbe. Soft-mask fabrication of gallium arsenide nanomembranes for integrated quantum photonics. *Nanotechnology*, 26(48):1–6, 2015.

[68] A. Laucht, F. Hofbauer, N. Hauke, J. Angele, S. Stobbe, M. Kaniber, G. Böhm, P. Lodahl, M. C. Amann, and J. J. Finley. (023034):1–12.

[69] Ravitej Uppu, Hans T. Eriksen, Henri Thyrrestrup, Aslı D. Uğurlu, Ying Wang, Sven Scholz, Andreas D. Wieck, Arne Ludwig, Matthias C. Löbl, Richard J. Warburton, Peter Lodahl, and Leonardo Midolo. *Nature Communications*, (3782): 1–6.

[70] Xiaoyan Zhou, Irina Kulkova, Toke Lund-Hansen, Sofie Lindskov Hansen, Peter Lodahl, and Leonardo Midolo. High-efficiency shallow-etched grating on GaAs membranes for quantum photonic applications. *Applied Physics Letters*, 113(25): 1–5, 2018.

[71] K. Kuruma, Y. Ota, M. Kakuda, S. Iwamoto, and Y. Arakawa. Surface-passivated high-Q GaAs photonic crystal nanocavity with quantum dots. *2001.02377*, pages 4–6, 2019.

[72] Pascale Senellart, Glenn Solomon, and Andrew White. High-performance semiconductor quantum-dot single-photon sources. *Nature Nanotechnology*, 12(11): 1026–1039, 2017.

[73] Gilles Brassard, Norbert Lütkenhaus, Tal Mor, and Barry C. Sanders. Limitations on practical quantum cryptography. *Physical Review Letters*, 85(6):1330–1333, 2000.

[74] T. C. Ralph. Boson sampling on a chip. *Nature Photonics*, 7(7):514–515, 2013.

[75] L. L. Rosenberg, G. LaRoche, and J. M. Ehlert. Evidence for heterogeneous turnover of iodine in rat thyroid glands. *Endocrinology*, 79(5):927–934, 1966.

[76] R. Hambury Brown and R. Q. Twiss. Correlation between photons in two coherent beams of light. *Journal of Astrophysics and Astronomy*, 15(1):13–19, 1994.

[77] Christopher Gerry and Peter Knight. *Introductory Quantum Optics*. Cambridge University Press, 10 2004.

[78] C. K. Hong, Z. Y. Ou, and L. Mandel. Measurement of Subpicosecond Time Intervals between Two Photons by Interference. *Physical Review Letters*, 59(18): 2044–2046, 1987.

[79] K. H. Madsen, S. Ates, J. Liu, A. Javadi, S. M. Albrecht, I. Yeo, S. Stobbe, and P. Lodahl. Efficient out-coupling of high-purity single photons from a coherent quantum dot in a photonic-crystal cavity. *Physical Review B*, 90(15):1–11, 2014.

[80] Charles Santori, David Fattal, Jelena Vučković, Glenn S. Solomon, and Yoshihisa Yamamoto. Indistinguishable photons from a single-photon device. *Conference on Quantum Electronics and Laser Science (QELS) - Technical Digest Series*, 89(10): 8–11, 2003.

[81] Jeppe Johansen, Brian Julsgaard, Søren Stobbe, Jørn M. Hvam, and Peter Lodahl. Probing long-lived dark excitons in self-assembled quantum dots. *Physical Review B*, 81(8):1–4, 2010.

[82] Pierre Türschmann, Hanna Le Jeannic, Signe F. Simonsen, Harald R. Haakh, Stephan Götzinger, Vahid Sandoghdar, Peter Lodahl, and Nir Rotenberg. Coherent nonlinear optics of quantum emitters in nanophotonic waveguides. *Nanophotonics*, 8(10):1641–1657, 2019.

[83] C Arnold, V Loo, A Lemaître, I Sagnes, O Krebs, P Voisin, P Senellart, and L Lanco. Cavity-Enhanced Real-Time Monitoring of Single-Charge Jumps at the Microsecond Time Scale. *PHYSICAL REVIEW X*, 021004(4):1–6, 2014.

[84] Mete Atatüre, Jan Dreiser, Antonio Badolato, Alexander Högele, Khaled Karrai, and Atac Imamoglu. Quantum-Dot Spin-State Preparation with Near-Unity Fidelity. *Science*, 312(5773):551–554, 2006.

[85] Stefan Seidl, Martin Kroner, Khaled Karrai, and Richard J Warburton. Voltage-Controlled Optics of a Quantum Dot. *Physical Review Letters*, 93(11):19–22, 2004.

[86] J. Houel, A. V. Kuhlmann, L. Greuter, F. Xue, M. Poggio, R. J. Warburton, B. D. Gerardot, P. A. Dalgarno, A. Badolato, P. M. Petroff, A. Ludwig, D. Reuter, and A. D. Wieck. Probing single-charge fluctuations at a GaAs/AlAs interface using laser spectroscopy on a nearby InGaAs quantum dot. *Physical Review Letters*, 108 (10):1–5, 2012.

[87] D Haft, F Bickel, A Lorke, R J Warburton, C Scha, K Karrai, J M Garcia, W Schoenfeld, and P M Petroff. Optical emission from a charge-tunable quantum ring. *Nature*, 405(6):8–11, 2000.

[88] A. Abragam. *The principles of Nuclear Magnetism.* Oxford University Press, London, 1961.

[89] Alexander V. Khaetskii, Daniel Loss, and Leonid Glazman. Electron spin decoherence in quantum dots due to interaction with nuclei. *Physical Review Letters*, 88(18):1868021–1868024, 2002.

[90] I. A. Merkulov, Al L. Efros, and M. Rosen. Electron spin relaxation by nuclei in semiconductor quantum dots. *Physical Review B*, 65(20):2053091–2053098, 2002.

[91] A. Greilich, D. R. Yakovlev, A. Shabaev, Al L. Efros, I. A. Yugova, R. Oulton, V. Stavarache, D. Reuter, A. Wieck, and M. Bayer. Mode locking of electron spin coherences in singly charged quantum dots. *Science*, 313(5785):341–345, 2006.

[92] Bernhard Urbaszek, Xavier Marie, Thierry Amand, Olivier Krebs, Paul Voisin, Patrick Maletinsky, Alexander Högele, and Atac Imamoglu. Nuclear spin physics in quantum dots: An optical investigation. *Reviews of Modern Physics*, 85(1): 79–133, 2013.

[93] E. A. Chekhovich, M. N. Makhonin, A. I. Tartakovskii, A. Yacoby, H. Bluhm, K. C. Nowack, and L. M.K. Vandersypen. Nuclear spin effects in semiconductor quantum dots. *Nature Materials*, 12(6):494–504, 2013.

[94] Andreas V. Kuhlmann, Jonathan H. Prechtel, Julien Houel, Arne Ludwig, Dirk Reuter, Andreas D. Wieck, and Richard J. Warburton. Transform-limited single photons from a single quantum dot. *Nature Communications*, 6:4–9, 2015.

[95] Daniel Najer, Immo Söllner, Pavel Sekatski, Vincent Dolique, Matthias C. Löbl, Daniel Riedel, Rüdiger Schott, Sebastian Starosielec, Sascha R. Valentin, Andreas D. Wieck, Nicolas Sangouard, Arne Ludwig, and Richard J. Warburton. A gated quantum dot strongly coupled to an optical microcavity. *Nature*, 575(7784): 622–627, 2019.

[96] L. Besombes and K. Kheng Kheng. Acoustic phonon broadening mechanism in single quantum dot emission. *PHYSICAL REVIEW B*, 63(155307):1–5, 2001.

[97] A J Ramsay, Achanta Venu Gopal, E M Gauger, A Nazir, B W Lovett, A M Fox, and M S Skolnick. Damping of Exciton Rabi Rotations by Acoustic Phonons in Optically Excited InGaAs/GaAs Quantum Dots. *PHYSICAL REVIEW LETTERS*, 017402(1):20–23, 2010.

[98] Emil V. Denning, Jake Iles-Smith, Niels Gregersen, and Jesper Mork. Phonon effects in quantum dot single-photon sources. *Optical Materials Express*, 10(1): 222–239, 2020.

[99] Antoine Reigue, Jake Iles-smith, Fabian Lux, Léonard Monniello, Mathieu Bernard, Florent Margaillan, Aristide Lemaitre, Anthony Martinez, Dara P S Mccutcheon, Jesper Mørk, Richard Hostein, and Valia Voliotis. Probing Electron-Phonon Interaction through Two-Photon Interference in Resonantly Driven Semiconductor Quantum Dots. *PHYSICAL REVIEW LETTERS*, 233602(6):1–6, 2017.

[100] P. Kaer, N. Gregersen, and J. Mork. *New Journal of Physics*.

[101] P Tighineanu, C L Dreeßen, C Flindt, P Lodahl, and A S Sørensen. Phonon Decoherence of Quantum Dots in Photonic Structures : Broadening of the Zero-Phonon Line and the Role of Dimensionality. *Physical Review Letters*, 120(25): 257401–1–257401–7, 2018.

[102] Alexia Auffèves-Garnier, Christoph Simon, Jean Michel Gérard, and Jean Philippe Poizat. Giant optical nonlinearity induced by a single two-level system interacting with a cavity in the Purcell regime. *Physical Review A - Atomic, Molecular, and Optical Physics*, 75(5):1–16, 2007.

[103] A. Javadi, I. Söllner, M. Arcari, S. Lindskov Hansen, L. Midolo, S. Mahmoodian, G. Kiršansk, T. Pregnolato, E. H. Lee, J. D. Song, S. Stobbe, and P. Lodahl. Single-photon non-linear optics with a quantum dot in a waveguide. *Nature Communications*, 6(8655):1–5, 2015.

[104] Romeo Bernini and Luigi Zeni. *Optoelectronics*. 2010.

[105] Ying Wang, Ravitej Uppu, Xiaoyan Zhou, Camille Papon, Sven Scholz, Andreas D. Wieck, Arne Ludwig, Peter Lodahl, and Leonardo Midolo. *Applied Physics Letters*, (13):131106–1–131106–7.

[106] Emmanuel Rosencher and Borge Vinter. *Complement to Chapter 7*. 2010.

[107] Benjamin Pen-Cheng Tsou. *Equivalent-circuit modeling of quantum-well lasers and fibre-optic communications channels*. PhD thesis, 2000.

[108] Davide Colleoni, Giacomo Miceli, and Alfredo Pasquarello. Fermi-level pinning through defects at GaAs/oxide interfaces: A density functional study. *Physical Review B*, 92(12):1–12, 2015.

[109] S. D. Offsey, J. M. Woodall, A. C. Warren, P. D. Kirchner, T. I. Chappell, and G. D. Pettit. Unpinned (100) GaAs surfaces in air using photochemistry. *Applied Physics Letters*, 48(7):475–477, 1986.

[110] W. E. Spicer, P. W. Chye, P. R. Skeath, C. Y. Su, and I. Lindau. New and Unified Model for Schottky Barrier and Iii-V Insulator Interface States Formation. *Journal of vacuum science and technology*, 16(5):1422–1433, 1979.

[111] T. D. Visser, H. Blok, B. Demeulenaere, and D. Lenstra. Confinement factors and gain in optical amplifiers. *IEEE Journal of Quantum Electronics*, 33(10):1763–1766, 1997.

[112] G. E. Stillman, C. M. Wolfe, C. O. Bozler, and J. A. Rossi. Electroabsorption in GaAs and its application to waveguide detectors and modulators. *Applied Physics Letters*, 28(9):544–546, 1976.

[113] Camille Papon, Xiaoyan Zhou, Henri Thyrrestrup, Zhe Liu, S Øren Stobbe, R Üdiger Schott, Andreas D. Wieck, Arne Ludwig, Peter Lodahl, and Leonardo Midolo. Nanomechanical single-photon routing. 6(4):524–530, 2019.

[114] H. C. Casey, D. D. Sell, and K. W. Wecht. Concentration dependence of the absorption coefficient for n- and p-type GaAs between 1.3 and 1.6 eV. *Journal of Applied Physics*, 46(1):250–257, 1975.

[115] F. P. Payne and J. P.R. Lacey. A theoretical analysis of scattering loss from planar optical waveguides. *Optical and Quantum Electronics*, 26(10):977–986, 1994.

[116] Biswarup Guha, Felix Marsault, Fabian Cadiz, Laurence Morgenroth, Vladimir Ulin, Vladimir Berkovitz, Aristide Lemaître, Carmen Gomez, Alberto Amo, Sylvain Combrié, Bruno Gérard, Giuseppe Leo, and Ivan Favero. Surface-enhanced gallium arsenide photonic resonator with quality factor of 6×10^6. *Optica*, 4(2): 218–221, 2017.

[117] Iván Prieto González, Luis Enrique Muñoz Camuñez, Alfonso González Taboada, Carmen Robles Urdiales, Jose María Ripalda Cobián, and Pablo Aitor Postigo Resa. Fabrication of high quality factor GaAs/InAsSb photonic crystal microcavities by inductively coupled plasma etching and fast wet etching. *Journal of Vacuum Science and Technology B*, 32(1):011204–2–011204–5, 2014.

[118] Rodrigo Benevides, Michaël Ménard, Gustavo S. Wiederhecker, and Thiago P. Mayer Alegre. Ar/Cl2 etching of GaAs optomechanical microdisks fabricated with positive electroresist. *Optical Materials Express*, 10(1):57–67, 2019.